CRANFIELD UNIVERSITY

PHD THESIS

INVESTIGATION TOWARDS A COUPLING BETWEEN POPULATION BALANCE AND SOLIDIFICATION MODELS

ARNAUD BOURDILLON

SUPERVISOR: DR. P.VERDIN

Cranfield University, School of Water, Energy and Environment
Oil & Gas Engineering Centre
August 2016

This thesis is submitted in partial fulfilment of the requirements for the Degree of PhD

It's the job that's never started as takes longest to finish.
All we have to decide is what to do with the time that is given us...

John Ronald Reuel Tolkien

Abstract

Due to the current oil consumption increase, deposits have decreased drastically. Engineers are constantly pushing the limits in order to drill deeper, convey oil further or build more efficient and sturdy pipelines. In an effort to obtain this rare ressource, companies are sometimes forced to install pipelines in extreme conditions and isolated terrains to exploit untouched oil deposits. If the structural designs of these devices have come to an agreement, internal phenomena occuring during the oil transport, are, currently not fully understood. In particular, droplets distribution evolution along with freezing events are the two main mechanisms responsible for efficiency loss of pipelines under extreme conditions. The aim of this work is to improve the current knowledge on these phenomena.

For many years, oil industry has focused on expensive experiments to better apprehend complex flow phenomena. A promising alternative, computational fluid dynamic (CFD), has been used in this PhD to fill the gap of knowledge in this field of study. Two new single-fluid solidification solvers, an improved population balance model and a novel multi-fluid solidification model have been developed. These solvers have been implemented in an open-source CFD environment (OpenFOAM) to ensure universal acces and a potential extension to this work.

It is shown that both single-fluid solidification solvers provide very good results when compared to experimental data. The maximum local discrepancies are evaluated below 20% for the worst case. The population balance model study performed in this PhD has identified important parameters, often under-looked. These findings have led to an improvement of the previous model close to 30% for the best case when compared to experimental results. The multi-fluid solidification model provides accurate ice formation rates (10% of maximal local discrepancies) when compared to experiments.

The work presented in this thesis, describes, within the same CFD environment, solvers able to compute both droplet size and distribution evolution and solidification processes. They can be used separately or conjointly to perform the numerical analysis of the flow behavior under extreme conditions, improving the way such problems are currently tackled. They can also be enhanced further to deal with sligthtly different research areas such as hydrates formations and corrosion events.

Acknowledgments

My first and biggest thanks goes to my supervisor Dr. Patrick Verdin for his invaluable help throughout this work. He went above his duties as supervisor both within and beyond the scope of this PhD. I could never thank him enough for the amount of time he has dedicated to me and his precious advices.

I would like to thank all the members of the multiphase flow group of Cranfield university who have closely follow and assess my progress. A special thank to Dr. Robert Sawko for his great help in coding and from which I always received the most challenging questions.

A special thank to my fellow PhD students with which I shared joy, doubts and from times to times laughs beyond control. Some would say a PhD is a lonely road. To those I would respond that it is always better to ride with friends.

I would like to thank Cranfield University and Prof. Chris Thompson to have given me the opportunity to pursue my work.

I strongly believe that undergoing a PhD without the support of a family is close to impossible. Mine has been extraordinary. Supporting my changing moods, helping me realizing that everything is relative and offering invaluable support. I don't think I will ever be able to thank them enough but every member of this singular company has contributed, one way or another, to the completion of this PhD.

To Marion Bournot, the girl who made everything enjoyable and for two of the best man I have ever known, Mr Daniel Gaudin and Mr Robert Tessier who are deeply missed...

Table of Contents

Abstract 3

Acknowledgments 4

List of Figures 9

List of Tables 11

List of Equations 12

List of abbreviations 16

List of Publications 17

I Introduction and scope of the study 18

II Population balance modelling 22

1 Review of population balance modelling 23

2 Introduction to population balance modelling 24
- 2.1 Population balance methods . . . 25
  - 2.1.1 Methods of classes . . . 25
  - 2.1.2 Methods of moments . . . 26
  - 2.1.3 Quadrature methods of moment . . . 26
- 2.2 Break-up models . . . 27
- 2.3 Coalescence models . . . 27

3 Eulerian-Eulerian model for multiphase flows 29
- 3.1 Mass and momentum conservation equations . . . 30
- 3.2 Turbulence equations . . . 30
- 3.3 Interphase source terms modelling . . . 32
  - 3.3.1 Drag force . . . 32
    - 3.3.1.1 Schiller and Naumann model . . . 34
    - 3.3.1.2 Hamard and Rybczynski model . . . 34
    - 3.3.1.3 Zhang and VanderHeyden model . . . 35
    - 3.3.1.4 Morsi and Alexander model . . . 35

3.3.1.5 Barnea and Mizrahi model . . . 35
3.3.1.6 Ishii and Zuber model . . . 36
3.3.1.7 Kumar and Hartland model . . . 36
3.3.1.8 Snyder et al. model . . . 37
3.3.1.9 Results and discussion . . . 37
3.3.2 Lift force . . . 37
3.3.3 Turbulent dispersion force . . . 39
3.3.4 Virtual mass force . . . 39

4 Population balance model for particle size prediction 42
4.1 Standard method of moment derivation . . . 43
4.2 $S-\gamma$ model . . . 45
4.3 Break-up modelling . . . 47
4.3.1 Break-up model . . . 47
4.3.1.1 Break-up regimes . . . 47
4.3.1.2 Viscous break-up . . . 48
4.3.1.3 Inertia break-up . . . 49
4.4 Coalescence modelling . . . 49
4.4.1 Coalescence model . . . 49
4.4.1.1 Viscous collision . . . 49
4.4.1.2 Inertial collision . . . 50

5 Parameters influencing droplet size prediction 52
5.1 Numerical campaign . . . 54
5.2 Grid independence study . . . 54
5.3 Interphase forces effect . . . 55
5.4 Turbulence model effects . . . 56
5.4.1 Realizable 2-layer k-ε model . . . 56
5.4.2 Turbulence response model . . . 58
5.4.3 Results and discussions . . . 58
5.5 Analysis of different drag models . . . 59
5.5.1 Results and discussion . . . 60
5.6 Break-up model effect . . . 60
5.6.1 Droplets generation during break-up . . . 61
5.6.2 Influence of the critical diameter value . . . 61
5.7 Coalescence model effect . . . 63
5.8 Parametric study summary . . . 63

6 Droplet size evolution in horizontal pipeline 66
6.1 Model verification and validation . . . 67
6.2 Additional numerical investigations . . . 68

7 Conclusions and discussions 71

Nomenclature 73

III Solidification phenomenon modelling 76

8 Review of solidification phenomenon modelling 77

9 Introduction to solidification processes and modelling 78
9.1 Solidification process . . . 79
9.2 Mathematical models for solidification . . . 81
9.3 Treatment of the partially solidified region . . . 84

10 Natural convection process 87
10.1 Natural convection model . . . 88
10.1.1 Temperature-dependent parameters . . . 88
10.1.2 Momentum and energy conservation equations . . . 88
10.2 Numerical simulations of natural convection in cavities . . . 90
10.2.1 Numerical campaign . . . 90
10.2.2 Grid independence study . . . 90
10.2.3 Model verification and simulations results . . . 93
10.2.4 Comparison with the standard Boussinesq approximation . . . 95
10.2.5 Comparison with Experimental measurements . . . 96

11 Solidification process with mushy region modelling 98
11.1 Solidification model with mushy region (IF) . . . 99
11.1.1 Energy conservation equation . . . 99
11.1.2 Temperature dependent fluid properties . . . 101
11.1.3 Mass and momentum conservation equations . . . 101
11.2 Numerical simulations of water freezing in cavities . . . 102
11.2.1 Numerical campaign . . . 102
11.2.2 Grid independence study . . . 102
11.2.3 Model verification and simulations results . . . 106
11.2.4 Comparison with Experimental measurements . . . 109
11.3 Numerical simulations of water freezing in cylinders . . . 110
11.3.1 Numerical campaign . . . 110
11.3.2 Grid independence study . . . 110
11.3.3 Model verification and simulations results . . . 112

12 Solidification process with slurry-mushy regions modelling 116
12.1 Solidification model with slurry-Mushy regions (IFSM) . . . 117
12.1.1 Energy conservation equation . . . 118
12.1.2 Mass and momentum conservation equations . . . 118
12.2 Numerical simulations of water freezing in cavities . . . 121
12.2.1 Model verification and comparisons with IcingFoam . . . 121
12.3 Numerical simulations of water freezing in cylinders . . . 124
12.3.1 Model verification and comparison with IcingFoam . . . 124

13 Conclusions and discussions 128

Nomenclature 131

IV Towards a possible coupling between population balance and solidification models **133**

14 Summary 134

15 Introduction 135

16 Solidification process for multiphase flows 136
16.1 Multiphase solidification solver . . . 137
16.1.1 Temperature dependent fluid properties . . . 137
16.1.2 Energy equations for continuous and dispersed phases . . . 140
16.1.3 Momentum equations for continuous and dispersed phases . . . 141
16.2 Natural convection process modelling . . . 142
16.3 Solidification process modelling . . . 143

17 Population balance modelling for multiphase flow 148
17.1 Continuity, momentum and energy equations . . . 149
17.2 Break-up modelling . . . 150
17.3 Coalescence modelling . . . 151
17.4 Interfacial forces . . . 152
17.4.1 Drag force . . . 153
17.4.1.1 Schiller and Naumann model . . . 153
17.4.1.2 Snyder et al. model . . . 154
17.4.2 Lift force . . . 154
17.4.3 Turbulent dispersion force . . . 154
17.5 Preliminary results . . . 154

18 Conclusions and discussions 157

Nomenclature 158

V Final conclusions and future work **162**

19 Final conclusions and discussions 163

20 Future work 166

References 166

List of Figures

3.1 Drag force acting on a spherical droplet in horizontal motion due to an incoming flow. . . . 33
3.2 Drag coefficient as a function of the Particle Reynolds number 38
3.3 Lift force towards the top acting on a spherical droplet. . . . 39
3.4 Turbulence dispersion force acting on high concentration region of droplet. . . . 40
3.5 Virtual mass during the motion of a spherical droplet. . . . 41

5.1 Influence of drag (F^D), turbulent dispersion (F^{td}), lift (F^ℓ) and virtual mass (F^{vm}) forces on the prediction of the droplet diameter in a plane section of the pipe. Experimental work shows particle diameters in the range $0 < d_{exp} < 1000$ μm 56
5.2 Turbulence model study 59
5.3 Numerical drop size prediction for different drag models. Experimental work shows particle diameters in the range $0 < d_{exp} < 1000$ μm . . 60
5.4 Sauter mean diameter estimates depending on the number of child droplet produced during break-up events. Experimental work shows particle diameters in the range $0 < d_{exp} < 1000$ μm 61
5.5 Sauter mean diameter estimation depending on the value of the critical Weber number. Experimental work shows a range of particle diameter such as $0 < d_{exp} < 1000$ 62
5.6 Sauter mean diameter of droplets at the pipe outlet estimation, in function of the drainage time models. . . . 63

6.1 Numerical results. . . . 67
6.2 Additional numerical results. . . . 69

9.1 Phase change nomenclature (left) and phase diagram (right). . . . 79

10.1 Water density variation function of the temperature between -20 $^\circ C$ and 20 $^\circ C$ 89
10.2 Profiles obtained from the mesh sensitivity analysis (ConvectionFoam) 92
10.3 Numerical results obtained with ConvectionFoam 94

11.1 Deviation between linear and error function for α_ℓ between $T_{sol} =$ 272.75K and $T_{liq} = 273.75$ K 100
11.2 Temperature profiles obtained from the mesh sensitivity analysis . . . 103
11.3 U velocity profiles obtained from the mesh sensitivity analysis 104
11.4 V velocity profile obtained from the mesh sensitivity analysis 105

11.5 Ice layer shape comparison . . . 106
11.6 Numerical results obtained with IcingFoam . . . 107
11.7 Comparisons between experimental work and IcingFoam solution for water freezing inside cavities at $t = 2600\ s$ . . . 109
11.8 Mesh sensitivity analysis for a water freezing process in a cylindrical enclosure after 42 minutes of physical time, along x-axis in the y-middle plane . . . 111
11.9 Numerical temperature profiles at different locations in the cylindrical enclosure with IcingFoam and comparison with experimental data - Wall temperature= -18^oC . . . 112
11.10 Temperature evolution, through time, at different locations inside the cylindrical enclosure . . . 114

12.1 liquid, slurry, mushy, solid regions transitions . . . 117
12.2 Slurry and mushy switching functions plot . . . 119
12.3 IcingFoamSlurryMushy numerical results - Temperature and velocity fields along horizontal and vertical line . . . 122
12.4 Slurry and Mushy switching functions behaviour during water solidification in cavity at $t = 100\ s$ . . . 123
12.5 Numerical temperature profiles at the top, center, side and bottom parts of the cylindrical enclosure with IcingFoamSlurryMushy and comparison with experimental data - Wall temperature= -18^oC . . . 125
12.6 Numerical temperature profiles at the center of the cylindrical enclosure with IcingFoamSlurryMushy for different wall temperatures and comparison with experiments . . . 127

16.1 Variable water properties values between $0°C$ and $20°C$ . . . 138
16.2 Numerical results obtained with IcingMultiPhase for convection problem . . . 143
16.3 Numerical results obtained with MultiIcingFOAM for solidification problem . . . 144
16.4 Comparisons between MultiIcingFOAM and experimental ice-layer . . . 144
16.5 Solidification rate process with IcingFoam and MultiIcingFOAM . . . 145
16.6 Numerical results obtained with IcingFoam and MultiIcingFOAM . . . 146

17.1 Break-up and coalescence rate obtained with PBMFoam solver . . . 156

List of Tables

3.1 Range of values for Richardson and Zaki exponent (b) 34

4.1 Break-up regimes and bounds of the integration 48
4.2 Drainage time models 50

5.1 Material properties of the two phases 54
5.2 Characteristics of the six grid system for mesh independence study . 55
5.3 List of model tested in the parametric study. 64

6.1 Material properties of kerosene for Cases 1-3 70
6.2 Material properties of aqueous potassium for Case 1-3 70

9.1 Mathematical expression of solidification terms. 80
9.2 Slurry-viscosity models. 85

10.1 Water properties for the natural convection study 90
10.2 Structured meshes for cavity cases 91
10.3 Numerical results of ConvectionFoam between $t = 100\ s$ and $t = 1500\ s$ 95
10.4 Comparisons against standard Boussinesq approximation at $t = 1500\ s$ 96
10.5 Comparisons against experiments at $t = 1500\ s$ 97

11.1 Water properties for the solidification study 103
11.2 Solidification rate process with IcingFoam between $t = 100\ s$ and $t = 1500\ s$ 108
11.3 Water properties for the freezing process in the cylindrical enclosure . 110
11.4 Structured meshes for cylindrical enclosure cases (M1, M2 and M3) . 111
11.5 Structured meshes for cylindrical enclosure cases (M4 and M5) 111
11.6 Solidification rate process with IcingFoam for cylinders between $t = 300\ s$ and $t = 1000\ s$ 114

12.1 Governing equations of the IcingFoamSlurryMushy solver. 120
12.2 Water properties for the solidification study in IcingFoamSlurryMushy 121
12.3 Comparisons between IF and IFSM for cavity at $t = 100\ s$ 123
12.4 Comparisons between IF and IFSM for cavity at $t = 1500\ s$ 124
12.5 Comparisons between velocity and ice layer profiles obtained with IF and IFSM 126
12.6 Comparisons between temperature profiles obtained with IF and IFSM 126

16.1 Coefficients for the variable properties functions. 138

17.1 Material properties of the two phases 155

List of Equations

2.1 PBE general form . . . 25
3.1 Continuity equation for Eulerian PBM model . . . 30
3.2 Mass balance equations . . . 30
3.3 Momentum equations for Eulerian PBM model . . . 30
3.4 Forces relationship for boundedness of momentum equations . . . 30
3.5 Turbulent kinetic energy (k) equations for Eulerian PBM model . . . 31
3.6 Additional terms in turbulent kinetic energy expression . . . 31
3.7 Turbulent dissipation (ε) equations for Eulerian PBM model . . . 31
3.8 Additional terms in turbulent dissipation expression . . . 32
3.9 Turbulent dynamic viscosity expression . . . 32
3.10 C_μ expression in Realizable $k-\varepsilon$ model . . . 32
3.11 Additional parameters for C_μ expression . . . 32
3.12 Drag force general expression . . . 33
3.13 Drag coefficient correction equation . . . 33
3.14 Drag coefficient Zaki correction model . . . 33
3.15 Particle Reynolds number definition . . . 34
3.16 Drag coefficient (Schiller & Naumann) . . . 34
3.17 Drag coefficient (Hamard) . . . 34
3.18 Correlation coefficient (Hamard) . . . 34
3.19 Drag coefficient (Zhang & VanderHeyden) . . . 35
3.20 Drag coefficient (Morsi & Alexander) . . . 35
3.21 Constants in drag coefficient (Morsi & Alexander) . . . 35
3.22 Mixture Reynolds number (Barnea & Mizrahi) . . . 36
3.23 Mixture viscosity(Barnea & Mizrahi) . . . 36
3.24 Empirical coefficients (Barnea & Mizrahi) . . . 36
3.25 Drag coefficient (Barnea & Mizrahi) . . . 36
3.26 Mixture viscosity (Ishii & Zuber) . . . 36
3.27 Exponent a (Ishii & Zuber) . . . 36
3.28 Drag coefficient (Ishii & Zuber) . . . 36
3.29 Drag coefficient (Kumar & Hartland) . . . 36

3.30 Drag coefficient (Snyder et al.) . . . 37
3.31 Lift force general expression . . . 38
3.32 Lift force expression (Auton & Hunt) . . . 38
3.33 Turbulent dispersion force general expression . . . 39
3.34 Virtual mass force general expression . . . 40
3.35 Fraction of free stream of fluid . . . 40
3.36 Upper bound of the virtual mass force coefficient . . . 40
3.37 Virtual mass coefficient (Zuber) . . . 41
3.38 Virtual mass coefficient for multiphase flows (Zuber) . . . 41
3.39 Virtual mass coefficient for multiphase flows with α_c (Zuber) . . . 41
4.1 Total number density expression ($N(\mathbf{x}, t)$) . . . 43
4.2 $N(\mathbf{x}, t)$ for a population characterized by their length . . . 43
4.3 Specific PBE for ξ, $\mathbf{x}$, $\Omega_{\mathbf{x}}$ and Ω_{ξ} . . . 43
4.4 GPBE expression . . . 44
4.5 Specific GPBE expression for ξ . . . 44
4.6 Specific GPBE expression for ξ in terms of moments . . . 44
4.7 GPBE expression with source term S . . . 44
4.8 Moment of the particle size distribution (PSD) . . . 45
4.9 $d_{3,2}$ and $d_{3,0}$ expressions . . . 45
4.10 Transport equation for the 0th moment . . . 45
4.11 Break-up and coalescence terms expressions . . . 45
4.12 Transport equations for the moments ($S - \gamma$ model) . . . 45
4.13 Transport equations for the moments ($S - \gamma$ model) . . . 46
4.14 Three first moments expression ($S - \gamma$ model) . . . 46
4.15 Sauter mean diameter expression ($S - \gamma$ model) . . . 46
4.16 Three-zero diameter expression ($S - \gamma$ model) . . . 46
4.17 Log-normal distribution (Hill) . . . 46
4.18 Transport equations for each moments with source terms ($S - \gamma$ model) 46
4.19 Break-up formulation (Lo & Zhang model) . . . 47
4.20 Probability density function (Lo & Zhang model) . . . 47
4.21 Integration bounds for break-up regimes (Lo & Zhang model) . . . 47
4.22 Kolmogorov length scale . . . 47
4.23 Critical diameter in viscous break-up (Lo & Zhang model) . . . 48
4.24 Local Kolmogorov shear rate . . . 48
4.25 Capillary number . . . 48
4.26 Break-up timescale in viscous break-up . . . 48
4.27 Expression of the function $\log f\left(\frac{\mu_d}{\mu_c}\right)$ . . . 48
4.28 d_{crit} and $\tau(d)$ in inertia break-up . . . 49
4.29 Weber number expression . . . 49
4.30 Coalescence formulation (Lo & Zhang model) . . . 49
4.31 Viscous collision rate K_{coll}^{vi} (Lo & Zhang model) . . . 50
4.32 $P_{coll}^{vi}(d_{eq})$ expression (Lo & Zhang model) . . . 50
4.33 Collision force expression (Lo & Zhang model) . . . 50
4.34 Critical film thickness expression (Lo & Zhang model) . . . 50
4.35 Inertial collision rate K_{coll}^{in} (Lo & Zhang model) . . . 50
4.36 Probability of inertial collision $P_{coll}^{in}(d_{eq})$ (Lo & Zhang model) . . . 51

4.37 Maximum phase difference Φ_{max} (Lo & Zhang model) 51
9.1 First law of thermodynamic 80
9.2 Heat capacity at constant volume 80
9.3 General enthalpy expression 81
9.4 Heat capacity at constant pressure 81
9.5 Transition between liquid and solid states 84
10.1 Polynomial water density variation 88
10.2 Momentum equations for convection solver 88
10.3 Validity of Boussinesq approximation 89
10.4 Energy equations for convection solver 89
10.5 Thermal conductivity definition 89
10.6 Dimensionless value of temperature 91
10.7 Dimensionless values used for solidification processes 93
10.8 Density variation expression in the standard Boussinesq approximation . 95
10.9 Density variation expression in ConvectionFoam 95
11.1 Enthalpy equations for mushy solidification solver 99
11.2 Total enthalpy expression 99
11.3 Sensible enthalpy expression 99
11.4 Linear liquid volume fraction expression 99
11.5 Total enthalpy as a function of the liquid volume fraction 100
11.6 Energy equations for mushy solidification solver 100
11.7 Source term for phase change processes in mushy solidification solver . . 100
11.8 Error function for liquid volume fraction 100
11.9 Total density expression for mushy solidification solver 101
11.10 Fluid properties definition for mushy solidification solver 101
11.11 Darcy source terms for velocity sink in mushy solidification solver 101
11.12 Momentum equations for mushy solidification solver 102
11.13 Energy source term (nc4 mar code) 106
12.1 Energy equations for slurry solidification solver 118
12.2 Dynamic viscosity expression for slurry solidification solver 118
12.3 Dynamic viscosity expression following Metzner 118
12.4 Slurry switching function 118
12.5 Momentum equations for slurry solidification solver 119
12.6 Mushy switching function 119
12.7 Darcy source terms for velocity sink in slurry solidification solver 119
16.1 Fluid properties evolution with temperature 137
16.2 Total fluid properties values computation 139
16.3 Water volume fraction function 139
16.4 Example of water/ice volume fraction computation 139
16.5 Volume fraction relationships 139
16.6 Energy equation for the dispersed water phase 140
16.7 Energy equation for the continuous oil phase 140
16.8 Convection term derivation in 2D 140
16.9 Thermal diffusivity and turbulence effects 141
16.10 Thermal diffusivity for single-fluid solver 141
16.11 Variation of heat between dispersed and continuous phases 141

16.12 Nusselt number . . . 141
16.13 Heat transfer coefficient between phases . . . 141
16.14 Dispersed and continous phases momentum equations . . . 142
16.15 Turbulence contribution to the momentum equations . . . 142
16.16 Dimensionless ice-layer height . . . 143
17.1 Continuity equations in PBMFOAM . . . 149
17.2 Momentum equations in PBMFOAM . . . 149
17.3 Energy equations in PBMFOAM . . . 150
17.4 Transport equations in PBMFOAM for the moments ($S-\gamma$ model) . . . 150
17.5 Probability density function in PBMFOAM . . . 150
17.6 Moment calculation in PBMFOAM . . . 150
17.7 Second orde rmoment in PBMFOAM . . . 151
17.8 Viscous and inertia break-up in PBMFOAM . . . 151
17.9 Diameters computation in PBMFOAM . . . 151
17.10 Transport equations with source terms in PBMFOAM ($S-\gamma$ model) . . . 151
17.11 Coalescence formulation in PBMFOAM (Lo & Zhang model) . . . 152
17.13 Equivalent diameter in PBMFOAM . . . 152
17.14 Coalescence term simplification in PBMFOAM . . . 152
17.15 Final definition of the coalescence term in PBMFOAM . . . 152
17.16 Drag force general expression in PBMFOAM . . . 153
17.17 Drag coefficient correction equation in PBMFOAM . . . 153
17.18 Particle Reynolds number definition in PBMFOAM . . . 153
17.19 Drag coefficient (Schiller & Naumann) in PBMFOAM . . . 153
17.20 Drag coefficient (Snyder et al.) in PBMFOAM . . . 154
17.21 Lift force expression (Auton & Hunt) in PBMFOAM . . . 154
17.22 Turbulent dispersion force general expression in PBMFOAM . . . 154

List of abbreviations

BBPF	BuoyantBoussinesqPimpleFoam solver
CF	ConvectionFoam solver
CFD	Computational fluid dynamics
CFL	Courant, Friedrichs and Lewy condition
ERF	Error function
IF	IcingFoam model
IMP	IcingMultiPhase model
IFSM	IcingFoamSlurryMushy model
LHS	Left hand side
NDF	Number density function
PBM	Population balance modelling
PSD	Particle size distribution
RHS	Right hand side

List of publications

- Numerical simulations of water freezing processes in cavities and cylindrical enclosures. Bourdillon.A.C, Verdin.P.G, Thompson.C.P. Applied thermal engineering, volume 75, 839-855, 2015.
- Numerical simulations of drop size evolution in a horizontal pipeline. Bourdillon.A.C, Verdin.P.G, Thompson.C.P. International journal of multiphase flow, volume 78, 44-58, 2016.
- Modelling Macroscopic Solidification of Binary Mixtures in Cavity and Channel Flows. Yam.K.S, Bourdillon.A.C, Sawko.R, Thompson.C.P. Journal of Heat and Mass transfer (submitted).

Part I

Introduction and scope of the study

Over the past few years, oil industry has become more than an economic stake since it regulates now the development of both importer and exporter countries. According to Fortune (2009), in 2008, from the top 20 private companies, 12 were oil companies or car manufacturers and the oil business was estimated, in 2009, to yield more than 6 billion a day (BP, 2009). To maintain and increase these profits, oil transport device (pipelines) designs are constantly optimized. Usually, more than one phase is transported in pipelines (liquid, gaseous or solid). Each phase possesses unique properties (density, viscosity, velocity...) and it is therefore crucial to be able to compute exchanges between them, along with accurate temperature, velocity and pressure fields to predict physical flow patterns and thus, the amount of oil output that can be expected from a given device.

As the oil comsumption always increases, ressources decrease drastically. Thankfully, the technologies have improved and as a result, it is now possible to drill deeper and to exploit untouched oil deposits. Oil platforms installation and drilling processes are, however, very expensive and from there, the oil pumped has to travel hundreds of kilometers through pipelines to reach purification stations. During the travel process, the flow behaviour can creates all sorts of complex phenomena that can reduce the life time of the device or even the oil output expected (mixing, separation or deposition).

After the 1973 oil crisis, which caused a drastic increase of the oil price in the USA, a pipeline was built to connect the newly discovered oil deposit of Prudhoe bay to Valdez, in Alaska. This system is called the Trans-Alaska Pipeline system (TAPS), contains twelve pump stations and is, nowadays, one of the world's largest pipeline system. It conveys oil between the two city along thousands of kilometers every day.

This pipeline has been specifically built to resist the extreme conditions of this isolated terrain (cold temperature, abscence of maintenance structure, impossibility to heat the pipe and zig-zags across the landscape). However, the physical phenomena occuring inside the pipeline and, especially, during the transport of oil, are yet, not fully understood. In particular, droplet break-up and coalescence due to the non-linear nature of the flow and freezing events caused unwanted incidents and, from time to time, loss of considerable amount of oil. The TAPS system is not the only device that suffers from having being installed under extreme conditions and there is a clear lack of useful tools to be able to better aprehend this field of research.

For many years, oil industry has focused on expensive experiments to obtain fundamental data able to provide a clear idea of the flow behaviour under various conditions. Even if accurate engineering quantities can be analyzed and obtained through measurement, human resources needed as well as obvious limitations, such as the impossibility to carry on experiments within real size pipelines, have pushed engineers, researchers and companies to look for more profitable approaches. Currently, a promising alternative, Computational Fluid Dynamics (CFD), which permits to obtain important engineering parameters through mathematical models and numerical simulations, is used daily by the world leader oil companies.

The purpose of this thesis is to use a CFD approach to investigate complex phenomena observed during oil transportation in pipelines under extreme conditions.

This thesis will focus on two phases, a dispersed water phase (droplets) transported by a continuous phase (oil) for pipelines used in extreme conditions (cold weather, deep water...). The intrinsic nature of the study area renders investigation of freezing and droplet transport processes essential. From an industrial point of view, being able to compute accurate blocking lengths of pipelines, evaluate ice strength adhesion and identify solidification areas are of great interest as these phenomena are a direct cause of efficiency loss and broken pipelines.

Over the past few years, many researchers have investigated solidification problems in pipelines. Among interesting results, the temperature gradient inside the walls of the pipe and the inlet velocity of the fluid, in liquid state, have been found to directly influence the solidification rate (Conde et al. (1976); Conde et al. (2004); Jalali & Najafi (2010)). Therefore, an accurate prediction of the velocities and motions of the different phases is essential to successfully deal with these problems. Among several physical processes, the change of size of the dispersed phase can influence its velocity directly.

For the scope of this study, typically, break-up and coalescence events of water drops transported by a continuous oil phase induce different mean velocities and therefore, different ice formation rates. Currently, a common approach to investigate the change of size of the dispersed phase is the population balance modelling. Several models have emerged over the past few years and this approach is still, deeply investigated (McGraw (1997); Petitti et al. (2012); Yuan et al. (2012)). Even if a population balance method is essential for this study, other phenomena, known to influence the motion of each of the phases, also need a particular attention. The forces constituting the momentum transfer term at the interphase, in particular drag, lift, virtual mass and turbulent dispersion forces, have been found by several researchers to directly impact the motion of the particles and therefore the velocity of the dispersed phase (Drew & Lahey (1987); Gupta & Pagalthivarthi (2006); Wei & Pang (2011)).

This work may significantly improve the way solidification problems are currently tackled. One of the main objectives of this research is to design a numerical model able to account for changes in size of the transported dispersed phase (droplets) and to develop, in parallel, a solidification model. Such a model might be enhanced through future research to solve solidification problems in pipelines more accurately than with current numerical models. Few similar studies have been proposed over the past few years but significant further research is still needed. Among them, Lei et al. (2009) developed a model for solidification and collision-growth in slab continuous casting caster and Vakhrushev et al. (2013) developed a Lagrangian model, based on the DPM theory, for bubbles motion and coupled it with a solidification model in OpenFOAM. However, no model able to compute phase change processes from liquid to solid with the help of a PBM approach has, from the author's best knowledge, been designed yet in an Eulerian-Eulerian framework. Moreover, models accounting for particle distribution to simulate change of size of the liquid phase and solidification, are not yet available, in OpenFOAM. Using both models can lead to considerable improvement for heat and mass transfer problems.

To summarize, the main objective of this PhD is to develop two solvers, a solidification model and a population balance based model and to perform thorough

numerical analyses to better understand the complex phenomena involved in such simulations. One of the most challenging task is to implement them in the open source CFD environment OpenFOAM. Both solvers used conjointly will permit to handle new CFD problems. The solidification model, discussed in this thesis, is able to take into account both mushy and slurry regions in a new formulation and to model its effect on solidification rate. A population balance solver, taking into account both break-up and coalescence events, has been identified from the literature review and validated. The novelty of the work presented in this thesis lies in the ability to identify key parameters which are of great importance when dealing with the PBM and the solidification solvers.

Finally, the current work can be extended. The solidification model has been developed further to handle multi fluid solidification problems in an Eulerian-Eulerian formulation and the implementation of the PBM solver identified has been tested. One of the novelty of this work has been to provide, within the same CFD environment, two solvers that can be used conjointly to handle both size change of particle and solidification processes. Few similar studies have emerged over the past few years. However, none has focused on a Eulerian-Eulerian formulation within an open source environment. Many applications could arise from these findings, such as a pure coupling (PBM and solidification within one single solver), hydrates formation or even corrosion related problems.

Part II

Population balance modelling

1 Review of population balance modelling 23

2 Introduction to population balance modelling 24
- 2.1 Population balance methods . . . 25
- 2.2 Break-up models . . . 27
- 2.3 Coalescence models . . . 27

3 Eulerian-Eulerian model for multiphase flows 29
- 3.1 Mass and momentum conservation equations . . . 30
- 3.2 Turbulence equations . . . 30
- 3.3 Interphase source terms modelling . . . 32

4 Population balance model for particle size prediction 42
- 4.1 Standard method of moment derivation . . . 43
- 4.2 $S - \gamma$ model . . . 45
- 4.3 Break-up modelling . . . 47
- 4.4 Coalescence modelling . . . 49

5 Parameters influencing droplet size prediction 52
- 5.1 Numerical campaign . . . 54
- 5.2 Grid independence study . . . 54
- 5.3 Interphase forces effect . . . 55
- 5.4 Turbulence model effects . . . 56
- 5.5 Analysis of different drag models . . . 59
- 5.6 Break-up model effect . . . 60
- 5.7 Coalescence model effect . . . 63
- 5.8 Parametric study summary . . . 63

6 Droplet size evolution in horizontal pipeline 66
- 6.1 Model verification and validation . . . 67
- 6.2 Additional numerical investigations . . . 68

7 Conclusions and discussions 71

Nomenclature 73

Chapter 1

Review of population balance modelling

This part presents theoretical and numerical aspects of population balance modelling (PBM). Current methods used to solve the population balance equations (PBE), along with break-up and coalescence models are reviewed in Chapter 2. The list is non-exhaustive and references are provided if additional information is required. The literature review has been carried out throughout this Part and in Chapters 3 and 4 in particular. The literature review has permited to identify a population balance model (standard method of moment), a break-up and a coalescence model that appears to be promising. From these findings, the models chosen within the scope of this PhD are derived in Chapters 3 and 4. These models are then used to carry out a thorough study on population balance modelling and to identify important parameters to be considered for accurate numerical simulations in this specific field. Interphase force effects, turbulence model, drag models, break-up and coalescence effects are deeply investigated in Chapter 5. It is found that the numerical model chosen gives accurate results when compared to experimental data and its ease of implementation within an open source software such as OpenFOAM has been highlighted. It has been demonstrated that a correct combination of models and parameters improves (47% for the best case) simulated results when compared to experimental data. Interactions between the different components of the whole model are discussed and their corresponding effects on the droplet diameter predictions are explained in Chapter 5. Finally, the present model is validated successfully against experimental work on drop size evolution inside horizontal pipelines in Chapter 6. The novelty of this work has permited to identifiy that the addition of the lift force tends to push the droplet toward the walls of the computational domain where turbulence and shear stress are the strongest, therefore leading to an increased break-up rate. Based on the findings of this study, recommendations for further population balance-based modelling with a standard method of moments are provided. Findings of this part will finally be used and expanded in Part IV.

Chapter 2

Introduction to population balance modelling

A literature review is presented in this chapter. Basic theoretical concepts of population balance modelling are detailed. Only the basic notions required to understand the population balance equations closure problems are presented in this chapter. Additional materials will be given in Chapter 4 where the full derivation of the PBE, in a standard method of moment framework is given. The nomenclature related to this entire part (i.e. Part II) is presented along with a description of each term. Current CFD models for break-up and coalescence events are also, briefly reviewed. Model names are given and review articles are referenced but no derivation will be detailed here, for the sake of clarity. This literature review has permitted to emphasize the promising compromise offered by the standard method of moment to handle PBM problems when compared to alternative methods. Additionally, one break-up and one coalescence model have been extracted from the literature review which satisfy the requirement of this PhD; a accurate model, validated against experimental results, and relatively easy to implement in an open source CFD code (OpenFOAM).

Contents

2.1 Population balance methods **25**
2.1.1 Methods of classes 25
2.1.2 Methods of moments 26
2.1.3 Quadrature methods of moment 26
2.2 Break-up models **27**
2.3 Coalescence models **27**

2.1 Population balance methods

During the transport of oil and water through pipes, interactions between the two fluids occur continuously. Considering oil as the continuous phase and water as the dispersed phase, these strong interactions can give birth to droplets being transported with the continuous phase. Such droplets can potentially interact with each other and with the pipe wall, leading to a complex physical behaviour. The correct prediction of droplets movement, size and shape evolution is necessary to evaluate the deposition rate along with other critical parameters influencing the flow such as separation and pressure gradients.

The population balance method (PBM) solving the population balance equations (PBEs) currently stands as the reference method in this field of study (Ramkrishna, 2000). From it's first derived use back in 1859 with Maxwell's kinetic theory of gas, population balance modelling interest has grown exponentially. The original population balance equations (PBE) have been generalized to some extent and is now used in many fields of research. PBE equations characterize the evolution of a population of particles in a given region of the domain through time, by a set of meaningful physical properties (coordinates, temperature, size, velocity, volume...). The number density function (i.e. NDF, $n(\mathbf{x}, \xi, t)$) gives all the necessary parameters useful to defined a population of particle. In its most general form, the PBE can be written as follows :

$$\frac{\partial n}{\partial t} + \nabla \cdot [n\mathbf{u}] = S \tag{2.1}$$

In Equation 2.1, S represents the source term describing discrete events. As the scope of this PhD focuses on liquid-liquid flows, these discrete events can be summarized as size changes, which can be computed through break-up and coalescence models. Each of these events can also be divided between birth and death rate of child droplets. The PBE equations therefore contain unclosed integrals and require numerical models for closure.

For the sake of clarity, only the most promising techniques for closure will be reviewed here (i.e. the method of classes, the method of moments and the quadrature method of moments). In nearly two-hundred years of investigation, researchers have managed to solve the PBE using a wide range of methods and it will be too long to present each of them here. One can refer to Marchisio & Fox (2013) for a detailed description, from the old Monte-Carlo methods (Friesen & Dabros (2003), Marchisio et al. (2003), Zhao et al. (2010)) to the most recent direct quadrature method of moments (DQMOM) (McGraw, 1997) and the extended quadrature method of moment (EQMOM) (Marchisio & Fox, 2013).

2.1.1 Methods of classes

Methods of classes have come as alternative solutions to overcome the computational expense induced by Monte-Carlo approaches (Hounslow et al. (1988), Litster et al. (1995), Ramkrishna (1985)). Within each class, the PBEs are solved directly for the number density function. For instance, within a given range of droplet sizes, the

particle size distribution (PSD) is discretized into an equivalent number of classes where the PBEs are solved. The number of classes necessary to accurately represent a population of droplets can therefore become very large and thus increase drastically the computational time. This is considered as the major drawback of the method of classes. In addition, the use of such method can be difficult. A mother droplet that belongs to a specific class at a specific time may produce for instance two or more child droplets during a break-up event that will belong to other classes in the future.

2.1.2 Methods of moments

Significant work has been performed over the past few years to solve the PBEs at a relatively low computational cost. The most promising approach is the method of moments, first introduced by Hulburt & Katz (1964). This method consists in solving the PBEs by tracking the moments of the particle size distribution instead of the number density function. This method permits to obtain a set of equations, expressed in terms of moments, that characterize the population of particles. Therefore, only few moments are necessary to entirely describe the population whereas an equivalent, the method of classes, would be to solve for fifty or sixty classes and thus for each iterations, leading to an enormous computational time. The remaining problem of the method of moments is that the source terms accounting for break-up and coalescence events contain the NDF and are therefore expressed in unclosed integrals. An interesting approach to overcome this problem lies in the ability to make an assumption on the shape of the NDF which solve the PBE directly. This promising method is referred to as the standard method of moments.

2.1.3 Quadrature methods of moment

McGraw (1997) introduced a new technique that permits to solve the PBE without using any assumption on the NDF. The equations are solved using a quadrature approximation and weights and abscissas are used to interpolate the formula. The NDF, therefore disappears from the source term and weights and abscissas can be retrieved from the moments. This method is known as the quadrature method of moments. One major drawback of the technique lies in its high difficulty to be implemented (Marchisio & Fox, 2013). However, this major breakthrough has led to a growing interest and the appearance of few pioneers techniques; the direct quadrature method of moments (DQMOM) (McGraw, 1997) and the extended quadrature method of moment (EQMOM) (Marchisio & Fox, 2013). They are, however, still recent and additional efforts has to be made to ease their implementation.

As a conclusion, a standard method of moment has been chosen to carry out this PhD as its constitutes a compromise between numerical accuracy and computational time.

2.2 Break-up models

Standard models for break-up are based on a critical Weber number. In this case, any droplet having a diameter greater than a critical diameter value, is assumed to break into smaller child droplets. A droplet subject to the motion of the surrounding fluid is deformed due to the action of the interphase source terms. Prior to any break-up event, a laps of time is present during which droplets are subject to a change of shape. A timescale for break-up events $\tau(d)$ is therefore present in the equations. A review performed in Liao & Lucas (2009) showed four different mechanisms of particle break-up: turbulent fluctuation and collision, viscous shear forces, shearing-off process and interfacial instabilities. These authors also presented several theoretical models for break-up which are available in the literature. They consider the balance between forces due to shear stress and turbulence (disruptive forces) and forces due to surface tension effects (restoring forces). Among interesting studies of break-up phenomenon, Kolev (1993) provides review of break-up causes. Several break-up models have emerged over the past few years. Among all these models, two are often used as references for many numerical studies. The Prince & Blanch (1990) model and the Luo & Svendsen (2004) break-up model which have been validated against experimental data of Hesketh et al. (1991). These models will not be derived here and one can see details in Liao & Lucas (2009). One of the drawback of both models is the high difficulty to implement them in an open source software like OpenFOAM as they contain unknown integral forms. However, a promising model for break-up has been successfully validated against experimental results of Simmons & Azzopardi (2001). In this model, developed by Lo & Rao (2007), both inertia and viscous break-up are considered and the integral can be derived from known form which render their implementation relatively easy. As a result, this break-up model has been chosen for further investigation.

2.3 Coalescence models

A coalescence event is a feature influencing the size distribution of droplets. Whereas break-up events are mostly due to interactions between droplets and the surrounding fluid, coalescence events can occur from the collision of two or more droplets. Mechanisms of particle coalescence have been reviewed in Liao & Lucas (2010) where the authors have shown that the physical models designed for coalescence events are typically constituted of two distinct methods: the collision frequency between droplets and the coalescence efficiency. Several coalescence models have emerged over the past few years. Among these models, two are often used as references for many numerical studies. The Prince & Blanch (1990) model and the Coulaloglou & Tavlarides (1977) coalescence models. Many other exist and one should refer to Liao & Lucas (2010) for a deep comparison of several coalescence models available in the literature. These models will not be derived here, for the same reason as stated in the previous section (i.e. difficulty of implementation). However, a more recent model (Lo & Rao, 2007) will be explained in details as it was selected fot the numerical simulations presented in this thesis.

Based on the previous findings, a standard method of moments will be used in the current study. The equations of the moments contain unclosed integral terms and therefore, additional modelling is required by assuming an initial (log-normal) distribution of droplets. Such a method has been successfully validated along with break-up and coalescence events in Lo & Rao (2007). The $S-\gamma$ standard method of moments model described in Lo & Rao (2007) will be used to perform numerical simulations of brine droplets in oil inside a horizontal pipeline. This work will be performed with the commercial CFD software StarCCM+ (StarCCM+, 2012). The study will focus on the identification of key parameters influencing the droplet behaviour during their transport. For this purpose, the effects of several drag models will be implemented and tested. The lift, turbulent dispersion and virtual mass force will be discussed. Parameters influencing droplet behaviour in turbulence, break-up and coalescence models parameters will also been investigated. Simulation results of droplet diameters prediction inside a horizontal pipeline will finally be compared and validated against both numerical and experimental results from the literature. The results of this study will permit to identify important parameters to study during a population balance modelling. The implementation of this model in OpenFOAM will be described in Part IV and important aspects that need to be considered for a coupling with solidification solver will be detailed.

Chapter 3

Eulerian-Eulerian model for multiphase flows

An Eulerian-Eulerian model for multiphase flow is presented in this chapter. Mass, momemtum and turbulence equations are derived. Each source term necessary to accurately model the interface between the two fluids are presented and derived. Several drag force models are reviewed and implemented and their behaviour in function of the particle Reynolds number is analysed. Based on these findings, the effect of several drag models on the droplet diameter prediction is investigated further in Chapter 5.

Contents

3.1 Mass and momentum conservation equations **30**
3.2 Turbulence equations **30**
3.3 Interphase source terms modelling **32**
3.3.1 Drag force 32
3.3.1.1 Schiller and Naumann model 34
3.3.1.2 Hamard and Rybczynski model 34
3.3.1.3 Zhang and VanderHeyden model 35
3.3.1.4 Morsi and Alexander model 35
3.3.1.5 Barnea and Mizrahi model 35
3.3.1.6 Ishii and Zuber model 36
3.3.1.7 Kumar and Hartland model 36
3.3.1.8 Snyder et al. model 37
3.3.1.9 Results and discussion 37
3.3.2 Lift force 37
3.3.3 Turbulent dispersion force 39
3.3.4 Virtual mass force 39

3.1 Mass and momentum conservation equations

For the Eulerian-Eulerian model, all phases are assumed to be in an equilibrium state. Each phase has its own velocity, energy and material properties. However, the conservation equations of each phase need closure. This is achieved through the definition of the phase interaction at each phase interface in each control volume. The continuity equation for an Eulerian-Eulerian model, in a general form, is written as shown in Equation 3.1.

$$\frac{\partial \alpha_i \rho_i}{\partial t} + \nabla \cdot (\alpha_i \rho_i \mathbf{u_i}) = \sum_{j \neq i} (K_{ij}^{mass} - K_{ji}^{mass}) + S_i^{mass} \ . \tag{3.1}$$

Subscripts i and j denote the continuous and dispersed phases. The terms α_i, ρ_i, $\mathbf{u_i}$ and S_i^{mass} refer to the volume fraction of phase i, the density of phase i, the velocity vectors of phase i and the mass source term of phase i, respectively. The transfer rates of mass (K_{ij}^{mass} and K_{ji}^{mass}) from one phase to another are both positive. Hence, for keeping the mass balance, the following two relationships have to be satisfied during the computation:

$$\sum_i \alpha_i = 1 \ ; \ \sum_i S_i^{mass} = 0 \ , \tag{3.2}$$

The momentum equations are given in Equation 3.3.

$$\begin{aligned} \frac{\partial \alpha_i \rho_i \mathbf{u_i}}{\partial t} + \nabla \cdot (\alpha_i \rho_i \mathbf{u_i} \mathbf{u_i}) = & -\alpha_i \nabla p + \alpha_i \rho_i \mathbf{g} + \mathbf{M}_i + \mathbf{F}_i^{int} \\ & + \nabla \cdot [\alpha_i (\tau_i + \tau_i^t)] + \sum_{j \neq i} (K_{ij}^{mass} \mathbf{u_j} - K_{ji}^{mass} \mathbf{u_i}) + \mathbf{S}_i^{mom} \ . \end{aligned} \tag{3.3}$$

In Equation 3.3, p stands for the pressure field, $\mathbf{g}$ is the gravitational acceleration vector, F_i^{int} represents the internal forces acting on phase i, and τ_i and τ_i^t are the molecular and turbulent stress tensors, respectively. The term $\mathbf{M}_i$ in Equation 3.3 represents the sum of forces transmitted from one phase to another. This term is usually composed of different forces such as drag ($\mathbf{F}_{ij}^d$), lift ($\mathbf{F}_{ij}^\ell$), virtual mass ($\mathbf{F}_{ij}^{vm}$) and turbulent dispersion ($\mathbf{F}_{ij}^{td}$). The forces acting on the continuous phase due to the dispersed phase must be equal in absolute value to the force acting on the dispersed phase due the continuous phase:

$$\mathbf{F}_{ij} = -\mathbf{F}_{ji} \ . \tag{3.4}$$

The forces constituting the interphase momentum transfer term ($\mathbf{M}_i$) will be derived in the following sections.

3.2 Turbulence equations

The realizable $k - \varepsilon$ turbulence model (Shih et al., 1995) was used in the simulations. This turbulence model has been selected as the StarCCM+ population

balance solver is accessible only through k-ε turbulence formulation. Equations 3.5 and 3.7 below give the transport equation for the turbulent kinetic energy term (k) and the transport equation for the turbulent dissipation term (ε), respectively.

$$\frac{\partial \alpha_i \rho_i k_i}{\partial t} + \nabla \cdot (\alpha_i \rho_i \mathbf{u_i} k_i) = \nabla \cdot \left[\alpha_i \left(\mu_i + \frac{\mu_i^t}{P_{r,k}^t} \right) \nabla k_i \right] + \alpha_i S_{k,i} + \alpha_i \left[E_{k,i} + E_{b,i} - \rho_i \left((\varepsilon_i - \varepsilon_0) + E_{Y,i} \right) \right] + \sum_{j \neq i} (K_{ij}^{mass} k_j^{(ij)} - K_{ji}^{mass} k_i) \ . \quad (3.5)$$

The terms μ_i and μ_i^t denote the molecular and the turbulent dynamic viscosity, respectively. The dimensionless term P_r is the Prandtl number. The production term, E_k, in Equation 3.5, represents the generation of turbulent kinetic energy due to the mean velocity gradient. E_Y stands for the dissipation of turbulent kinetic energy due to the contribution of fluctuating dilatation and ε_0 is the ambient turbulence value in the source terms that counteracts turbulence decay. E_b is the production of turbulent kinetic energy due to buoyancy effects. Finally, S_k is the source term for the turbulent kinetic energy. These terms are expressed as:

$$\begin{aligned} E_k &= \mu^t R^2 - \frac{2}{3}\rho k \nabla \cdot \mathbf{u} - \frac{2}{3}\mu^t (\nabla \cdot \mathbf{u})^2 \ , \\ R &= |\mathbf{R}| = \sqrt{2\mathbf{R} : \mathbf{R}^T} = \sqrt{2\mathbf{R} : \mathbf{R}} \ , \\ \mathbf{R} &= \frac{1}{2}\left(\nabla \mathbf{u} + \nabla \mathbf{u}^T \right) \ , \\ E_b &= \beta \frac{\mu^t}{P_{r,k}^t} (\nabla T \cdot \mathbf{g}) \ , \\ \beta &= -\frac{1}{\rho}\left(\frac{\partial \rho}{\partial T} \right)_p \ , \\ E_Y &= \frac{2k\varepsilon}{u_{Sound}} \ . \end{aligned} \quad (3.6)$$

R stands for the modulus of the mean strain rate tensor, β is the thermal expansion coefficient and T is the temperature. The transport equation for the turbulent dissipation term (ε) can be written as:

$$\frac{\partial \alpha_i \rho_i \varepsilon_i}{\partial t} + \nabla \cdot (\alpha_i \rho_i \mathbf{u_i} \varepsilon_i) = \nabla \cdot \left[\alpha_i \left(\mu_i + \frac{\mu_i^t}{P_{r,\varepsilon}^t} \right) \nabla \varepsilon_i \right] + \alpha_i \left[C_{\varepsilon 1} R \varepsilon + \frac{\varepsilon_i}{k_i} (C_{\varepsilon 1} C_{\varepsilon 3} E_{b,i}) - \frac{\varepsilon_i}{k_i + \sqrt{\nu \varepsilon_i}} C_{\varepsilon 2} \rho_i (\varepsilon_i - \varepsilon_0) \right] + \sum_{j \neq i} (K_{ij}^{mass} \varepsilon_j^{(ij)} - K_{ji}^{mass} \varepsilon_i) + \alpha_i S_{\varepsilon,i} \ , \quad (3.7)$$

where the coefficients of the model are expressed as:

$$\begin{aligned} C_{\varepsilon 1} &= max\left[0.43, \frac{\frac{Rk}{\varepsilon}}{5+\frac{Rk}{\varepsilon}}\right] , \\ C_{\varepsilon 2} &= 1.9 , \\ C_{\varepsilon 3} &= 1 \;\text{ if } E_b \geq 0,\; 0 \;\text{ if } E_b < 0 . \end{aligned} \tag{3.8}$$

Values of the constants used in the terms $C_{\varepsilon 1}$, $C_{\varepsilon 2}$ and $C_{\varepsilon 3}$ are expressed following the common definition of the realizable k-ε model. C_μ is no longer constant in the realizable $k-\varepsilon$ model:

$$\mu^t = \rho C_\mu \frac{k^2}{\varepsilon} , \tag{3.9}$$

with C_μ expressed as:

$$C_\mu = \frac{1}{4.0+\sqrt{6}\cos(\theta)\frac{kU^*}{\varepsilon}}. \tag{3.10}$$

The terms present in Equation 3.10 are defined as:

$$\begin{aligned} \theta &= \frac{1}{3}\cos^{-1}(\sqrt{6}W) , \\ W &= \frac{R_{ij}R_{jk}R_{ki}}{\sqrt{R_{ij}R_{ij}}^3} , \\ U^* &= \sqrt{R:R - W:W} . \end{aligned} \tag{3.11}$$

Subscripts i, j and k refer to the phases i, j and k respectively and W is the rotation rate tensor.

3.3 Interphase source terms modelling

3.3.1 Drag force

Any particle in motion inside a flow experiences a force acting parallel to this incoming flow: the drag force. This force represents the phenomenon where particles tend to follow the fluctuating velocities of the flow. One can distinguish viscous and form drag forces. "The form drag is caused by the variable pressure distribution around the moving particle, associated with its shape and size. The viscous drag is however produced, mainly within the boundary layer, by the viscous stress related to the fluid viscosity" (Wei & Pang, 2011). The respective magnitudes of each one of these contributions vary with the particle Reynolds number. Figure 3.1 gives a representation of the drag force acting on a spherical droplet during a horizontal motion.

It was reported by several researchers that the drag coefficient is related to many factors such as the particle shape, the Weber number, the particle Reynolds number

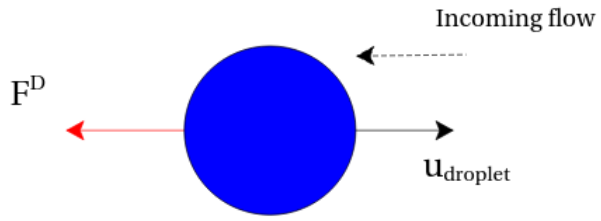

Figure 3.1: Drag force acting on a spherical droplet in horizontal motion due to an incoming flow.

or the Eotvos number among others (Crowe et al. (1998); Takagi et al. (2008)). However, it is found that the majority of the drag coefficient models available in the literature are based on the particle Reynolds number and few of them on the Eotvos number. Moreover, several drag models are only linked to the particle Reynolds number. Recently, the mathematical expression for the drag force has come to an agreement and can, therefore, be expressed in the following general form:

$$F^D = C^D \frac{\rho_c}{2} \pi r_p^2 |\mathbf{u_r}| \mathbf{u_r}. \tag{3.12}$$

Where r_p is the radius of a particle, $\mathbf{u_r}$ is the relative velocity between the different phases and C^D is the actual drag coefficient. In order to take account of eventual non-spherical shape of droplets, any correction can be added to the general expression of the drag force through the drag coefficient. The drag coefficient is therefore expressed as the multiplication of a single-particle drag coefficient (C^D_∞) and a drag correction factor (f^D) which can correct several important parameters such as the droplet size, shape or terminal velocities:

$$C^D = C^D_\infty f^D. \tag{3.13}$$

Several drag correction model are available in the literature. In order to deal with droplet of relatively small diameters (i.e from 1.0×10^{-9} to 1.0×10^{-3} m), the Richardson & Zaki (1997) correction model is the most suitable. As an example, the correction added to the size of the droplet can be modelled through the following expression:

$$f^d = \frac{d}{d_\infty} = \alpha_c^b, \tag{3.14}$$

where b is the Richardson and Zaki exponent. Table 3.1 gives the wide range of application of the method, where d stands for the diameter of the droplet and D for the diameter of the tube. Several models have been used over the past few years to compute the drag coefficient. They are reviewed in the following paragraphs.

TABLE 3.1: Range of values for Richardson and Zaki exponent (b)

Range of Re_∞	b for small tubes	b for large tubes
$Re_\infty < 0.2$	4.65	4.65
$0.2 < Re_\infty < 1$	$\left(4.35 + 17.5\frac{d}{D}\right) Re_\infty^{-0.03}$	$4.35Re_\infty^{-0.03}$
$1 < Re_\infty < 200$	$\left(4.45 + 18\frac{d}{D}\right) Re_\infty^{-0.1}$	$4.45Re_\infty^{-0.1}$
$200 < Re_\infty < 500$	$4.45Re_\infty^{-0.1}$	$4.45Re_\infty^{-0.1}$
$Re_\infty > 500$	2.39	2.39

3.3.1.1 Schiller and Naumann model

The model is based on the drag law of Stokes, which approaches the drag coefficient as $C^D = \frac{24}{\mathrm{Re}_d}$ for $\mathrm{Re} < 1$. Schiller & Naumann (1935) extended the applicability of the model to intermediate Re by means of a dimensionless multiplication factor which accounts for the inertial effects on the drag force. The model is acurate for spherical and non-deformable particles as Klaseboer et al. (2001) have experimentally proved.

The expression of the drag coefficient in the Schiller & Naumann (1935) model is based on the particle Reynold's number defined as follow :

$$\mathrm{Re}_d = \frac{\rho_c |\mathbf{u_r}| d}{\mu_c}, \tag{3.15}$$

where d stands for the particle diameter. The standard drag coefficient is then expressed as:

$$C^D = \begin{cases} \frac{24\left(1+0.15\mathrm{Re}_d^{0.687}\right)}{\mathrm{Re}_d} & \mathrm{Re}_d \leq 1000 \\ 0.44 & \mathrm{Re}_d > 1000 \end{cases} \tag{3.16}$$

3.3.1.2 Hamard and Rybczynski model

Currently, the model of Hamard and Rybczynski is used in the case where viscous Newtonian fluid droplets are dispersed in a second immiscible viscous Newtonian fluid. It is based on the classical drag law of Stokes following the form (Chhabra, 1992):

$$c^D = \frac{24}{\mathrm{Re}_d} A, \tag{3.17}$$

where A stands as a correlation coefficient based on the ratio between the dispersed and continuous phases viscosities defined by:

$$A = \frac{2 + 3\frac{\mu_d}{\mu_c}}{3 + 3\frac{\mu_d}{\mu_c}}. \tag{3.18}$$

This drag model loses its accuracy for high particle Reynolds number where a Schiller & Naumann (1935) scheme is usually preferred (StarCCM+, 2012).

3.3.1.3 Zhang and VanderHeyden model

The drag model developped by Zhang & VanderHeyden (2002) is based on an average particle-scale interaction scheme. The drag force is calculated as a function of the relative velocity between oil and water $\mathbf{u_r}$. The drag coefficient is expressed as:

$$C^D = 0.44 + \frac{24}{\mathrm{Re}_d} + \frac{6}{1+\sqrt{\mathrm{Re}_d}}. \tag{3.19}$$

3.3.1.4 Morsi and Alexander model

The Morsi & Alexander (1972) drag model is similar to the Schiller and Naumann model as it is suitable for smooth and spherical particle shapes. The drag coefficient is expressed as a function of the particle Reynolds number:

$$C^D = a + \frac{b}{\mathrm{Re}_d} + \frac{c}{\mathrm{Re}_d^2}, \tag{3.20}$$

where the values of the constants a, b and c are dependent on the different values for the particle Reynolds number such as:

$$a, b, c = \begin{cases} 0, 24, 0 & 0 < \mathrm{Re}_d < 0.1 \\ 3.690, 22.73, 0.0903 & 0.1 < \mathrm{Re}_d < 1 \\ 1.222, 29.1667, -3.8889 & 1 < \mathrm{Re}_d < 10 \\ 0.6167, 46.50, -116.67 & 10 < \mathrm{Re}_d < 100 \\ 0.3644, 98.33, -2778 & 100 < \mathrm{Re}_d < 1000 \\ 0.357, 148.62, -47500 & 1000 < \mathrm{Re}_d < 5000 \\ 0.46, -490.546, 578700 & 5000 < \mathrm{Re}_d < 10000 \\ 0.5191, -1662.5, 5416700 & \mathrm{Re}_d \geq 10000 \end{cases} \tag{3.21}$$

The different values of the coefficients a,b and c have been chosen to fit a minimum deviation according to experimental data (Yilmaz & Gundogdu, 2009).

Over the past few years, experimental studies on liquid/liquid drag forces revealed that a particular attention has to be made regarding the effects of adjacent entities in the prediction of these drag coefficients. For a high dispersed phase volume fraction $\alpha > 0.05$, these entities have to be taken into account for an accurate prediction of the drag coefficient (Rusche & Issa (2000);Al-Taweel et al. (2006)).

3.3.1.5 Barnea and Mizrahi model

The model of Barnea & Mizrahi (1975) was extended from a solid-liquid drag model. Unlike the previous models, Barnea and Mizrahi used a particle Reynolds number based on the mixture viscosity defined as follows:

$$\mathrm{Re}_{d,m} = \frac{\rho_c \mathbf{u_r} d}{\mu_m}. \tag{3.22}$$

The mixture viscosity μ_m is evaluated following a viscosity law based on two empirical coefficients A_1 and A_2. The mixture viscosity is therefore expressed as:

$$\mu_m = \mu_c A_1 \frac{2A_1 + 3\frac{\mu_d}{\mu_c}}{3A_1 + 3\frac{\mu_d}{\mu_c}}, \tag{3.23}$$

where the empirical coefficients A_1 and A_2 are defined by :

$$\begin{aligned} A_1 &= \exp\left[\frac{5\alpha_d A_2}{3(1-\alpha_d)}\right], \\ A_2 &= \frac{\mu_c + 2.5\mu_d}{2.5\mu_c + 2.5\mu_d}. \end{aligned} \tag{3.24}$$

Therefore, this model becomes suitable for a volume fraction of the dispersed phase $\alpha_d > 0.05$ and the drag coefficient is expressed thanks to the following relationship:

$$C^D = \left(1 + \alpha_d^{1/3}\right)\left(0.63 + \frac{4.8}{\sqrt{\mathrm{Re}_{d,m}}}\right)^2. \tag{3.25}$$

3.3.1.6 Ishii and Zuber model

The Ishii & Zuber (1979) model is comparable to the Barnea & Mizrahi (1975) model as the drag coefficient is a function of the particle Reynolds number of the mixture. However, in this case, the mixture viscosity μ_m is evaluated by a different viscosity law:

$$\mu_m = \mu_c \left(1 - \frac{\alpha_d}{\alpha_{max}}\right)^a. \tag{3.26}$$

For liquid-liquid system the maximum value of the volume fraction of the dispersed phase is fixed at $\alpha_{max} = 1$ and the exponent a is evaluated as:

$$a = -2.5\alpha_{max}\frac{\mu_d + 0.4\mu_c}{\mu_d + \mu_c}. \tag{3.27}$$

Therefore, the drag coefficient (Ishii & Zuber, 1979) can be expressed as:

$$C^D = \frac{24}{\mathrm{Re}_{d,m}}\left(1 + 0.1\mathrm{Re}_{d,m}^{0.75}\right). \tag{3.28}$$

3.3.1.7 Kumar and Hartland model

The model proposed by Kumar & Hartland (1985) is expressed as a function of the particle Reynolds number and has been validated over a large range of experimental data. The drag coefficient can be written as:

$$C^D = \left(0.53 + \frac{24}{\mathrm{Re}_d}\right)\left(1 + 4.56\alpha_d^{0.73}\right). \tag{3.29}$$

3.3.1.8 Snyder et al. model

More recently, Snyder et al. (2007) developed a new drag model based on the particle Reynolds number where the drag coefficient is defined as:

$$C^D = \begin{cases} \frac{24}{\mathrm{Re}_d} & \mathrm{Re}_d < 1 \\ \frac{24}{\mathrm{Re}_d}\left[1 + \frac{3.6}{\mathrm{Re}_d^{0.313}}\left(\frac{\mathrm{Re}_d - 1}{19}\right)^2\right] & 1 \leq \mathrm{Re}_d \leq 20 \\ \frac{24}{\mathrm{Re}_d}\left(1 + 0.15\mathrm{Re}_d^{0.687}\right) & 20 \leq \mathrm{Re}_d \end{cases} \tag{3.30}$$

It is important to note that the models presented previously are all based on the particle Reynolds number. Other models based on the Eotvos number, in particular, are available in the literature. Among all these models, one can find difficult to choose a proper drag coefficient. The purpose of the next section is to analyze numerically these models for liquid-liquid flows.

3.3.1.9 Results and discussion

In order to analyse the different drag models, a theoretical approach is necessary as a first step. The drag coefficient profiles are plotted as a function of the particle Reynolds number and for a constant volume fraction of the dispersed phase such as $\alpha_d = 0.5$. The range of values of the particle Reynolds number has been, primarily, chosen to be $0 < \mathrm{Re}_d < 10$, which corresponds to values encountered in numerous problems. The drag coefficient profiles are analysed between two regions for this range. First the Stokes region, for $\mathrm{Re}_d < 1$, is analysed, where the particle Reynolds number has an high influence on the drag coefficient.

The drag coefficient seems to decrease exponentially with the increase of the particle Reynolds number as shown in Figure 3.2. The analysis is extended in two additional regions for higher particle Reynolds numbers $10 < \mathrm{Re}_d < 200$ and $200 < \mathrm{Re}_d < 1000$, where the drag coefficients seem to reach a constant value as the particle Reynolds number increases.

From Figure 3.2, one can deduce that even if the different drag models presented have different formulations, the drag coefficient profiles remain relatively close. In particular Zhang, Schiller, Snyder and Morsi models show a close behaviour. Larger discrepancies are observed for the model of Kumar, probably due to its formulation. Kumar model takes the volume fraction of the dispersed phase into account. Schiller, Snyder and Zhang drag models seem to be better indicates for this study case, according to Figure 3.2 and have been recommended by Wei & Pang (2011) in a thorough analysis of the current drag models. The Snyder model has been selected in this study as it provides three different drag coefficient formulations depending on the particulate Reynolds number range, whereas the Schiller model uses two and the Zhang model one only.

3.3.2 Lift force

Unlike the drag force expression, the lift force is more difficult to investigate and according to Hibiki & Ishii (2007), more than 20 lift models are currently used.

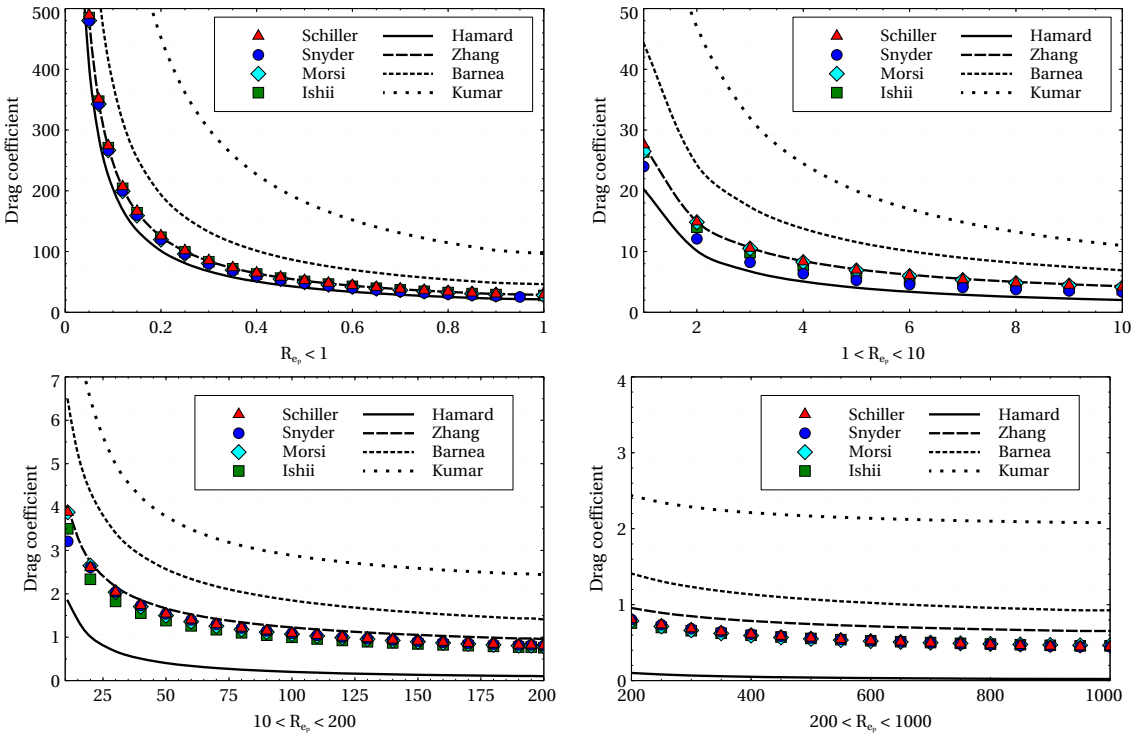

FIGURE 3.2: Drag coefficient as a function of the Particle Reynolds number

However, the following expression, given in a general formulation, based on the surrounding continuous phase vorticity, is widely used:

$$F^{\ell} = \frac{4\pi r^3}{3} C^{\ell} \rho_c \mathbf{u_r} \text{ x } \omega_c. \tag{3.31}$$

Among all available models, those from Saffman (1965), Wang et al. (1987), Mei et al. (1994) and Tomiyama et al. (2002) are widely used. However, the most commonly lift force expression is derived from Auton & Hunt (1988) and it is based on the curl of the continuous phase velocity following:

$$F^{\ell} = \alpha_d C^{\ell} \rho_c \left[\mathbf{u_r} \text{ x } (\nabla \text{ x } \mathbf{u_c}) \right]. \tag{3.32}$$

The lift force may be extremely important in predicting both droplet motion and size in complex multiphase systems. By definition, the lift force acts perpendicular to the relative motion of a droplet. The direction of the force depends, however, on the velocity gradient between the continuous and the dispersed phase. Therefore, this force tends to push the droplets perpendicularly to the main flow direction. In the case of an horizontal flow, the force pushes the droplets towards the walls of the system studied, where shear and turbulence rates are strongest. Hence, the presence of this force can have a significant impact on the droplet size prediction, especially when break-up and coalescence phenomena are considered and known to be closely dependent of both shear stress and turbulence rate. Several researchers also noticed the importance of multiple particle parameters onto the expression of the

lift force such as the rotational and relative speed of the droplet and the shear rate in particular (Ervin & Tryggvason (1997); Magnaudet & Legendre (1997); Hibiki & Ishii (2007); Wei & Pang (2011)). Figure 3.3 shows the representation of a lift force, acting toward the top, on a spherical droplet during a horizontal motion.

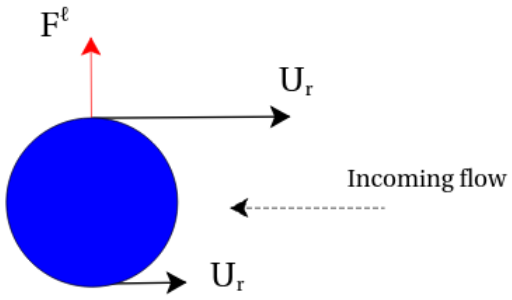

Figure 3.3: Lift force towards the top acting on a spherical droplet.

3.3.3 Turbulent dispersion force

The turbulent dispersion force results from the combined actions of the interphase drag and the turbulent surrounding eddies of the continuous phase. The physical effect of the force results in moving the particles from high to low concentration areas and get transported by the effect of the drag force. This force can have a significant effect on the particle size distribution, in particular when the continuous and dispersed phases have large volume fraction differences and when the drag coefficient plays an important role in the particle motion (Lahey & Lopez (1993); Burns et al. (2004); Lucas et al. (2004)).

The turbulent dispersion force is usually expressed as follows:

$$F_{ij}^{td} = C^D \frac{\rho_c}{2} \frac{a_{ij}}{4} |\mathbf{u_r}| \frac{\nu_c^t}{\sigma_\alpha} \left(\frac{\nabla \alpha_j}{\alpha_j} - \frac{\nabla \alpha_i}{\alpha_i} \right), \tag{3.33}$$

where the first part is deduced from the drag coefficient C^D, the term ν_c^t represents the continuous phase turbulent kinematic viscosity and σ_α is the turbulent Prandtl number, usually taken to be equal to unity. a_{ij} represents the interfacial area density and α_i and α_j the continuous and dispersed phases volume fractions respectively. Figure 3.4 shows a representation of the turbulent dispersion force effect in high concentration regions.

3.3.4 Virtual mass force

When a body inside a fluid domain accelerates, it is likely that some of the surrounding fluid volume will be displaced during its motion. The virtual mass force represents the inertia that is added to the system due to this phenomenon. The virtual mass force contribution to the particles motion can become significant when both continuous and dispersed phases have densities of similar order of magnitude

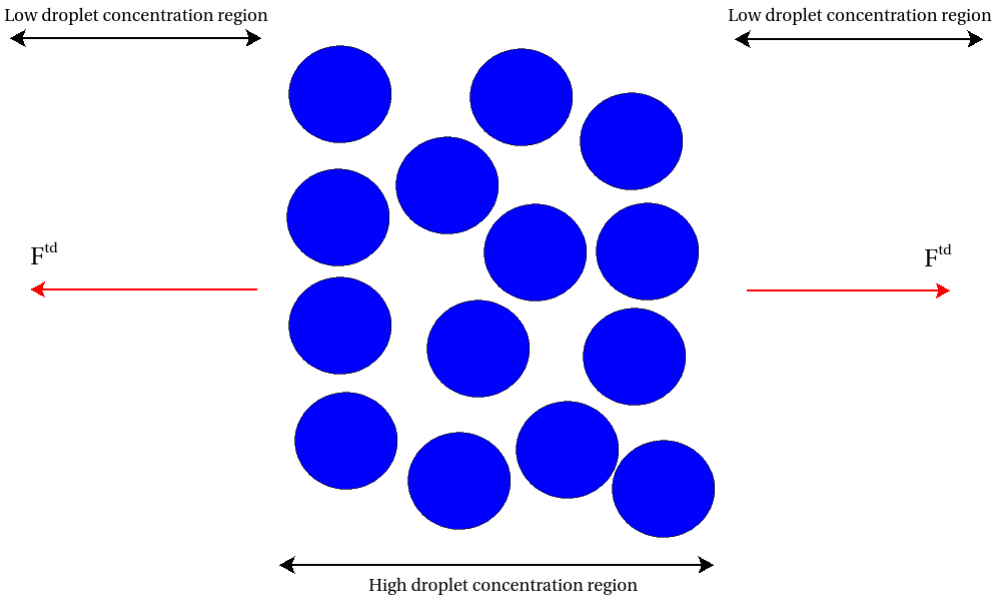

FIGURE 3.4: Turbulence dispersion force acting on high concentration region of droplet.

which is the case for droplets in oil problems (Drew & Lahey (1987); Harlow & Cook (1984)). One common way to approach the virtual mass force is to derive, from a 2-phase flow, the model developed by Auton & Hunt (1988). The force acting on a phase i due to the acceleration relative to a phase j is expressed as:

$$F_{ij}^{vm} = C_{ij}^{vm} \rho_c \alpha_d (\mathbf{a_j} - \mathbf{a_i}), \tag{3.34}$$

where the vectors $\mathbf{a_j}$ and $\mathbf{a_i}$ stand for the accelerations of phase j and i respectively.

When dealing with the virtual mass force, it is important to distinguish which fraction of the surrounding fluid is entrained on the dispersed phase as virtual mass. To overcome this problem, Harlow & Cook (1984) developed the concept of separating the surrounding fluid as a fluid fraction entrained on the dispersed phase and a free stream fraction of fluid (not entrained as virtual mass on the dispersed phase). The concept may be explained in Equation 3.35, where γ represents the fraction of free stream of the fluid:

$$\gamma = \frac{\alpha_c - C^{vm} \sum \alpha_d}{\alpha_c}. \tag{3.35}$$

An upper bound virtual mass coefficient limit, depending on both volume fraction of the continuous phase and minimum fraction of the free stream can then be deduced, by considering that the free stream fluid fraction is always greater than some minimum value γ_{min}:

$$C_{max}^{vm}(\alpha_c, \gamma_{min}) = \frac{\alpha_c}{1 - \alpha_c}(1 - \gamma_{min}) \tag{3.36}$$

A common value for the virtual mass coefficient is 0.5 which is suitable for spherical particles. However, in order to deal with problems where droplets concentrations constantly increase or decrease due to break-up and coalescence phenomena, the Zuber (1964) model can be added. The model developed is based on the analysis of the dispersed volume fraction, within an outer stationary sphere of an accelerating inner sphere, proposed by Lamb (1945). The general formulation of the virtual mass coefficient for a single dispersed phase is:

$$C_{Zuber}^{vm} = 0.5\frac{1+2\alpha_d}{1-\alpha_d}. \tag{3.37}$$

This formulation can be extended to multiphase computations, using the fundamental assumption that $\sum \alpha_d = 1 - \alpha_c$ which leads to:

$$C_{Zuber,ij}^{vm} = 0.5\frac{3-2\alpha_c}{\alpha_c}. \tag{3.38}$$

A common value $\gamma_{min} = -10$ allows the Zuber virtual mass coefficient to be used for the wide range $1 < \sum \alpha_d < 0.66$ before any limitation is applied. Hence, the virtual mass coefficient used in Equation 3.34 becomes:

$$C_{ij}^{vm} = \left[\left(C_{Zuber,ij}^{vm}\right)^{-2} + \left(C_{max}^{vm}\left(\alpha_c, \gamma_{min}\right)\right)^{-2}\right]^{-1/2}. \tag{3.39}$$

Figure 3.5 describes the virtual mass acting on a spherical droplet.

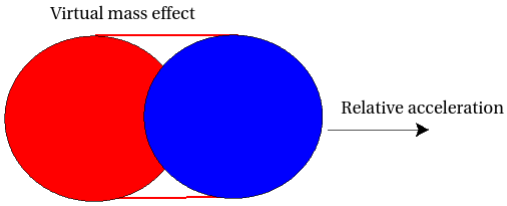

Figure 3.5: Virtual mass during the motion of a spherical droplet.

Chapter 4

Population balance model for particle size prediction

The derivation of a standard method of moment is detailed here. This part of the solver, when coupled with the Eulerian-Eulerian multiphase flow solver described in Chapter 3 permits to characterize the evolution of a population of particles in a given region. Hence, break-up and coalescence models chosen for this study and extracted from the literature review presented in Chapter 2 are detailed thoroughly. Break-up and coalescence mechanisms important for each of the models are also explained.

Contents

4.1 Standard method of moment derivation **43**
4.2 $S - \gamma$ model **45**
4.3 Break-up modelling **47**
4.3.1 Break-up model 47
4.3.1.1 Break-up regimes 47
4.3.1.2 Viscous break-up 48
4.3.1.3 Inertia break-up 49
4.4 Coalescence modelling **49**
4.4.1 Coalescence model 49
4.4.1.1 Viscous collision 49
4.4.1.2 Inertial collision 50

4.1 Standard method of moment derivation

This chapter focuses on mathematical methods currently used, to be able to predict size and population evolution of a given set of particles. The population balance method (PBM), solving the population balance equations (PBE's) stands as the reference method to deal with this field of study (Ramkrishna, 2000). These equations aim at characterizing the evolution of the number of particles in a given region of the domain through time. In an Eulerian formulation, the dispersed phase is often described as a sum of discrete elements composing it. Therefore, each one of the elements is charaterized by a certain amount of properties that are classified as internal (ξ = size, volume, velocity...) or external ($\mathbf{x}$ = spatial coordinates). As such, the discrete elements constituting the dispersed phase can be described as the evolution of the properties of interest through time, thanks to the so-called number density function (NDF) : $n(\mathbf{x}, \xi, t)$. This function clearly identifies the entire population of particles at any instant and any point in the entire computational domain (Marchisio & Fox, 2013). The total number density (N) can be deduced from its formulation by the integration of the NDF through the evolution of the internal properties ξ, as given by Equation 4.1.

$$N(\mathbf{x}, t) = \int_{\Omega_\xi} n(\xi) d\xi. \tag{4.1}$$

As an example, considering a population of particles only characterized by their length L, the relation between the NDF and the total number density becomes:

$$N(\mathbf{x}, t) = \int_{\Omega_\mathbf{L}} n(\mathbf{L}) d\mathbf{L} = \int_0^\infty n(\mathbf{L}) d\mathbf{L}. \tag{4.2}$$

The NDF is used in the population balance equations to approximate the evolution of the particle population properties through time and space. The specific population balance equations for an internal property ξ, an external property $\mathbf{x}$ in a physical space control volume $\Omega_\mathbf{x}$ and a phase space control volume Ω_ξ can be written as:

$$\begin{aligned} &\frac{\partial}{\partial t}\left[\int_{\Omega_\mathbf{x}} d\mathbf{x} \int_{\Omega_\xi} d\xi n(\mathbf{x}, \xi, t)\right] + \int_{\Omega_\xi} d\xi \int_{\Omega_{\mathbf{x_m}}} [n(\mathbf{x}, \xi, t)\mathbf{u}] \cdot d\mathbf{a}_\mathbf{x} \\ &+ \int_{\Omega_\mathbf{x}} d\mathbf{x} \int_{\Omega_{\xi\mathbf{m}}} \left[n(\mathbf{x}, \xi, t)\dot{\xi}\right] \cdot d\mathbf{a}_\xi = \int_{\Omega_\mathbf{x}} d\mathbf{x} \int_{\Omega_\xi} d\xi h(\mathbf{x}, \xi, t). \end{aligned} \tag{4.3}$$

Where $\Omega_{\mathbf{x_m}}$ and $\Omega_{\xi_\mathbf{m}}$ stand for the bounds of the physical space and the phase space control volume respectively, h is a function representing the discrete events occurring in the system and $\dot{\xi}$ is the internal properties velocity in the phase space, due to droplet velocity in the physical space u. In Equation 4.3, the partial derivative gives the droplet accumulation rate in the system. The second term represents the flux of the number density through the domain and the third term computes the

rate of change of a given internal property. PBE's can be referred to as univariate if only one internal property is of interest for the particle population or multivariate whenever more than one internal property is needed. Moreover, if the droplets are characterized by their own velocity distribution instead of a unique common velocity field, a generalized expression for the population balance equation (GPBE) can be deduced from Equation 4.3. In this context, the particle velocity is added in the equation as an internal property of the number density function such as $n(\mathbf{x}, \xi, \mathbf{u}, t)$. The GPBE is given in Equation 4.4.

$$\begin{aligned}\frac{\partial n(\mathbf{x},\xi,\mathbf{u},t)}{\partial t} + \nabla \cdot [n(\mathbf{x},\xi,\mathbf{u},t)\mathbf{u}] + \frac{\partial}{\partial \mathbf{u}} \cdot [n(\mathbf{x},\xi,\mathbf{u},t)\mathbf{a_d}] \\ + \frac{\partial}{\partial \xi} \cdot [n(\mathbf{x},\xi,\mathbf{u},t)\xi] = h(\mathbf{x},\xi,\mathbf{u},t),\end{aligned} \tag{4.4}$$

where $\mathbf{a_d}$ stands for the acceleration of the droplets. The GPBE serves as a starting point for many numerical studies involving population balance modelling. Considering, now, the variable ξ as the unique internal property for an univariate GPBE, Equation 4.4 can be rewritten as:

$$\frac{\partial n(\mathbf{x},\xi,t)}{\partial t} + \nabla \cdot [n(\mathbf{x},\xi,t)\mathbf{u}] + \frac{\partial}{\partial \xi} \cdot [n(\mathbf{x},\xi,t)\xi] = h(\mathbf{x},\xi,t). \tag{4.5}$$

For the sake of simplicity, Equation 4.5 can be rewritten in terms of moments, i.e. the transport equations of interest in a CFD context. The general expression used in most current CFD solvers is the following one:

$$\frac{\partial n(\mathbf{x},\xi,t)}{\partial t} + \nabla \cdot [n(\mathbf{x},\xi,t)\mathbf{u}] + \frac{\partial}{\partial \xi}[\mathbf{G}_\xi n(\mathbf{x},\xi,t)] = h(\mathbf{x},\xi,t), \tag{4.6}$$

where the term containing $\mathbf{G}_\xi$ is the rate change of particle internal property of interest and h represents the discrete events occurring during the transport of the dispersed phase. Usually, Equation 4.6 is even more simplified by considering a source term S for the discrete events such as breakage and coalescence of particles. This will be discussed in the following sections. As a result, and considering, as an example, the length of the droplets to be the only internal property of interest, Equation 4.6 is simplified as:

$$\frac{\partial n(\mathbf{x},\xi,t)}{\partial t} + \nabla \cdot [n(\mathbf{x},\xi,t)\mathbf{u}] = S \tag{4.7}$$

As mentioned previously, the PBE's or GPBE are not closed equations. Therefore, numerical models for closure of the right hand part of both formulations are necessary. As identified during the literature review (Chapter 2), moments based methods will be used to overcome the closure problem of the population balance equations. The method of moments, first introduced by Hulburt & Katz (1964), is a promising alternative to the computational expense induced by the use of common Monte Carlo or class methods.

The method consists in solving the PBE's by tracking the moments of the particle size distribution. Therefore, the moments of the PSD can be obtained through the resolution of Equation 4.8

$$m_k(\mathbf{x},t) = \int_0^\infty n(\mathbf{x},\xi,t)\xi^k d\xi. \tag{4.8}$$

The use of the standard method of moments (SMOM) permits to define the particle size distribution of the system by tracking, only, few lower-order moments. Typically, three to four moments are necessary and are related to important parameters of the droplets such as the diameter, surface area or volume. The ratio between these moments is often used to characterized a population of droplets such as the mean sauter diameter ($d_{3,2}$) or the three-zero diameter ($d_{3,0}$); expressed in Equation 4.9

$$\begin{aligned} d_{3,2} &= \frac{m_3(\mathbf{x},t)}{m_2(\mathbf{x},t)}, \\ d_{3,0} &= \frac{m_3(\mathbf{x},t)}{m_0(\mathbf{x},t)}. \end{aligned} \tag{4.9}$$

Hence, the SMOM, provides a large improvement of the computational efficiency compared to the method of classes. The equations of the moments contain unclosed integral terms and therefore, additional modelling is required to solve a population balance problem through the standard method of moments.

As an example, the transport equation for the 0th moment becomes:

$$\frac{\partial m_0(\mathbf{x},t)}{\partial t} + \nabla\cdot(m_0(\mathbf{x},t)\mathbf{u_d}) = S_{br} + S_{coal}. \tag{4.10}$$

The source terms S_{br} and S_{coal} are related to the source term to account for break-up and coalescence phenomena respectively. Break-up and coalescence terms are a sum of birth and death rate as shown in Equation 4.11

$$\begin{aligned} S_{br} &= S_{br}^{Birth} + S_{br}^{Death}, \\ S_{coal} &= S_{coal}^{Birth} + S_{coal}^{Death}. \end{aligned} \tag{4.11}$$

4.2 $S-\gamma$ model

Moment-based methods can be used to overcome the closure problem of the population balance equations. The $S-\gamma$ model has been used here. This model solves the transport equations for the moments (m) of the diameter size distribution as:

$$m_\gamma = n\int_0^\infty d^\gamma P(d)d(d)\ , \tag{4.12}$$

with γ the order of the moment, n the number of particle per volume, d the particle diameter and $P(d)$ the probability density function of a particle diameter. The $S-\gamma$ model solves the particle size distribution by tracking only the first three moments. It can be deduced that:

$$\begin{aligned} m_0 &= n, \\ m_2 &= n\int_0^\infty d^2 P(d) d(d), \\ m_3 &= n\int_0^\infty d^3 P(d) d(d). \end{aligned} \tag{4.13}$$

The zeroth-moment of the distribution corresponds to the particle number density n. An analogy with solver parameters is obtained for the second and third moments, which leads to:

$$\begin{aligned} m_0 &= n, \\ m_2 &= \frac{A_{if}}{\pi}, \\ m_3 &= \frac{6\alpha}{\pi}. \end{aligned} \tag{4.14}$$

The interfacial density area (A_{if}) is the area available for drag, heat, and mass transfer between each pair of phases in an interaction. From these equations, two mean diameters can be derived: the Sauter mean diameter ($d_{3,2}$) and the three-zero diameter ($d_{3,0}$):

$$d_{3,2} = \frac{6\alpha}{\pi m_2} = \frac{6\alpha}{A_{if}}, \tag{4.15}$$

$$d_{3,0} = \left(\frac{6\alpha}{\pi m_0}\right)^{1/3} = \left(\frac{6\alpha}{\pi n}\right)^{1/3} . \tag{4.16}$$

For closure of the equations of moments, additional modelling is required by assuming an initial distribution of droplets. A log normal distribution (η) is often used following the relationship introduced by Hill (1998):

$$\eta^2 = \ln\left(\frac{d_{32}}{d_{30}}\right) . \tag{4.17}$$

By analogy with Equation 4.6 the following transport equations are solved for each moment γ of the distribution in the $S-\gamma$ model:

$$\frac{\partial m_\gamma}{\partial t} + \nabla\cdot(m_\gamma \mathbf{u}) = S = S_{br} + S_{coal} . \tag{4.18}$$

The right hand-side of this equation contains the source terms responsible for break-up S_{br} and coalescence S_{coal} during the droplet transport. Break-up and coalescence terms are a sum of birth and death rates, as expressed in Equation 4.11.

4.3 Break-up modelling

4.3.1 Break-up model

By integrating the effects of a droplet of diameter d over all diameters, the source terms for the break-up phenomena can be found. This break-up formulation is expressed in Equation 4.19, following Lo & Zhang (2009):

$$\frac{dm_\gamma}{dt} = \int_{\ell_l}^{u_l} nP(d)\frac{N(d)^{(1-\gamma/3)} - 1}{\tau(d)} d^\gamma d(d) \ , \tag{4.19}$$

where, u_ℓ and ℓ_ℓ are the upper and lower limits respectively and $N(d)$ represents the number of daughter droplets produced during the break-up of a mother droplet. $P(d)$ is the probability density function defined as:

$$P(d) = \frac{1}{d\dot{w}\sqrt{2\pi}} \ exp\left[-\frac{(\ln(d) - \ln(\dot{m}))^2}{2\dot{w}^2}\right] \ , \tag{4.20}$$

which describes the log-normal distribution used to characterise the droplet size distribution defined by a mean $\dot{m}$ and a width $\dot{w}$.

4.3.1.1 Break-up regimes

Break-up events only occur if the droplet has a diameter larger than a critical diameter d_{crit}. Both viscous and inertial break-up regimes can be considered, using the equations from Hill (1998). Depending on the value of the critical diameter and the flow conditions, one or both break-up regimes can be obtained. In this case, integration bounds in Equation 4.19 become:

$$\begin{cases} \text{Viscous break-up (laminar flows)} & \ell_l = d_{crit} \ , \ u_l = \infty \ , \\ \text{Viscous break-up (turbulent flows)} & \ell_l = d_{crit} \ , \ u_l = L_k \ , \\ \text{Inertial break-up} & \ell_l = q \ , \ u_l = \infty \ . \end{cases} \tag{4.21}$$

Viscous break-up events can happen in turbulent flows if the droplets critical diameter d_{crit} is smaller than the Kolmogorov length scale defined as:

$$L_k = [\frac{\nu^3}{\varepsilon}]^{1/4}, \tag{4.22}$$

where ν is the kinematic viscosity and ε is the dissipation rate of turbulent kinetic energy. In addition, for inertial break-up, the lower limit ℓ_l of the integration is equal to a variable q which is the greater value between the critical diameter and the Kolmogorov length scale. Considering $S_{br_{in}}$ and $S_{br_{vi}}$ the contributions of inertial and viscous break-up source terms respectively, the break-up regimes can be distinguished as reported in Table 4.1.

TABLE 4.1: Break-up regimes and bounds of the integration

Condition over d_{crit}	Flow nature	Break-up regime	Integration bounds
-	Laminar	$S_{Br} = S_{Br_{vi}}$	$\ell_l = d_{crit}$, $u_l = \infty$
$d_{crit} < L_k$	Turbulent	$S_{Br} = S_{Br_{in}} + S_{Br_{vi}}$	$\ell_l^{vi} = d_{crit}$, $u_l^{vi} = L_k$
			$\ell_l^{in} = L_k$, $u_l^{in} = \infty$
$d_{crit} > L_k$	Turbulent	$S_{Br} = S_{Br_{in}}$	$\ell_l = d_{crit}$, $u_l = \infty$

4.3.1.2 Viscous break-up

The viscous break-up model computes the effects of the viscosity of the fluid on the break-up of the particles considered. Two main parameters are used to model break-up phenomena: the critical diameter (d_{crit}) and the break-up timescale $\tau(d)$. The critical diameter is computed as follows (Hill (1998); Lo & Zhang (2009)):

$$d_{crit} = \frac{2\sigma C_{a_{crit}}}{\mu_c \chi} \ , \tag{4.23}$$

with σ the surface tension. The shear rate χ, is computed differently, depending on the nature of the flow. For laminar flows, it is calculated from the local velocity gradient whereas for turbulent flows, the local Kolmogorov shear rate is used:

$$\chi = \sqrt{\frac{\varepsilon \rho_c}{\mu_c}} \ . \tag{4.24}$$

The capillary number C_a represents the effects of viscous forces versus surface tension (σ) at the interphase. A common mathematical formulation is:

$$C_a = \frac{\mu_c d \chi}{2\sigma} \ . \tag{4.25}$$

For viscous break-up events, the break-up timescale (Equation 4.26) is a function of the viscosity ratio between the phases and whether (or not) the flow is rotational. The general break-up criterion is then such as $C_a \geq C_{a_{crit}}$. The break-up timescale can be computed with:

$$\tau(d) = \frac{\mu_c d}{\sigma} f\left(\frac{\mu_d}{\mu_c}\right) \ , \tag{4.26}$$

where

$$\log f\left(\frac{\mu_d}{\mu_c}\right) = \delta_0 + \delta_1 \log\left(\frac{\mu_d}{\mu_c}\right) + \delta_2 \left[\log\left(\frac{\mu_d}{\mu_c}\right)\right]^2 \ , \tag{4.27}$$

with δ_0, δ_1 and δ_2 constants correlated from experimental data of Hill (1998).

4.3.1.3 Inertia break-up

The inertia break-up is related to the inertia forces that can induce a break-up during droplets motion. The critical diameter and break-up timescale are calculated as follows (StarCCM+, 2012):

$$\begin{aligned} d_{crit} &= 5.6 \left[\frac{2\sigma W_{e_{crit}}}{\rho_c}\right]^{3/5} \epsilon^{-2/5} \ , \\ \tau(d) &= 0.4\pi \left[\frac{3\rho_d + 2\rho_c}{192\sigma}\right]^{1/2} d^{3/2} \ . \end{aligned} \tag{4.28}$$

The Weber number (W_e) characterizes the shape of droplets travelling at slip velocity and their susceptibility to break-up. It is the ratio of the dynamic pressure around the droplet and the surface tension:

$$We = \frac{\rho_c \varepsilon^{2/3} d^{5/3}}{2\sigma} \ . \tag{4.29}$$

Hence, the inertial break-up occurs when $W_e \geq W_{e_{crit}}$, where the critical Weber number is based on the critical Reynolds number, function of the critical diameter of the droplets.

The critical diameter d_{crit} and the number of fragments $N(d)$ are two important parameters for the calibration of the break-up model used.

4.4 Coalescence modelling

4.4.1 Coalescence model

The coalescence model used here, described in Lo & Rao (2007), is based on a standard method of moments. It considers the probability of collision of droplets, the contact time of two colliding droplets as well as the drainage time of the liquid film between them. This model uses an equivalent diameter d_{eq} for each moment from which the expression of the source term for coalescence event can be obtained (Lo & Zhang, 2009):

$$\frac{dm_\gamma}{dt} = C_{coll}(2^{\gamma/3} - 2) K_{coll} P_{coll}(d_{eq}) d_{eq}^{\gamma}. \tag{4.30}$$

4.4.1.1 Viscous collision

The collision of two droplets produces their interaction for a lapse of time. During this time, the film of the continuous phase between these two colliding drops will start to drain. If this drainage is less than the critical film thickness f_{crit}^{th}, coalescence occurs. Otherwise, droplets separate (Azzopardi et al., 2011). For viscous collisions, the viscous collision rate K_{coll}^{vi} is evaluated as:

$$K_{coll}^{vi} = \sqrt{\frac{8\pi}{3}} (\chi d_{eq}) d_{eq}^2 \left(\frac{6\alpha}{\pi d_{eq}^3}\right)^2 \ . \tag{4.31}$$

The term describing the probability of collision leading to coalescence, $P_{coll}(d_{eq})$, is expressed, in the case of a viscous coalescence $P^{vi}_{coll}(d_{eq})$, as (Lo & Zhang, 2009):

$$P^{vi}_{coll}(d_{eq}) = exp^{(-t_{drain}\chi)}, \tag{4.32}$$

where t_{drain} is the drainage time. Several models are available for the computation of the drainage time; they are listed in Table 4.2, from the fastest drainage time model (largest coalescence rate) to the slowest.

TABLE 4.2: Drainage time models

Type of model	Formulation	Time state
Partially mobile interface	$t_{drain} = \frac{\pi\mu_d\sqrt{F_{coll}}}{2f^{th}_{crit}}\left(\frac{d_{eq}}{4\pi\sigma}\right)^{3/2}$	Quasi-steady state
Partially mobile interface	$t_{drain} = \frac{3}{2}\frac{F_{coll}d^2_{eq}\sqrt{\mu_d\rho_d}}{32\pi\sigma^2 f^{th}_{crit}}$	Short collision time
Fully immobile	$t_{drain} = \frac{3\mu_c d^2_{eq}F_{coll}}{64\sigma^2\pi\left(f^{th}_{crit}\right)^2}$	-

The collision force (F_{coll}) in Table 4.2 is expressed as:

$$F_{coll} = \frac{3}{2}\pi\mu_c\chi d^2_{eq} \ . \tag{4.33}$$

The critical film thickness f^{th}_{crit} is deduced from the evaluation of the Hamaker constant A_H (Hamaker, 1937). The default value is $A_H = 5.10^{-21}$:

$$f^{th}_{crit} = \left[\frac{A_H d_{eq}}{24\pi\sigma}\right]^{1/3} \ . \tag{4.34}$$

4.4.1.2 Inertial collision

During inertial collisions, oscillations on the droplets shape may have a dominant influence on the local velocity in the film. The probability of coalescence is determined from the phase difference between the oscillating droplets, as discussed in Lo & Zhang (2009). Hence, the inertial collision rate K^{in}_{coll} and the probability of inertial collision $P^{in}_{coll}(d_{eq})$ can be expressed respectively as:

$$K^{in}_{coll} = \sqrt{\frac{2\pi}{5}}(\varepsilon d_{eq})^{\frac{1}{3}}\frac{36\alpha^2}{\pi^2 d^4_{eq}} \ , \tag{4.35}$$

$$P_{coll}^{in}(d_{eq}) = \left(\frac{\Phi_{max}}{\pi}\right)\sqrt{1 - \frac{161.3(We - 0.8We_{crit})^2}{\Phi_{max}^2}}\ , \tag{4.36}$$

where Φ_{max} is the maximum phase difference.

$$\Phi_{max} = \frac{137.8 f_{crit}^{th} \rho_c \sigma}{0.8 We_{crit} \mu_d^2 d_{eq}}\ . \tag{4.37}$$

Chapter 5

Parametric study of model parameters influencing droplet size prediction

This chapter presents the numerical simulation performed with the solver Star-CCM+. An Eulerian-Eulerian model has been used to evaluate the evolution of droplet diameter dispersed in a continuous oil phase, initially injected at the inlet of a horizontal pipe with a given diameter. Break-up and coalescence events are of interest to accurately compute the evolution of droplet diameters. Numerical simulations will be compared to both experimental and numerical results, performed with the solver StarCD. The initial conditions, mesh independence study, effects of drag, lift, turbulent dispersion and virtual mass forces, turbulence models and break-up and coalescence models parameters are evaluated. Finally thorough comparison with experimental data are performed under several different flow conditions. This study permits to highlight key parameters necessary for accurate PBM simulations.

Contents

5.1 Numerical campaign **54**
5.2 Grid independence study **54**
5.3 Interphase forces effect **55**
5.4 Turbulence model effects **56**
5.4.1 Realizable 2-layer k-ε model 56
5.4.2 Turbulence response model 58
5.4.3 Results and discussions 58
5.5 Analysis of different drag models **59**
5.5.1 Results and discussion 60
5.6 Break-up model effect **60**
5.6.1 Droplets generation during break-up 61
5.6.2 Influence of the critical diameter value 61
5.7 Coalescence model effect **63**
5.8 Parametric study summary **63**

5.1 Numerical campaign

The test case selected for this study has been taken from Simmons & Azzopardi (2001) experiments. During their experiments they have conducted multiple test cases for droplets dispersed in oil in both horizontal and vertical pipes. By injecting droplets near the inlet of the pipe with several diameters, they were able to capture the evolution of the droplet diameter travelling through the pipe. In particular, the distribution of the droplet diameters at the outlet was analysed with two optical measurement techniques: backscatter technique using a Par-Tec 300C and a diffraction technique using a Malvern 2600.

The experiments were conducted in a 4.5 m long pipe where droplets were transported by an oil continuous phase within a diameter conduit of 63 mm. The dispersed phase used was an aqueous potassium carbonate solution, slightly heavier than water, to represents the salted water. The continuous phase selected is kerosene and the interfacial tension has been set, according to experiments, to $\sigma = 0.01\ N/m$.

Table 17.1 gives the material properties of the two phases used in the experiments.

TABLE 5.1: Material properties of the two phases

Phase	Type	$\rho\ [Kg.m^{-3}]$	$\mu\ [kg.m^{-1}.s^{-1}]$	u $[m.s^{-1}]$	α [%]
Kerosene	Continuous	797	0.0018	2.393	93.8
Aqueous potassium	Dispersed	1166	0.0016	0.158	6.2

In order to minimize the formation of dispersion at the inlet, a special inlet arrangement for the experiment has been designed. The droplets are introduced in the pipe through perforated hole in the wall near the inlet. This inlet arrangement allows the droplets to be created by turbulence and mixing within the pipe, where they start their motion in regions where turbulence and break-up rates are strongest. To accurately represent this inlet arrangement, the inlet of the computational domain has been separated into two sections, following Lo & Rao (2007) recommendations who conducted the same sort of numerical analysis of this case. Hence, the droplets are injected in the computational domain through a ring close to the wall only whereas the center of the pipe is filled with kerosene only. During the experiments, different initial droplet diameters were used, from 750, 1000 and 1500 μm. It has been shown by Simmons & Azzopardi (2001) and Lo & Rao (2007) that within this range of diameters, only little difference on the result appears. Therefore, for this particular study, the effect of the initial droplet diameter can be neglected. For the numerical simulation presented in this chapter, a standard initial diameter of 1000 μm was used.

5.2 Grid independence study

A thorough mesh independence study has been performed on the computational domain. Three different mesh distributions over the length of the domain (+ x

direction) have been primary used to analyse the evolution of the mixture velocity and the turbulence quantities (both turbulent dissipation and kinetic energy rate). Good agreements over the profiles of these quantities for the three different distributions have been observed. The mesh independence study has been carried out to investigate the influence of the cell distribution on the surface of the pipe. Each mesh used is refined in the boundary layer near the wall to capture accurately both wall shear stress and turbulence quantities. The addition of a boundary layer near the wall is extremely important to capture accurately break-up events, which occur mainly in the boundary layer. Table 5.2 gives the characteristics of the 5 meshes used to carry out this study.

Table 5.2: Characteristics of the six grid system for mesh independence study

Grid	Cell number	Cell distribution
M_1	100000	500 x 200
M_2	190000	950 x 200
M_3	250000	1250 x 200
M_4	420000	2100 x 200
M_5	630000	3150 x 200

This study has shown that a similar profiles are obtained for the meshes M_4 and M_5. For the sake of simplicity, they will not be displayed here. The coarser mesh (M_4) has therefore been chosen to carry out the numerical study so that maximum computational time efficiency is obtained.

5.3 Interphase forces effect

As previously explained, drag, lift, turbulent dispersion and virtual mass forces can have a major impact on both droplet diameter and motion predictions. Using different combinations of these four forces, the mean Sauter diameter of the droplets is plotted in Figure 5.1 in function of the vertical position on a plane section close to the outlet of the pipe.

Figure 5.1 shows that similar droplet diameter predictions are obtained from the bottom to the middle of the pipe for the four combinations of force contributions. However, discrepancies are visible near the top region of the pipe. The combination of drag, turbulent dispersion and drag, turbulent dispersion, virtual mass predict approximatively the same droplet diameter near the top part of the pipe. However, as soon as the lift force contribution is added to the model, the minimum droplet diameter prediction falls down. Experiments of Simmons & Azzopardi (2001) have led to a distribution of diameter in the range $0 < d < 1000$ μm whereas the previous computation shows a distribution range of $500 < d < 800$ μm without contribution of the lift force and $300 < d < 800$ μm when the lift force is added to the model.

The lift force contribution is here extremely important. Since the lift force acts perpendicularly to the motion of the droplets, it tends to push the droplets toward the top wall of the pipe where wall shear stress and turbulence are the strongest. The

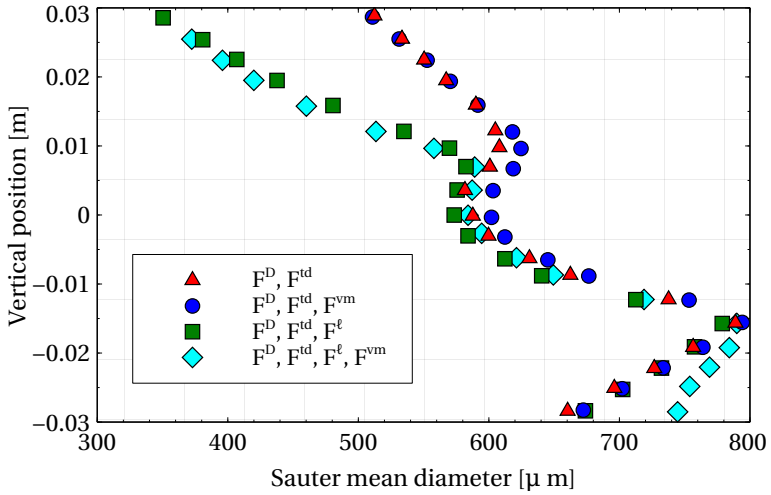

FIGURE 5.1: Influence of drag (F^D), turbulent dispersion (F^{td}), lift (F^ℓ) and virtual mass (F^{vm}) forces on the prediction of the droplet diameter in a plane section of the pipe. Experimental work shows particle diameters in the range $0 < d_{exp} < 1000$ μm

phenomenon enhances break-up which leads to a better prediction of the minimum size of the droplets near the top wall of the pipe when the lift force contribution is added to the model.

The contribution of the turbulent dispersion force to the model resides in the motion of the droplets in the pipe. Since all droplets are injected in the ring near wall section, a large difference of volume fraction occurs between this region and the center of the pipe, where only kerosene is injected in the domain. The definition of the turbulent dispersion force leads to the fundamental result that the particles tend to move from high concentration regions to low concentration regions. This has been observed during the numerical simulations. Near the inlet, as the droplets are entrained by the continuous kerosene phase, they tend to move towards the center of the pipe where the droplet concentration is lower than near the wall of the pipe.

Impact of the drag, lift and turbulent dispersion forces onto the prediction of the droplet diameters has been demonstrated. Several drag models have been implemented and tested; results will be discussed later on in this chapter. The contribution of the virtual mass force is less apparent than the other forces. It may be due to the fact that the acceleration of both dispersed and continuous phase is relatively small. Since the particle diameter prediction is closely linked to both break-up and coalescence rates, which are related to turbulence quantities, an analysis of different turbulence models is performed in the following section.

5.4 Turbulence model effects

5.4.1 Realizable 2-layer k-ε model

The previous analysis were performed using the k-ε model provided by the multiphase segregated flow solver. To improve robustness of the model, the realizable 2-

layer k-ε models has been used. The model gains the flexibility of an all y^+ treatment. Using this model of turbulence for the two phases permits to improve the stability of the computation compared to those performed with the standard k-ε model. The two-layer formulation permits to blend a one-equation model, solving only for the turbulent kinetic energy k but prescribing the dissipation rate ε algebraically (StarCCM+, 2012). The 2-layer model becomes a function of the turbulent Reynolds number Re_y and the distance from the wall y such as :

$$l_\varepsilon = f(y, \mathrm{Re}_y), \tag{5.1}$$

where the turbulent Reynolds number is defined as:

$$\mathrm{Re}_y = \frac{\sqrt{k} y \rho}{\mu} \tag{5.2}$$

Therefore, the dissipation rate of turbulent kinetic energy can be computed as a function of the 2-layer model length scale function such as:

$$\varepsilon = \frac{k^{3/2}}{l_\varepsilon} \tag{5.3}$$

To recover the full 2-equation model from the use of the 2-layer approach, a blending function suggested by Jorgen (1998) is used:

$$\lambda = \frac{1}{2}[1 + \tanh(\frac{\mathrm{Re}_y - \mathrm{Re}_y^*}{A})], \tag{5.4}$$

where Re_y^* is defined as the limit of applicability of the 2-layer formulation and A stands for the width of the blending function. The constant A can be approximated by the analyse of the variation of the turbulent Reynolds number:

$$A = \frac{|\Delta \mathrm{Re}_y|}{atanh\ 0.98}. \tag{5.5}$$

Similarly to Equation 5.4, the turbulent viscosity is blended to a full 2-equation model as:

$$\mu_t = \lambda \mu_t|_{k-\varepsilon} + (1-\lambda)\mu(\frac{\mu_t}{\mu})_{2\ layer}. \tag{5.6}$$

The 2-layer formulation has been chosen due to its efficiency to accurately compute turbulent quantities for intermediate meshes ($1 < y^+ < 30$) where the y^+ computed during these simulations were spread from $4 < y^+ < 9$. The all y^+ treatment as a wall function has also been added to the model. This hybrid scheme combines low and high y^+ treatment to increase the range of applicability. The realizable k-ε model has been preferred over the standard k-ε due to its ability to express the critical coefficient C_μ as a function of the mean flow rather than being constant. In the standard k-ε model, the C_μ value is usually equal to 0.09. In the realizable k-ε model however, C_μ is no longer constant (see Section 3.2 and Equation 3.10). For the calibration of the turbulence model, the turbulent length scale is computed according to the fully-developed flow in pipe assumption ($\ell = 0.038 D_H = 0.0024$) and the turbulent intensity is given by $I = 0.16 \mathrm{Re}_c^{-1/8} = 0.04$. Even if the turbulence model initially chosen leads to relatively satisfactory results, a turbulence response model is more appropriate for multiphase interactions to treat the dispersed phase turbulence.

5.4.2 Turbulence response model

The turbulence response model predicts the velocity fluctuations in the dispersed phase using algebraic correlations of the velocity fluctuations of the continuous phase (Issa & Oliveira, 1994). The turbulence of the dispersed phase is extrapolated from the solution of the continuous phase. The model is based on the evaluation of a turbulent response coefficient C_t which defines the interaction between the phases by the analysis of the ratio between dispersed and continuous velocity fluctuation:

$$C_t = \frac{u_d^{'}}{u_c^{'}}. \tag{5.7}$$

The dispersed phase turbulent eddy viscosity is then expressed, thanks to the turbulent response coefficient as:

$$\mu_d^t = \frac{\rho_d}{\rho_c} C_t^2 \mu_c^t. \tag{5.8}$$

The same sort of relationship is used to approximate the turbulent kinetic energy k and the turbulent dissipation rate ε.

In order to accurately represent the turbulence quantities affecting the droplets, a volume fraction correction to this turbulent response coefficient has been formulated by Rusche et al. (2004):

$$C_t = 1 + (C_t^* - 1)^{-f(\alpha_d)}. \tag{5.9}$$

The volume fraction correction function $f(\alpha_d)$ is given by:

$$f(\alpha_d) = 180\alpha_d - 4.71 \text{ x } 10^3 \alpha_d^2 + 4.26 \text{ x } 10^4 \alpha_d^3. \tag{5.10}$$

The coefficient C_t^* is expressed from Wang (1994):

$$C_t^* = \frac{3+\beta}{1+\beta+2\frac{\rho_d}{\rho_c}}, \tag{5.11}$$

and β follow the expression:

$$\beta = \frac{2L_{ij}^D l_\varepsilon^2}{\alpha_d \mu_c \mathrm{Re}_t}, \tag{5.12}$$

where

$$l_\varepsilon = C_\mu \frac{k_c^{3/2}}{\varepsilon_c}, \tag{5.13}$$

$$\mathrm{Re}_t = \frac{\sqrt{\frac{2k_c}{3}} l_\varepsilon \rho_c}{\mu_c}. \tag{5.14}$$

5.4.3 Results and discussions

The realizable 2-layer k-ε model is used to model the turbulence of the kerosene continuous phase. The dispersed phase turbulence is treated alternatively with a realizable 2-layer k-ε model as in the previous section and with the Issa turbulence response model. The results obtained for these 2 turbulence models are shown in Figure 5.2 for the dispersed phase. To maintain consistency in the post-treatment,

the mean Sauter diameter of the droplets is analysed in the same plane section as shown in the previous section. The turbulent kinetic energy rate is also provided to understand the correlation between the turbulence model and the size of the droplets.

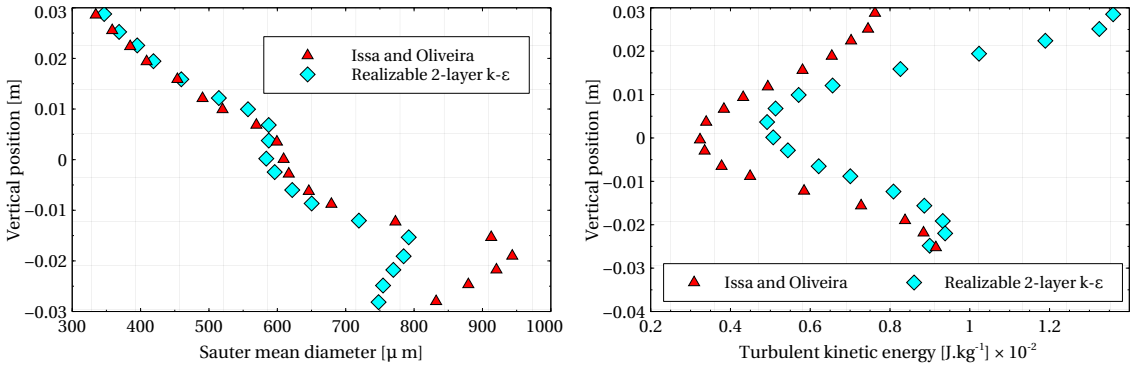

a) Sauter mean diameter distribution

b) Turbulent kinetic energy distribution

Figure 5.2: Turbulence model study

Figure 5.2 shows that the Issa turbulence response model leads to smaller values of the turbulence kinetic energy than the realizable 2-layer k-ε model. It is difficult to establish which model provides the best physical representation of the turbulent quantities since no experimental or numerical results are available for comparison. However, the Issa turbulence response model, due to the under-prediction of the turbulent kinetic energy compared to the realizable 2-layer k-ε, is more efficient in capturing the larger droplet diameters (Figure 5.2 (left)). This model provides a range of droplet diameters from $300 < d < 950$ μm when the realizable 2 layer k-ε model gives a spread of droplet diameters from $300 < d < 800$ μm which is less accurate compared to the experimental data of Simmons & Azzopardi (2001) who computes droplet diameters in the range $0 < d < 1000$ μm. For the dispersed phase, the Issa turbulence model is therefore preferred over the realizable 2 layer k-ε model. This model will therefore be used in the current study.

However, none of the 2 models tested seems to predict accurately the minimum size of the droplet diameters. To improve the results and to investigate the cause of the over- prediction of the droplet diameters, two parameters, supposed to be responsible for the over-estimation of the minimum droplet diameters, will be investigated in the next parts of this chapter: drag and break-up models.

5.5 Analysis of different drag models

Several drag models have been implemented and tested in StarCCM+, to provide a better understanding of the drag force contribution to both droplet motion and diameter prediction. These models have been derived in Section 3.3.1 and are compared to the Schiller and Naumann model used for previous simulations discussed on this chapter. The models implemented for further investigations are the Kumar

& Hartland (1985), Chhabra (1992), Zhang & VanderHeyden (2002) and Snyder et al. (2007) models.

5.5.1 Results and discussion

These four models are implemented in StarCCM+ and used in the numerical simulations. Figure 5.3 presents the drag coefficient profile and the mean sauter diameter of the droplets obtained in this study.

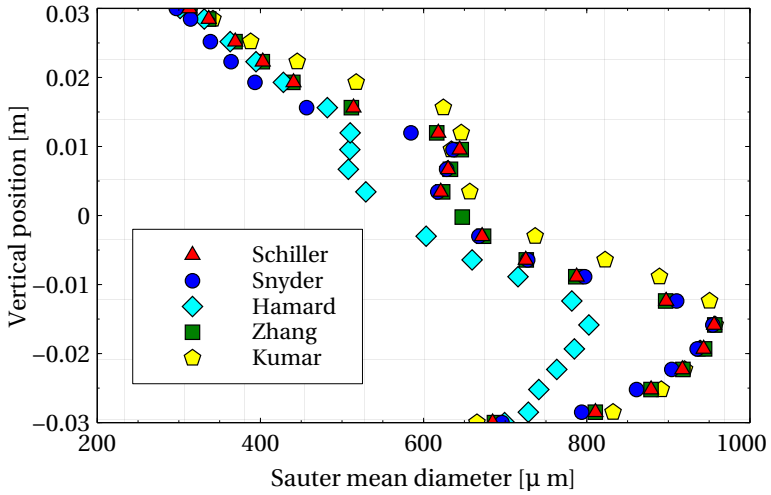

FIGURE 5.3: Numerical drop size prediction for different drag models. Experimental work shows particle diameters in the range $0 < d_{exp} < 1000$ μm

As expected, the models of Zhang, Schiller and Snyder give similar results. The Snyder drag model is probably the most suitable for this study as it allows a slight increase of the range of droplet diameters computed and provides a better minimum size of droplets at the pipe outlet section. Large discrepancies are however visible for the Hamard and the Kumar models when compared to the three remaining models.

Particle Reynolds numbers associated with this case are in the range $0 < \mathrm{Re}_d < 3$. The Snyder drag coefficient distinguishes whether or not the droplets are in the Stokes region (this is not the case for either the Schiller or the Zhang model). For these reasons, this drag model has been selected for further investigation in this PhD. As the particle diameter prediction is closely linked to break-up and coalescence rates, an analysis of different break-up model effect is performed in the following section.

5.6 Break-up model effect

It has been shown so far that the numerical models are not able to capture efficiently the minimum diameter of the droplets. Even if results have been slightly improved with different drag formulations, the break-up model needs enhancement. Two critical parameters are analyzed: the number of fragments that a droplet can

break into, $N(d)$ and the critical diameter (d_{crit}) which is the maximum diameter before break-up.

5.6.1 Droplets generation during break-up

In the previous numerical simulations, the number of fragments was assumed to be binary ($N(d) = 2$). A mother droplet could only break into 2 daughter droplets of equal size. Several numerical simulations are described here, to analyse the influence of the number of child droplets generated during break-up events on the global diameter of the droplets. Four additional numerical simulations are performed and displayed in Figure 5.4 for the following range of $N(d)$:

$$N(d) = i \text{ for } i = [3, 4, 5, 6] \tag{5.15}$$

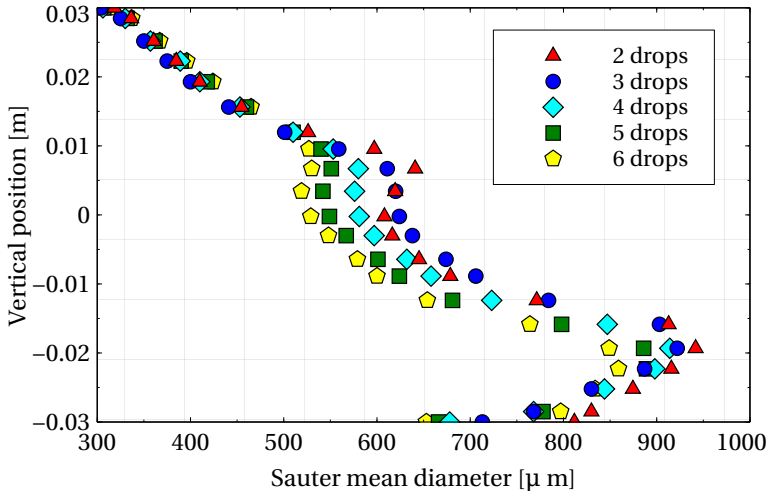

Figure 5.4: Sauter mean diameter estimates depending on the number of child droplet produced during break-up events. Experimental work shows particle diameters in the range $0 < d_{exp} < 1000$ μm

The results show that little difference is present when increasing the number of child droplets produced during break-up events. The number of childs produced does not seem to have a major impact on their average diameters. In general, increasing the number of droplet produced leads to a slight decrease of the maximum droplet diameter obtained without decreasing significantly the diameter of the smallest droplets. Therefore, a binary fragmentation is recommended and will be used for further numerical simulations.

5.6.2 Influence of the critical diameter value

The critical diameter d_{crit} permits to calibrate the break-up model by specifying a critical droplet diameter value from where a break-up event will occur. Hence, if $d > d_{crit}$ during the simulation, then a droplet of diameter d will break into child droplets. The value of the critical diameter is computed as a function of turbulent

quantities and a critical Weber number:

$$d_{crit} = 5.6 \left[\frac{2\sigma W_{e_{crit}}}{\rho_c} \right]^{3/5} \varepsilon^{-2/5}. \tag{5.16}$$

The value of the critical Weber number is difficult to define and can only be affected to a constant value in StarCCM+. Following Lo & Rao (2007), the critical Weber number has been set to $W_{e_{crit}} = 0.23$ for the previous computations. It is important to state that during the numerical simulations using Star-CD (Lo & Rao, 2007), this critical Weber number has been implemented as a function of the critical Reynolds number, such as:

$$W_{e_{crit}} = \begin{cases} \frac{0.069}{\mathrm{Re}_{crit}} & \mathrm{Re}_{crit} < 0.3 \\ 0.23 & \mathrm{Re}_{crit} > 0.3 \end{cases}$$

Due to software limitations, including the fact that only a constant critical Weber number value can be specified, several independent numerical simulations have been performed with different critical Weber number values, leading to a large range of critical diameter obtained via Equation 5.16. Figure 5.5 presents the results obtained for different critical Weber numbers.

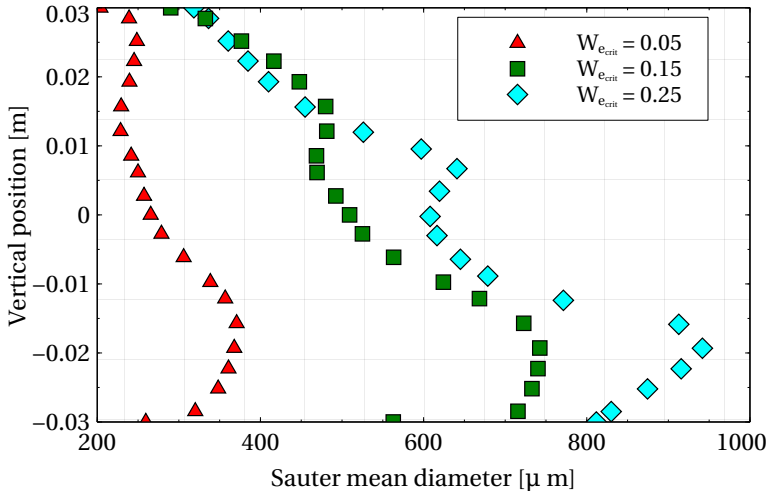

FIGURE 5.5: Sauter mean diameter estimation depending on the value of the critical Weber number. Experimental work shows a range of particle diameter such as $0 < d_{exp} < 1000$

It can be seen that, for a given coalescence drainage time model (in this case the fully immobile scheme, from Table 4.2), the value of the critical Weber number plays an important role in the droplet diameter prediction. For a given value of $W_{e_{crit}}$ close to the theoretical one ($W_{e_{crit}} = 0.25$), the range of droplet diameter is from $300 < d < 950$. However, as the value of $W_{e_{crit}}$ decreases, the computation reveals that the numerical model presents slight improvement in the prediction of the minimum droplet diameters, at the cost of a large loss of accuracy in predicting the maximum droplet size. Therefore, the influence of the value of the critical Weber number has to be correlated to the coalescence model chosen. This is investigated in the next section of this thesis, for two values of the critical Weber number, $W_{e_{crit}} = 0.05$ and $W_{e_{crit}} = 0.15$.

5.7 Coalescence model effect

It has been established that the choice of the critical Weber number is important for the prediction of the droplet diameters. A calibration is also required on the coalescence model to improve the numerical results. The coalescence probability rate is closely linked to the critical Weber number value, as shown previously in Equation 4.35. A reduction of the critical Weber number value will increase the break-up rate and will decrease the coalescence rate.

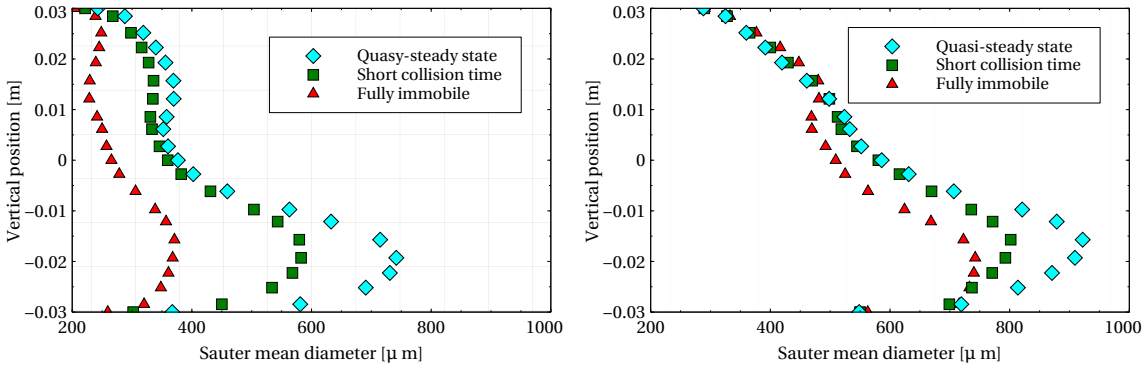

a) $W_{e_{crit}} = 0.05$ b) $W_{e_{crit}} = 0.15$

Figure 5.6: Sauter mean diameter of droplets at the pipe outlet estimation, in function of the drainage time models.

Note that the drainage time of the coalescence model might also influence the coalescence rate. To understand this effect, the drainage time models available in StarCCM+ have been tested for two critical Weber numbers: $W_{e_{crit}} = 0.05$ and $W_{e_{crit}} = 0.15$. Results are shown in Figure 5.6.

Each drainage time model from Table 4.2 produces the same estimates of the minimum droplet size, around $200\mu m$ when $W_{e_{crit}} = 0.05$ and around 300μm when $W_{e_{crit}} = 0.15$. However, the maximum droplet size is better predicted by the quasi-steady state drainage time model with the highest critical Weber value $W_{e_{crit}} = 0.15$. A high $W_{e_{crit}}$ and the quasi-steady state drainage time model are therefore the most adequate choices for this work. To compare further this study with experimental data from Simmons & Azzopardi (2001) and numerical results obtained with Star-CD, a critical Weber number value of 0.23 has been chosen for the validation, as recommended by Lo & Rao (2007).

5.8 Parametric study summary

In this section, a summary of all the models tested, along with their combination is presented. The aim is to give a general overview of all the parametric study performed in the previous sections. Table 5.3 gives the list of the models tested.

TABLE 5.3: List of model tested in the parametric study.

Drag models	Interface force effects	Turbulence models	Droplets generated	We_{crit}	Coalescence model
Schiller	F^D, F^{td}	Realizable 2-layer $k-\varepsilon$	2 drops	0.05	Quasi-steady state
Snyder	F^D, F^{td}, F^{vm}	Turbulence response	3 drops	0.15	Short collision time
Hammard	F^D, F^{td}, F^{ℓ}		4 drops	0.25	Fully immobile
Zhang	$F^D, F^{td}, F\ell, F^{vm}$		5 drops		
Kumar			6 drops		

Table 5.3 shows the final selected models for each columns in red. During this thesis, each of the models have been tested from top to bottom and then left to right. Since the models have been tested independently, the starting point of the simulations were chosen to be the Schiller drag model, F^D, F^{td} for the interface force effects, the Realizable $k-\varepsilon$ turbulence model, 2 drops, a critical Werber number equal to 0.25 and the quasy-steady state coalescence model. From there, each of the model in each column were tested independently. The selected models (those which provide the best results when compared to experimental studies of Simmons & Azzopardi (2001) and given in red in Table 5.3) have then been selected to run the final numerical simulations presented in the next section of this thesis.

Chapter 6

Numerical prediction of droplet size evolution in horizontal pipeline

Based on the thorough study presented in Chapter 5, important parameters necessary to perform accurate PBM simulations have been detailed. All of these findings are put together in this chapter, where numerical results are compared to experimental work. It is shown that, choosing carefully the coalescence and break-up models, using all the interphase source forces, the appropriate drag model and an accurate turbulence model, the numerical results compare well with experimental measurements.

Contents

6.1 Model verification and validation **67**

6.2 Additional numerical investigations **68**

6.1 Model verification and validation

According to the previous observations made in Chapter 5, the numerical model has been calibrated. The momentum transfer term is constituted of the four forces. The drag model of Snyder et al. (2007), implemented within StarCCM+, is used along with the lift model of Auton & Hunt (1988). The drainage time of the coalescence model is set to short collision time (Table 4.2). The number of daughter droplets generated during break-up events is set to 2 and the critical Weber number has been set equal to 0.23. A steady simulation is run for 4000 iterations which permits to reach a pseudo steady state where the average diameter of the droplets remains constant.

It is important to note that the measured values were taken in the middle of the pipe and were averaged over time whereas the computed results shown in Figure 6.1 for both Lo & Rao (2007) and the present computations were obtained for the entire cross section near the pipe outlet. Therefore, the simulated results may be slightly different from experiments. The particle diameter as a function of the cumulative volume fraction near the pipe outlet is given in Figure 6.1. Numerial data and scalar representation of the Sauter mean diameter and the volume fraction are both provided.

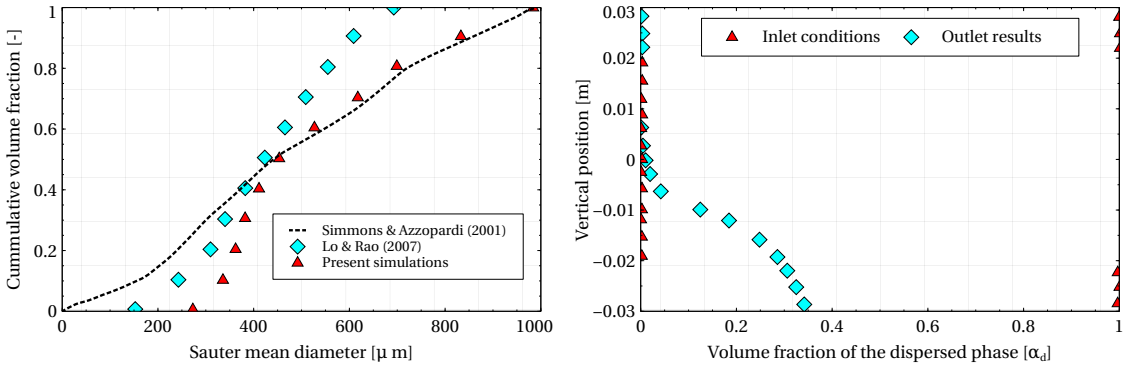

a) Droplet diameter, function of the volume fraction

b) Volume fraction of the dispersed phase

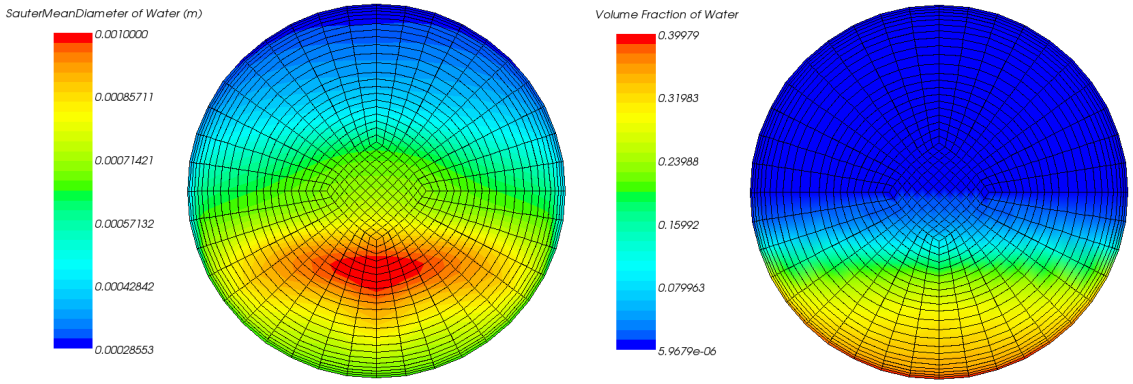

c) Sauter mean diameter at the outlet

d) Volume fraction at the outlet

Figure 6.1: Numerical results.

Results show a good spread of the droplet diameter near the pipe exit. A really good agreement with experimental data from Simmons & Azzopardi (2001) is found for the range of volume fraction $0.5 < \alpha_d < 1$. The coalescence model is well calibrated compared to the numerical simulation of Lo & Rao (2007) where they observed that the large droplets were under-predicted. However, larger discrepancies are observed for the range of volume fraction $0 < \alpha_d < 0.5$. As numerical studies (Lo & Rao, 2007) have shown, the amount of small droplets is over-predicted by the current break-up model. The cause of this under-prediction of the break-up rate and therefore over-prediction of the small droplets has been explained by the authors, by the coarseness of the mesh used in the near wall region. This statement does not seem to be the correct explanation here as the mesh used in the simulations presented in this PhD is very fine next to the wall and an over-estimation of the minimum diameter is still noticeable. The Break-up model probably needs improvement to be able to predict better the minimum size of the droplet in the near wall regions, even if the results remain satisfactory. In addition, different lift models and lift coefficients may lead to satisfactory enhancement of the break-up rate.

The volume fraction of the droplets near the pipe exit shows a settling effect of the droplet towards the bottom of the pipe. Hence, mainly due to turbulent dispersion effects and gravity, the ring distribution designed at the inlet of the pipe is lost as the droplets travel through the pipe length. This leads, eventually, to the formation of a liquid pool in the bottom wall region whereas the kerosene continuous phase, lighter than the dispersed phase, moves in the top region. This settling effect has been observed in both experimental and numerical analysis.

Experimental studies in Simmons & Azzopardi (2001) have been performed for other continuous, disperse phase velocities and different volume fraction of the dispersed phase, however for the same horizontal pipe geometry. Simulations have also been performed for these conditions. Results are discussed in the following section.

6.2 Additional numerical investigations

Tables 6.1 and 6.2 summarize the material properties of both continuous and dispersed phases for the two additional test cases (Cases 2 and 3). Properties for Case 1 discussed in previous chapters are also reported for comparison. The only difference in the kerosene properties between all threes cases is the volume fraction α_c, which is the highest for Case 1 and the lowest for Case 3. For the dispersed phase, the only differences between all three cases is for the velocity u_d and the volume fraction α_d which are the lowest for Case 1 and the highest for Case 3.

These changes into the dispersed phase properties are the only adjustments made to the model. Parameters used and discussed in the previous sections of this report remain identical. The results obtained are displayed in Figure 6.2, near the outlet of the pipe with the same cummulative volume fraction used by Lo & Rao (2007). Simmons & Azzopardi (2001), have shown that the results obtained for the different mixture velocities agreed to fit an ULLN (uper-limit logarithmic normal) curve. This curve is used here for further comparison. The results show that approximately the same minimum and maximum droplet diameters are found for all three different test cases. However, it seems that as the velocity and the volume fraction of the

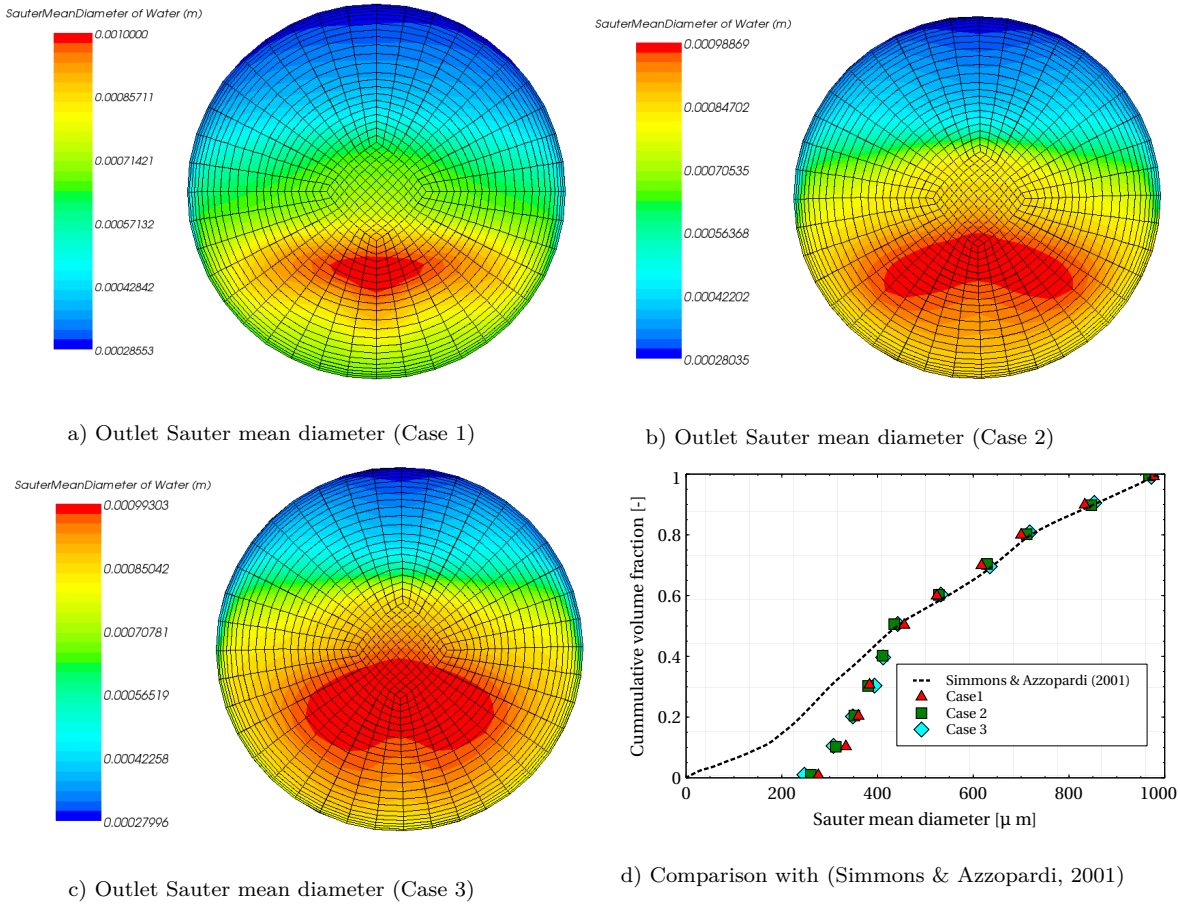

a) Outlet Sauter mean diameter (Case 1)

b) Outlet Sauter mean diameter (Case 2)

c) Outlet Sauter mean diameter (Case 3)

d) Comparison with (Simmons & Azzopardi, 2001)

Figure 6.2: Additional numerical results.

dispersed phase increase, the amount of larger droplets in the entire surface of the pipe exit increases. Unfortunately, no experimental data over the entire cross section of the pipe are available for these study cases. However, from a mathematical point of view, the increase of both dispersed phase initial velocity and volume fraction, lead to the enhancement of the probability collision rate as shown in Equation 4.35. Therefore, it was expected to find an increased amount of large droplets at the surface of the pipe exit as the velocity of the dispersed phase increases.

Table 6.1: Material properties of kerosene for Cases 1-3

Kerosene	Case 1	Case 2	Case 3
ρ_c $[kg/m^3]$	797	797	797
μ_c $[Pa.s]$	0.0018	0.0018	0.0018
u_c $[m.s^{-1}]$	2.393	2.393	2.393
α_c [%]	93.8	88.3	83.1

Table 6.2: Material properties of aqueous potassium for Case 1-3

Aqueous potassium	Case 1	Cases 2	Case 3
ρ_d $[kg/m^3]$	1166	1166	1166
μ_d $[Pa.s]$	0.0016	0.0016	0.0016
u_d $[m.s^{-1}]$	0.158	0.317	0.488
α_d [%]	6.2	11.7	16.9

Chapter 7

Conclusions and discussions

This part described the droplet diameter distribution transported by a continuous kerosene phase in a 4.5 m horizontal pipe. Mean Sauter diameters, forces impact, turbulence specifications of the dispersed phase as well as break-up and coalescence modelling were analysed numerically. Results show reasonable agreement with both numerical and experimental data available in the literature. The following conclusions can be drawn:

1. The forces constituting the momentum transfer term at the interphase are found to play an important role in the computed droplet diameter. Over several drag models, the Snyder et al. (2007) model, implemented in StarCCM+, has been found to provide satisfactory results compared to other models tested. The lift force has been found to enhance break-up rate by pushing droplets towards the wall of the pipe where both shear and turbulence quantities are the strongest. The turbulence dispersion force plays a considerable part in the overall motion of the droplets by pushing them from high to low concentration regions. The virtual mass force is less important than the other forces contribution in this study, due to the low values of both phases accelerations.

2. The turbulence modelling of the dispersed phase is extremely important for an accurate computation of the break-up and coalescence events. The realizable 2-layer k-ε and the turbulence response model have been tested. The turbulence response model seems more appropriate to accurately predict droplet sizes.

3. Break-up and coalescence models available in the numerical solver were investigated. The specification of the number of droplet generated during break-up events has been found to have a negligible impact on the average mean sauter diameter of the droplet. However, the specification of both critical Weber number and coalescence drainage time models play an important role for minimum and maximum droplet diameter predictions.

4. The present study shows good agreement with experimental data for the particle diameter prediction for cumulative volume fraction in the range $0.5 > d > 1$. Larger discrepancies are observed in the range $0 < d < 0.5$, also obtained in the numerical simulation of Lo & Rao (2007) with Star-CD. Therefore, the break-up rate seems to be under-predicted by the current model. Break-up

model may need further enhancement, in particular for the critical diameter specification along with the break-up rate model. The contribution of the lift force has also been found to be extremely important for the minimum droplet size. Therefore, the addition of a lift model may improve the results.

5. Additional studies have been carried out for different dispersed phase superficial velocities. The results have shown that an increase of the dispersed phase velocity tends to enhance the probability of collision rate and therefore increase the amount of large droplets observed in the entire outlet cross section of the pipe.

Even if this part provides a good understanding of the phenomenon responsible for both break-up and coalescence events and a reasonable agreement with experimental data has been obtained, additional experimental data over different sections of the pipe would provide better understanding of the physical phenomena.

The models derived and presented in this part have shown to provide satisfactory results for droplet size prediction in horizontal pipelines. As detailed previously, the coalescence model is relatively easy to implement in a CFD code since no integral resolution is required. The implementation of the break-up model may, however, be more problematic. This will be discussed in the Part IV of this thesis as the present model is implemented in OpenFOAM. It has been shown that the contribution of each force at the interphase is necessary, along with good modelling of the turbulence quantities and an appropriate drag model. Based on the findings of this part, an accurate population balance model, using a standard method of moment, will be detailed in Part IV.

Part of the work presented here has been published in Bourdillon et al. (2016) and additional work is ongoing based of these findings. In particular, a comparison, in terms of accuracy and speed, is performed with similar settings and same study case between three different population balance models: Method of classes, Standard method of moment (present work) and quadrature method of moments.

Nomenclature

Dimensionless numbers

A_H	Hamaker constant	$[-]$
C_a	Capillary number	$[-]$
E_o	Eötvös number	$[-]$
W_e	Weber number	$[-]$
P_r	Prandtl number	$[-]$
R_e	Reynolds number	$[-]$
y^+	Non-dimensional wall distance	$[-]$

Greek letters

α	Volume fraction	$[-]$
χ	Shear rate	$[s^{-1}]$
Δt	Time step	$[s]$
η	Log-normal distribution	$[-]$
γ	Moment	$[-]$
μ	Dynamic viscosity	$[kg.m^{-1}.s^{-1}]$
ν	Kinematic viscosity	$[m^2.s^{-1}]$
Φ	Phase difference	$[-]$
ρ	Density	$[kg.m^{-3}]$
σ	Surface tension	$[kg.s^{-2}]$
$\tau(d)$	Time scale	$[s]$
ε	Turbulent energy dissipation rate	$[m^2.s^{-3}]$
ξ	Internal properties	$[-]$
ζ	Free-stream fraction	$[-]$

Operators

$:$	Scalar product of two tensors	$[-]$
$\cdot$	Scalar product of two vectors	$[-]$
Δ	Laplacian operator	$[-]$
$\|a\|$	Modulus of a	$[-]$
$\mathbf{a}$	Vector of a	$[-]$

$\nabla\cdot$	Divergence operator	$[-]$
$\nabla\times$	Curl operator	$[-]$
∇	Gradient operator	$[-]$
$\overline{a}$	Mean of a	$[-]$

Roman letters

$\dot{m}$	Mean	$[-]$
$\dot{w}$	Width	$[-]$
ℓ_ε	Length scale	$[m]$
ℓ_l	Lower limit	$[-]$
A	Area	$[m^2]$
a	Acceleration component	$[m.s^2]$
$d_{3,0}$	Three-zero diameter	$[m]$
$d_{3,2}$	Sauter mean diameter	$[m]$
d	Diameter	$[m]$
E	Production terms	$[-]$
F	Forces	$[kg.m.s^{-2}]$
f	Film	$[-]$
G	Rate change of particle properties	$[s^{-1}, kg^{-1}, m^{-1}]$
g	Gravitational acceleration value	$[m.s^{-2}]$
h	Discrete events	$[-]$
I	Intensity	$[\%]$
K	Rate	$[s^{-1}, kg^{-1}, m^{-1}]$
k	Turbulent kinetic energy	$[m^2.s^{-2}]$
L	Length	$[m]$
L_K	Kolmogorov length scale	$[m]$
M	Interphase momentum transfer	$[-]$
N	Total number density	$[-]$
n	Number density function	$[-]$
$N(d)$	Child produced during break-up	$[-]$
P	Probability density function	$[-]$
p	Pressure	$[Pa]$
R	Modulus of mean strain rate tensor	$[s^{-1}]$
r	Radius	$[m]$
S	Source term	$[-]$
t	Time	$[s]$
u	Velocity components	$[m.s^{-1}]$
u_l	Upper limit	$[-]$
W	Rotation rate tensor	$[s^{-1}]$
x	External properties	$[-]$
y	Wall distance	$[m]$

Subscripts

∞	Single-particle	[−]
b	Buoyancy	[−]
br	Break-up	[−]
c	Continuous phase	[−]
$coall$	Coalescence	[−]
$coll$	Collision	[−]
$crit$	Critical value	[−]
d	Dispersed phase	[−]
$drain$	Drainage	[−]
eq	Equivalent value	[−]
Hy	Hydraulic	[−]
i, j, l	Phases i, j or l	[−]
if	Interfacial	[−]
in	Inertial	[−]
k	Kinetic energy contribution	[−]
m	Mixture	[−]
max	Maximum value	[−]
min	Minimum value	[−]
p	Particle	[−]
r	Relative components	[−]
vi	Viscous	[−]

Superscripts

$'$	Fluctuating part	[−]
ℓ	Lift	[−]
$Birth$	Birth of droplet	[−]
D	Drag	[−]
$Death$	Death of droplet	[−]
int	Internal	[−]
$mass$	Mass	[−]
mom	Moment	[−]
T	Transpose	[−]
t	Turbulent	[−]
td	Turbulent dispersion	[−]
th	Thickness	$[m]$
vm	Virtual mass	[−]

Part III

Solidification phenomenon modelling

8 Review of solidification phenomenon modelling 77

9 Introduction to solidification processes and modelling 78
9.1 Solidification process . . . 79
9.2 Mathematical models for solidification . . . 81
9.3 Treatment of the partially solidified region . . . 84

10 Natural convection process 87
10.1 Natural convection model . . . 88
10.2 Numerical simulations of natural convection in cavities . . . 90

11 Solidification process with mushy region modelling 98
11.1 Solidification model with mushy region (IF) . . . 99
11.2 Numerical simulations of water freezing in cavities . . . 102
11.3 Numerical simulations of water freezing in cylinders . . . 110

12 Solidification process with slurry-mushy regions modelling 116
12.1 Solidification model with slurry-Mushy regions (IFSM) . . . 117
12.2 Numerical simulations of water freezing in cavities . . . 121
12.3 Numerical simulations of water freezing in cylinders . . . 124

13 Conclusions and discussions 128

Nomenclature 131

Chapter 8

Review of solidification phenomenon modelling

This part presents theoretical and numerical aspects of solidification modelling. The work of previous researchers, identified through a literature review presented in Chapter 9, has been used to design solvers for single-fluid freezing simulations. Basic aspects of phase changes, numerical methods and models currently used to tackle solidification problems with CFD and theoretical concepts of the modelling of partially solidified regions are presented. This chapter also identifies promising recent findings which are used collectively in this work to create new solidification models. The strategic position regarding the choice of models used in this PhD is finally provided. Based on the findings detailed in this chapter, a natural convection solver has been designed in OpenFOAM. Chapter 10 details the mathematical formulation of the model implemented and its validation against numerical results from the literature for heat transfer phenomena of water inside cavities. Results agree well, the maximum local discrepancies being evaluated below 15 %. Steady-state solutions from this solver are used as initial conditions for solidification simulations. The first solidification model approaches the partially solidified region as a mushy region, assumed to behave as a porous media. Chapter 11 contains the derivation of this solver and water freezing processes inside cavities and cylinders and are validated against both numerical and experimental results. Simulated results agree well with other simulated and experimental results, the maximal local discrepancies being close to 15 % for the later case, where experimental measurement were provided. This solidification solver has finally been extended and modified to create a novel formulation to account for both slurry and mushy regions. In this case, a distinction is made between the newly formed iced particles not interacting with each other (slurry region) and the mixture of compact ice and liquid (mushy region). The numerical model of this solver is detailed in Chapter 12. A validation is also performed, based on the test cases used in Chapter 11. Finally, this chapter presents a discussion which identifies and explains the discrepancies between the two models derived in this Part. It appears clearly that physical phenomena observed in experiments could be reproduced with high accuracy when using either models. This is thoroughly discussed in Chapter 13 where conclusions, and useful findings to be used in the next part of this thesis (Part IV) are provided.

Chapter 9

Introduction to solidification processes and modelling

A literature review is presented in this chapter. Basic theoretical concepts of solidification are presented and the principles of thermodynamics are explained. The nomenclature related to this entire part (i.e. Part III) is presented along with a description of each term. Current CFD models for freezing studies are also reviewed. It is found that an enthalpy-porosity model constitutes a promising solution to tackle solidification related problems. Freezing simulations are often time demanding as fine time steps and mesh resolution are usually necessary (in an Eulerian framework) to capture every features of the flow. An error function has therefore been used to compute fast phase change processes. The treatment of the partially solidified region is then emphasized and it is found that the use of Darcy's law along with additional viscosity in the flow can be used to simulate both mushy and slurry regions with accuracy.

Contents

9.1 Solidification process **79**
9.2 Mathematical models for solidification **81**
9.3 Treatment of the partially solidified region **84**

9.1 Solidification process

Solidification or freezing refers to the change of state from liquid to solid in a thermodynamic system. The change of state from one phase to another, usually due to a temperature or pressure gradient, induces significant changes in material properties (viscosity, velocity, volume...). Typically, for a given set of critical pressures and temperatures one can observe transition between solid, liquid and gaseous states. Figure 9.1, from Marechal (2008), describes the phase transition nomenclature and a typical phase diagram for phase transition processes in function of pressure and temperature evolutions. The critical pressure and temperature points passed which a phase change will occur, depend on the nature of the phases. As an example, for a liquid flowing inside a domain at a temperature below a critical temperature, phase change from liquid to solid will appear. In that specific case, this critical temperature is referred to as the solidus temperature.

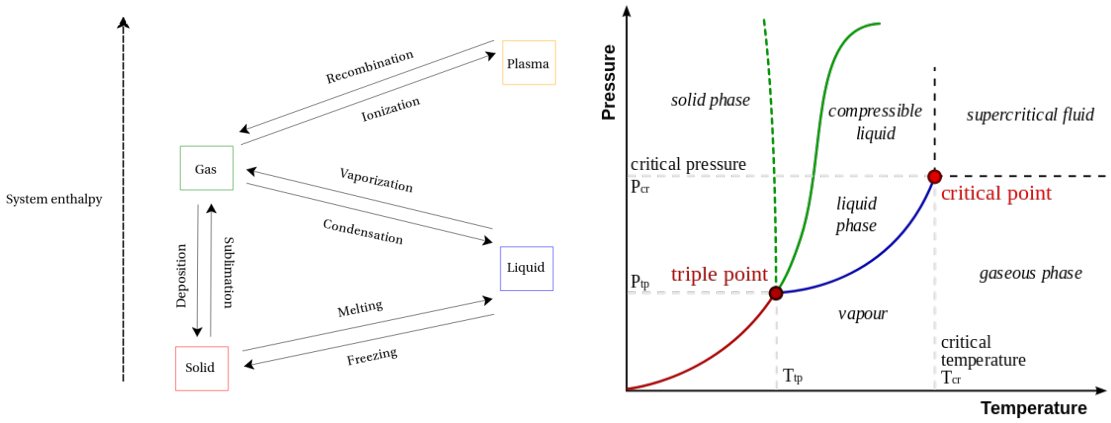

FIGURE 9.1: Phase change nomenclature (left) and phase diagram (right).

Solidification, or freezing phenomena, are complex events involving heat transfers during phase changes. In order to quantify and approach this process of heat transfer, the latent heat is often used. The latent heat L is the heat released or absorbed by a thermodynamic system during a change of matter state (Perrot, 1998) for a constant temperature. The change of matter state from liquid to solid is an exothermic process which means that the amount of latent heat stored during the motion of the flow and other phase transitions is released as sensible heat during freezing events. On the contrary, the change of phase from solid to liquid is an endothermic process since the system absorbs energy during melting events. The distinction between latent and sensible heat may be difficult since they refer to the same form of energy. However, latent heat is directly associated with phase change process whereas sensible heat quantifies the influence that a transfer of energy has on the temperature of the system. The latent heat of fusion refers to the heat released or absorbed during freezing or melting events. Values for several substances (water, oxygen, hydrogen...) are available in the literature. The specific latent heat L_{qs} is then used to quantify the amount of heat Q needed to achieve the change of state of a material per unit of mass m. The sensible heat Q_s represents the product

between the mass of the substance m, the specific heat capacity c and the gradient of temperature ΔT.

An important parameter related to a phase change process is the heat capacity C. It represents the amount of heat required to modify the temperature of a system by a given amount. The heat capacity value is problem dependent since it is an extensive property of the matter, meaning that the size of the problem directly influences its evolution. For ease of use, the heat capacity is often expressed as an intensive property by the so called specific heat capacity c. The heat capacity is defined according to fundamentals principles of thermodynamics. The internal energy E of a system can be modified by two factors, the work done by this system W and the amount of heat Q received.

TABLE 9.1: Mathematical expression of solidification terms.

Terms	Formulation	Nomenclature
Specific latent heat	$L_{qs} = \frac{Q}{m}$	Q : heat released/absorbed kJ
		m : mass of the substance kg
Sensible heat	$Q_s = mc\Delta T$	c : specific heat capacity $J/kg.K$
		ΔT : gradient of temperature K
Heat capacity	$C = \frac{\Delta Q}{\Delta T}$	ΔQ : gradient of heat kJ
		ΔT : gradient of temperature K
Heat capacity ($p = cst$)	$C_p = \left(\frac{\partial H}{\partial T}\right)_p = \left(\frac{\partial Q}{\partial T}\right)_p$	$J.K^{-1}$
Heat capacity ($V = cst$)	$C_V = \left(\frac{\partial U}{\partial T}\right)_V = \left(\frac{\partial Q}{\partial T}\right)_V$	$J.K^{-1}$
Specific heat capacity	$c = \frac{\partial C}{\partial m}$	$J.kg^{-1}.K^{-1}$
Specific heat capacity ($p = cst$)	$c_p = \left(\frac{\partial C}{\partial m}\right)_p$	$J.kg^{-1}.K^{-1}$
Specific heat capacity ($V = cst$)	$c_V = \left(\frac{\partial C}{\partial m}\right)_V$	$J.kg^{-1}.K^{-1}$
Enthalpy	$H = h + \Delta H$	h : specific sensible enthalpy J
		ΔH : gradient of enthalpy
Specific sensible enthalpy	$h = h_{ref} + \int_{T_{ref}}^{T} cdT$	h_{ref} : Reference enthalpy J

The mathematical formulation of this relation is given in Equation 9.1.

$$dE = \delta Q + \delta W = \delta Q - pdV \ , \tag{9.1}$$

which leads to the expression of the heat capacity if the heat is added to the domain at a constant volume (see Equation 9.2).

$$C_V = \left(\frac{\partial E}{\partial T}\right)_V = \left(\frac{\partial Q}{\partial T}\right)_V \ . \tag{9.2}$$

Additionally, the mathematical expression of the enthalpy H of a thermodynamic

system is given by Equation 9.3.

$$\begin{aligned} H &= E + pV \ , \\ dH &= \delta Q + V dp \ . \end{aligned} \tag{9.3}$$

This expression allows to obtain the formulation of the heat capacity at a constant pressure in Equation 9.4:

$$C_p = \left(\frac{\partial H}{\partial T}\right)_p = \left(\frac{\partial Q}{\partial T}\right)_p . \tag{9.4}$$

The total energy of a thermodynamic system is expressed in terms of enthalpy of the system H which is computed as a function of the internal energy, pressure and volume of a system. However, for specific solidification problems, the enthalpy is often expressed as the sum of the specific sensible enthalpy h and the gradient of enthalpy ΔH which is related to the latent heat of fusion. Direct resolution of the total enthalpy H is impossible. Therefore, the evolution of the enthalpy in the domain ΔH is more of scientific interest. In case of freezing, since the process is exothermic, the sign of the enthalpy changes : ΔH is negative, due to the amount of energy released during the phase change process. Table 9.1 provides the mathematical formulation of the terms explained previously.

9.2 Mathematical models for solidification

Solidification refers to the phase transition between liquid and solid states when the liquid part of the fluid is cooled down at a temperature below its freezing point. Conversely, the change of state from solid to liquid, called the melting process, occurs when the solid part of the fluid is heated to temperatures above the melting point. For pure substances (pure water for instance), melting and freezing points are found for the same temperatures. Solidification phenomena are commonly encountered in the foundry industry, food conservation and oil engineering for instance (Kowaleski & Rebow, 1999). Solidification problems give rise to many important issues such as pressure drops, diminution of flow rate or even flow blockage due to ice accretion which can cause breakage of the pipeline (Weigand & Beer, 1993). Pressure drop in pipes is defined as the pressure difference between two control volumes within it. Magnitude of frictional forces, caused by resistance to the flow (velocity, viscosity) directly influences the magnitude of the pressure drop. Usually solidification starts near the wall layer of the pipe due to a wall temperature below the freezing point of the fluid and spreads towards the center of the pipe. Therefore, it can diminish the flow rate and by consequence the amount of oil expected to be pumped through the pipeline. Once formed, ice can agglomerate against the pipe wall towards the center of the pipe, leading to potential blockage and breakage of the pipe. Mass, momentum and energy properties are highly dependent on the phase state (solid or liquid) (Hu & Argyropoulos, 1996). Usually, the separation between solid and liquid states takes the form of a thin layer whose position cannot be specifically determined in advance. These problems of moving boundary are also

referred to as Stefan problems (Stefan, 1889b) (Stefan, 1889a). Stefan proposed an exact analytical solution for moving boundary problems applicable to a single phase. Later on, Neumann (1912) improved the analytical resolution of the Stefan problem by extending it to two phase problems, however only in rectangular coordinates. Paterson (1952) extended this work further for cylindrical coordinates. However, these types of exact analytical solutions are only applicable for constant parameters fields in both phases. They are still used for some particular fields such as aircraft icing where exact analytical solutions are possible (Myers & Mitchell, 2011). The numerical modelling of solidification processes remains a challenging field of study for engineers and researchers. Prescribing the moving solid-liquid interface and dealing with variable fluid properties induced by thermal evolution, constitute the main difficulties of this research area. Then, Goodman (1958) introduced the heat balance integral method where integrals are used to express the overall heat balance in entire domains. This method is, however, only applicable for extremely simple cases due to the mathematical complexity of its resolution. With the development of numerical methods able to handle moving boundary problems, two methods have emerged over the years, the fixed and variable grid methods. The fixed grid methods are used to compute temperatures for a given time at a given position on a fixed grid. Consecutive values of temperatures are computed by finite differences between two points and two time steps. Therefore, the moving boundary position will be approximated between two fixed nodes of the grid. Using a fixed grid method allows to approximate the moving boundary relatively easily. However, computational time can become highly demanding for large domains or extended time (Basu & Date (1988); Voller et al. (1990)). The variable grid methods allow to overcome this limitation by solving the exact position of the moving boundary for every single time step of the simulation. A finite difference scheme is applied at each time step, through a moving grid to obtain the exact position of the moving boundary. Even though these methods have been applied widely (Murray & Landis (1959); Tien & Churchill (1965); Heitz & Westwater (1970)), they are only applicable for one-dimensional problems. To investigate more complex multi-dimensional problems, more representative of the physics, one has to use methods where the location of the moving boundary is not explicitly tracked. Several approaches have emerged over the past few years, a brief description of each one of them is provided below.

- Apparent heat capacity method: The apparent heat capacity method has been introduced by the work of Hashemi & Sliepcevich (1967). It computes the evolution of the heat capacity of a material as a function of the temperature. Therefore, if, for a given computational cell, the temperature successively falls below the solidus point and rises above the liquidus point during the same time step, the heat capacity changes cannot be computed. To overcome the problem, one can use very small time steps but this leads obviously to an important loss of computational time efficiency.

- Effective capacity method: The effective capacity method, proposed by Poirier & Salcudean (1988), is an alternative to the apparent heat capacity method. Rather than computing an apparent heat capacity in each cell, an effective

heat capacity is integrated by a temperature profile between nodes of the cells constituting the computational domain. Even if the method allows to overcome the limitations of the apparent heat capacity method, its implementation and integration can be extremely complex (Poirier (1986); Hu & Argyropoulos (1996)).

- Heat integration method: In the heat integration method, the temperature is evaluated in each computational cell. If the calculated temperature is below the solidus temperature, phase change from liquid to solid state occurs in the cell studied. The method has been successfully applied in several studies (Dusinberre (1945); Argyropoulos (1981); Rolph & Bathe (1982)). However, even if some limitations observed with both apparent and effective capacity methods are overcome by this model, the prediction of the position of the moving boundary is sometimes inaccurate and the momentum equation is not solved for the liquid phase (Poirier & Salcudean, 1988).

- Source-based method: This method introduces any additional heat (caused by either freezing or melting) into the transport energy equation as source terms (Voller & Swaminathan, 1991). Such method has been widely used due to its relative ease of implementation (Salcudean & Abdullah (1988); Voller et al. (1990)). However, if the overall accuracy and computational time are acceptable, the correct prediction of the moving boundary location may be difficult (Hu & Argyropoulos, 1996).

- Enthalpy method: The Enthalpy method is used to solve common conservation equations on a fixed Eulerian computational grid. It uses source terms as in source-based methods to take into account evolving physical properties during the phase change. Usually, the effect of phase change is recorded through the latent heat of fusion in function of the temperature. Currently the enthalpy method is widely used to handle solidification/melting problems (Rose (1960); Bell & Wood (1983); Tacke (1985); Voller et al. (1990); Lacroix (1993); Gong & Mujumdar (1997); Trp (2005)). Even if it could be difficult to implement, the enthalpy method is one of the most promising method to tackle solidification/melting problems.

- Enthalpy-porosity method: The enthalpy-porosity method is an alternative to the enthalpy method and has been recently successfully used (Conde et al. (2004); Jalali & Najafi (2010); Rosler & Bruggermann (2011); ANSYS (2011); StarCCM+ (2012)). In this method, the evolution of the latent heat in function of the temperature is not necessary a linear function as opposed to the enthalpy method. These problems are also refereed to as mushy solidification problems. This approach, first proposed by Voller & Prakash (1987) permits to handle solidification problems where phase change occurs for a range of temperature instead of a constant temperature ($T_{sol} \neq T_{liq}$), which is the case for non-pure materials. The relation between the latent heat and the temperature is performed through the volume fraction of the material studied. Depending on the values taken by the volume fraction, the fluid can be considered as pure liquid ($\alpha_\ell = 1$), pure solid ($\alpha_\ell = 0$) or neither pure liquid or

solid ($0 < \alpha_\ell < 1$). In this last case scenario, a mushy region is introduced which is treated as a porous medium. The mushy region is considered to be a solid material containing pores and holes filled by the liquid material.

As discussed previously, several researchers have focused on moving grid techniques for the treatment of the liquid-solid front (Wintruff & Gunther (2001); Jana et al. (2007)). However, the use of a deforming mesh can often become complex and therefore considerable efforts have been made over the past few years to track the solid/liquid moving boundary on a fixed Eulerian grid. Many numerical models used to tackle solidification problems are described in detail in Hu & Argyropoulos (1996). Among available models, the enthalpy based models have been widely investigated (Rose (1960); Bell & Wood (1983); Tacke (1985); Voller et al. (1990); Lacroix (1993); Gong & Mujumdar (1997); (Trp, 2005)). A particular attention on modelling the sink of velocity from liquid to solid phases is, however, required when using fixed grid methods. To numerically represent the phenomenon, common procedures consist in adding viscosity to the flow in the solid zone (Gartling, 1980) or reducing the velocity into the momentum equations directly by adding sink terms. The next section presents an overview on procedures to handle the partially solidified region.

9.3 Treatment of the partially solidified region

The enthalpy-porosity method treats the liquid volume fraction as a function of temperature. Therefore, one can usually distinguish three distinct regions depending on the temperature considered. The liquidus temperature (T_{liq}) is the upper bound past which a fluid will evolve in a liquid state and therefore past which $\alpha_\ell = 1$. On the contrary, any fluid in regions where the temperature is below the solidus temperature (T_{sol}) is assumed to be in solid state and thus $\alpha_\ell = 0$. Finally, the transition between fully liquid or fully solid state is computed through a function, usually defined as shown in Equation 9.5:

$$\alpha_\ell = \frac{T - T_{sol}}{T_{liq} - T_{sol}} \text{ for } T_{sol} < T < T_{liq}. \tag{9.5}$$

This region, where $0 < \alpha_\ell < 1$ is called the partially solidified region. The partially solidified region can be split in two regions. The slurry and the mushy zones. Depending on the value of the solid volume fraction ($f_s = 1 - \alpha_\ell$) the fluid will be considered in the slurry or the mushy region. Therefore, for a solid volume fraction such as $f_s < 0.3$ the mixture is considered as a slurry, the solid grains are suspended in the flow and do not interact with each other. However, for higher values of the solid volume fraction ($f_s > 0.3$) the solid grains are assumed to agglomerate in the mushy region. Since the size and shape of the crystals are different in these two regions, the resistance to the flow is not identical in both regions. Resistance to the flow field induced by the change of state of the fluid is modelled through slurry-viscosity models in the slurry region and is assimilated to a porous medium in the mushy region. Since the enthalpy-porosity approach only models the effect

of phase change in the energy equation, additional source terms are required in the momentum equation to accurately model the sink of velocity in the fully solid region. The enthalpy- porosity model, initially proposed by Voller & Prakash (1987), treats the partially solidified region as only a mushy region. The sink of velocity in solid regions during a phase change can be modelled by Darcy type source terms (Darcy, 1856) which has been widely used to describe the flow of fluids through porous medium. If the porosity decreases, the same effect is observed in the permeability and the velocity. Therefore, the porosity function acts as a trigger to simulate the effect of phase changes into the fluid properties.

Where $f_s < 0.3$ the partially solidified region can be treated as a slurry region. The slurry region is treated through slurry-viscosity models. Several models exist to simulate the effect of suspended grains into the flow field. Slurry-viscosity models aim at increasing the viscosity of the mixture in order to model the effect of the solidified particles, not interacting with each other, on the motion of the fluid. The viscosity of the liquid phase is modified according to different parameters depending on the model chosen. Table 9.2 summarizes the expression of the relative viscosity for the most common slurry-viscosity models.

Table 9.2: Slurry-viscosity models.

Models	Formulation
(Liu, 2000)	$\mu^* = \left[a\left(f_{s_{max}} - f_s\right)\right]^{-n}$
(Mooney, 1951)	$\mu^* = \exp\left(\frac{\mu f_s}{1-K f_s}\right)$
(Krieger & Dougherty, 1959)	$\mu^* = \left(1 - \frac{f_s}{f_{s_{max}}}\right)^{-\mu f_{s_{max}}}$
(Chong et al., 1971)	$\mu^* = \left(1 + \frac{0.75 f_s / f_{s_{max}}}{1 - f_s / f_{s_{max}}}\right)^2$
(Dabak & Yucel, 1986)	$\mu^* = \left[1 + \frac{\mu f_{s_{max}} f_s}{n(f_{s_{max}} - f_s)}\right]^n$
(Metzner, 1985)	$\mu^* = \mu\left[1 - \frac{F_k f_s}{A_{crys}}\right]^{-2}$

Few studies dealing with these slurry-viscosity models are available in the literature. Among them, Pradipta et al. (2008) stated that, for a limestone-water slurry mixture, Liu (2000) model predicted the relative viscosity better compared to Mooney (1951), Krieger & Dougherty (1959), Chong et al. (1971), Dabak & Yucel (1986). It is shown that most of these models use a maximum solid fraction ($f_{s_{max}}$) which is obtained by extrapolating a fitting line from experimental data. Therefore it is entirely case dependent and could not be applicable for a wide range of flow. Moreover, some (Dabak & Yucel (1986); Liu (2000)) are build from a predicted relative viscosity (n) which can also be difficult to interpret. In the presented models, Metzner (1985) remains the easiest to implement in a CFD code since it does not suffer from the same constraints. As a result, this model will be used and validated when dealing with slurry regions modelling.

Based on the previous statements, the model to be implemented in this PhD work will be based on an enthalpy-porosity method (which permits to expand the range of applicability of the enthalpy based method) described in Voller & Prakash (1987)

using Darcy's law to represent the effect of partially solidified fluid in the mushy region. This will be coupled with a slurry-viscosity approach to model additional viscosity of the flow, induced by solid grains not interacting with each others, in the slurry region. Variable properties for water will also be used along with additional novel techniques that will be described in the next chapter of this PhD thesis.

Chapter 10

Natural convection process

A Convection solver has been implemented in the Open source CFD code OpenFOAM to study heat transfer phenomena of water in internal geometries. A polynomial water density variation has been used for the gravity related terms. Temperature-dependent fluid properties, mass, momentum and energy conservation equations are derived. The present model is validated with numerical results from the literature for natural convection of water in cavities. Good qualitative agreement is also found when compared to experimental measurements. A comparison with the standard Boussinesq approximation is finally performed. This study identifies that the use of variable properties is an essential feature for the correct modelling of natural convection of water. In particular, a small change in density (of the order of 0.2 $kg.m^{-3}$) induces significant changes in flow patterns. This finding can be applied to other engineering fluids of interests, such as kerosene, air or brine for example and therefore improve the accuracy of the modelling of freezing processes. This convection solver solution can be used as a boundary condition, before solidification phenomena are considered, so that computational time is reduced.

Contents

10.1 Natural convection model **88**
10.1.1 Temperature-dependent parameters 88
10.1.2 Momentum and energy conservation equations 88
10.2 Numerical simulations of natural convection in cavities **90**
10.2.1 Numerical campaign 90
10.2.2 Grid independence study 90
10.2.3 Model verification and simulations results 93
10.2.4 Comparison with the standard Boussinesq approximation 95
10.2.5 Comparison with Experimental measurements 96

10.1 Natural convection model

In natural convection, the fluid motion is only generated by the density difference in the fluid. This density difference is caused by temperature gradients and produces the driving force responsible for flow appearance, the buoyancy force. The fluid in contact or near a hot heat source is warmed up and becomes less dense. As a result this fluid rises inside the domain. On the other hand the fluid near the cold heat source is pushed and moves to replace the hot fluid in its previous position, in the vicinity of the hot heat source. Since this heat source still warms up the domain, the cold fluid becomes heated and its density decreases. This repeated physical phenomenon in a closed domain generates the motion of the fluid in natural convection, this motion being referred to as the convection current.

10.1.1 Temperature-dependent parameters

The solver implemented in OpenFOAM is called ConvectionFoam (CF). It is a transient, laminar solver for natural convection problems. The solver does not simulate phase change processes. However, it has been designed to reach steady state solutions. Fields of interest (temperature, velocity, pressure...) in steady state, can then serve as initial parameters for the switching to solidification solvers. Heat transfer induced by convection refers to the process of exchanging heat between two or more regions due to the motion of the fluid. Usually, this phenomenon is induced by a temperature gradient causing a density difference between regions. Following published work from Kohlrausch (1968) and Kowaleski & Rebow (1999), a fourth order polynomial formulation (Figure 10.1) can be written for the gravity related terms in the momentum equations, to model the water density variation:

$$\begin{aligned}\rho(T) = {} & 999.840281167108 + 0.0673268037314653 \times T \\ & - 0.00894484552601798 \times T^2 \\ & + 8.78462866500416.10^{-5} \times T^3 \\ & - 6.62139792627547.10^{-7} \times T^4\end{aligned} \tag{10.1}$$

10.1.2 Momentum and energy conservation equations

Momentum equations for the 2D convection solver are computed as follows:

$$\begin{aligned}&\frac{\partial u}{\partial x} + \frac{\partial v}{\partial y} = 0 \ , \\ &\frac{\partial \rho_r u}{\partial t} + u\frac{\partial \rho_r u}{\partial x} + v\frac{\partial \rho_r u}{\partial y} = -\frac{\partial p}{\partial x} + \mu\Delta u \ , \\ &\frac{\partial \rho_r v}{\partial t} + u\frac{\partial \rho_r v}{\partial x} + v\frac{\partial \rho_r v}{\partial y} = -\frac{\partial p}{\partial y} + \mu\Delta v - g[\rho(T) - \rho_r] \ ,\end{aligned} \tag{10.2}$$

where ρ_r stands for the water density at reference temperature, p is the pressure and μ represents the dynamic viscosity of water. The PISO algorithm (Oliveira

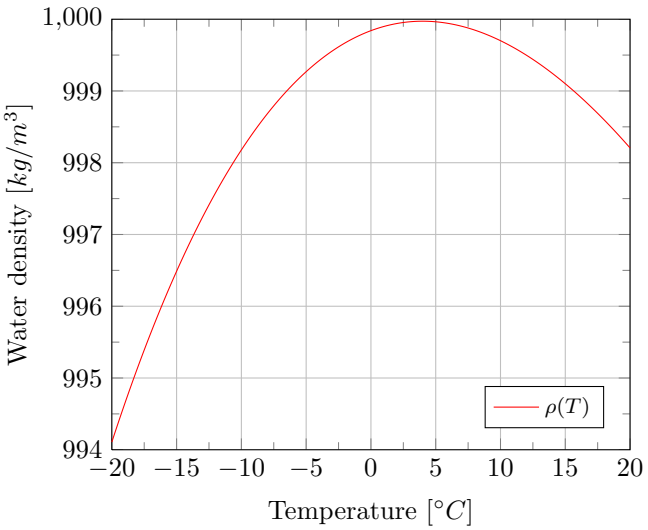

Figure 10.1: Water density variation function of the temperature between $-20\ °C$ and $20\ °C$

& Issa, 2001) is used to ensure the pressure-velocity correction-coupling during the simulation. The gravity related terms in Equation 10.2 (i.e. $-g[\rho(T)-\rho_r]$) represents the modified Boussinesq approximation (Boussinesq, 1897). This assumption is valid as the density variations meet the requirement shown in Equation 10.3.

$$\frac{\Delta\rho}{\rho_r} << 1. \tag{10.3}$$

Once flux and velocity fields are obtained from Equation 10.2, the temperature equation representing the convection phenomenon is solved:

$$\frac{\partial T}{\partial t} + u\frac{\partial T}{\partial x} + v\frac{\partial T}{\partial y} = \gamma\Delta T\ . \tag{10.4}$$

The thermal diffusivity term γ determines the ability of a material to conduct or store energy:

$$\gamma = \frac{\lambda}{\rho_r c_p}\ , \tag{10.5}$$

with λ the thermal conductivity, i.e. the ability of a material to conduct heat and c_p the specific heat capacity, which is the heat required to change the temperature of a material. The natural convection solver implemented in OpenFOAM is able to handle 2D laminar and single fluid problems of heat transfer.

10.2 Numerical simulations of natural convection in cavities

10.2.1 Numerical campaign

The test case presented in this section stands as a numerical benchmark for water freezing studies. Numerical simulations have been performed with the commercial CFD code Fluent (ANSYS, 2011) and with the in-house code frecon in Kowaleski & Rebow (1999). Simulation results obtained with the convection solver implemented in OpenFOAM are compared to these results. Additionally, the same numerical simulations have been run with StarCCM+ (2012) for further comparisons. For the sake of clarity results from this last software will not be provided here but good agreement has been obtained with Kowaleski & Rebow (1999). The natural convection phenomenon of water, induced by a temperature gradient between two opposite walls, is analyzed in a squared shape cavity of height $\ell = 38\ mm$. Upper and lower walls are assumed adiabatic and a temperature gradient is induced from the left wall ($T_{w_\ell} = 283\ K$) to the right wall ($T_{w_r} = 273\ K$). The natural convection solver is used to reach a pseudo-steady state solution. Once the solution has converged, the fields of interest (i.e. velocity, pressure and temperature) are extrapolated and used as initial conditions to study water freezing processes. This will be discussed in the next section of this thesis. For this study, the internal temperature is initialized to $T_i = 278\ K$. No initial velocity is assumed. Table 10.1 summarises the water properties from Kowaleski & Rebow (1999) for the test case.

TABLE 10.1: Water properties for the natural convection study

Water properties	Symbol	Values	Units
Density	ρ_r	999.8	$kg.m^{-3}$
Dynamic viscosity	μ	0.001003	$kg.m^{-1}.s^{-1}$
Thermal conductivity	λ	0.6	$W.m^{-1}.K^{-1}$
Heat capacity	c_p	4182	$J.kg^{-1}.K^{-1}$
Gravitational acceleration	g	9.81	$m.s^{-2}$
Thermal diffusivity	γ	1.435×10^{-7}	$m^2.s^{-1}$

As the Prandtl number is close to $P_r \simeq 7$ and the Rayleigh number to $R_a \simeq 2\ 518\ 084$, the heat transfer is assumed to be convective. The flow is laminar since the Reynolds number, computed from the maximal velocity value, is close to 40. Numerical simulations are carried out for approximately 33 minutes to reach the steady state.

10.2.2 Grid independence study

A mesh sensitivity analysis has been performed with four different quad-based structured grids. The cell repartition is uniform (i.e. $\Delta x = \Delta y$). Table 10.2 gives a representation of the meshes used for this study.

Table 10.2: Structured meshes for cavity cases

Number of cells	Mesh density representation
Mesh 1 (76×76)	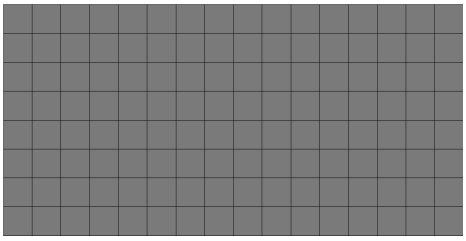
Mesh 2 (190×190)	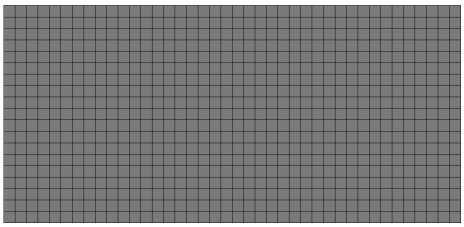
Mesh 3 (500×500)	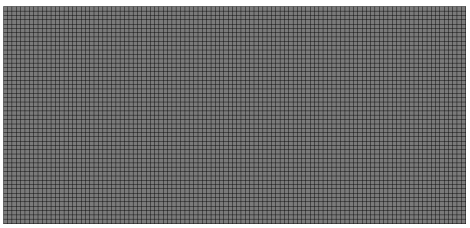
Mesh 4 (700×700)	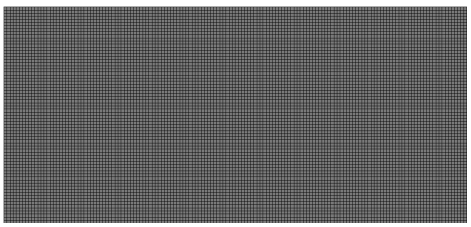

Only a close-up towards the top left corner of the numerical domain is displayed in this table. Temperature, horizontal and vertical velocity fields have been compared along the x and y mid-planes. Figure 10.2 shows the dimensionless results obtained with all four grids.

Dimensionless values of temperature ($\tilde{T}$) are written as:

$$\tilde{T} = \frac{T - T_{cold}}{T_{hot} - T_{cold}} = \frac{T - 273}{10} \ . \tag{10.6}$$

Horizontal and vertical velocities ($\tilde{u}$ and $\tilde{v}$), axial and vertical positions ($\tilde{x}$ and $\tilde{y}$), and time ($\tilde{t}$) are made dimensionless with the length of the cavity $\ell = 38\ mm$ and the thermal diffusivity $\gamma = 1.435 \times 10^{-7}\ m^2/s$:

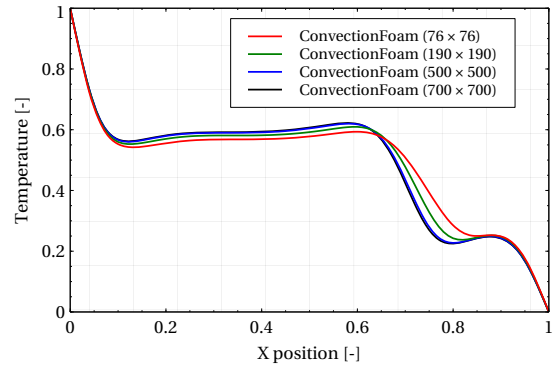

a) Temperature along horizontal line

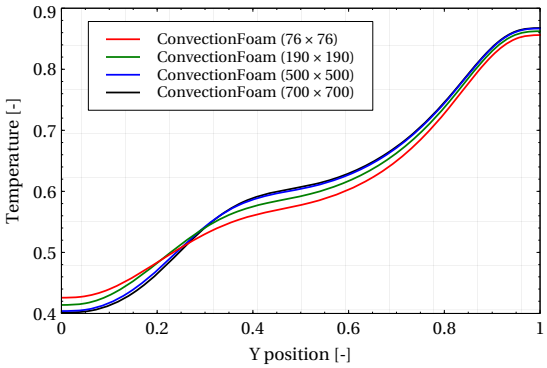

b) Temperature along vertical line

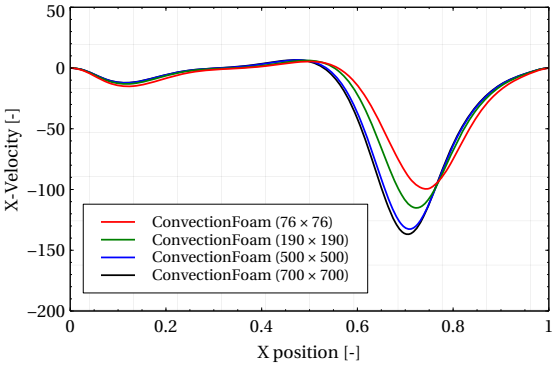

c) U-velocity along horizontal line

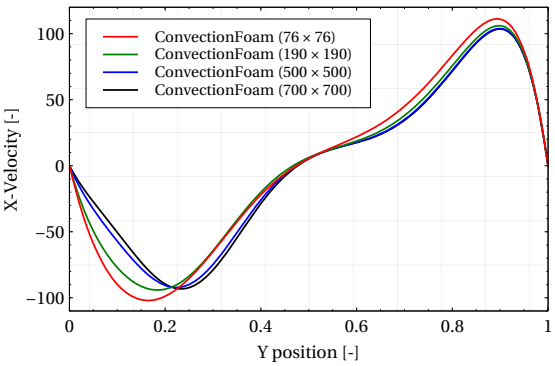

d) U-velocity along vertical line

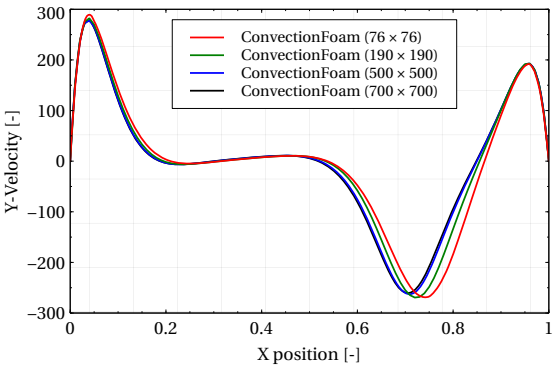

e) V-velocity along horizontal line

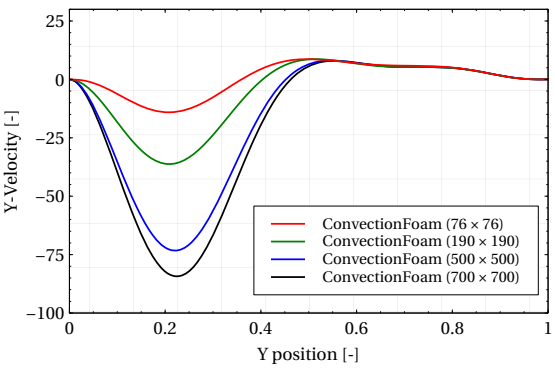

f) V-velocity along vertical line

FIGURE 10.2: Profiles obtained from the mesh sensitivity analysis (ConvectionFoam)

$$
\begin{aligned}
\tilde{u} &= \frac{u\ell}{\gamma} = \frac{u\ 38\times10^{-3}}{1.435\times10^{-7}}\ , \\
\tilde{v} &= \frac{v\ell}{\gamma} = \frac{v\ 38\times10^{-3}}{1.435\times10^{-7}}\ , \\
\tilde{x} &= \frac{x}{\ell} = \frac{x}{38\times10^{-3}}\ , \\
\tilde{y} &= \frac{y}{\ell} = \frac{y}{38\times10^{-3}}\ , \\
\tilde{t} &= \frac{t\gamma}{\ell^2} = \frac{t\times1.435\times10^{-7}}{1.444\times\ 10^{-6}}\ .
\end{aligned}
\tag{10.7}
$$

Results obtained with the two finer meshes (i.e. 500 × 500 and 700 × 700 cells) show a close behaviour for each field studied. The results presented are dimensionless and the maximum deviation between smallest peaks is close to 0.05 mm/s which leads to a maximal error below 10 % between these two meshes. For this reason, the fourth mesh (700 × 700) is used for further validation of the solver in the next section.

10.2.3 Model verification and simulations results

Dimensionless simulated results obtained with the convection model implemented in OpenFOAM are compared to Fluent and frecon solutions (Kowaleski & Rebow, 1999) in Figure 10.3.

Results obtained with ConvectionFoam show good agreement with both frecon and Fluent solutions. Maximum local differences are visible for the vertical y-velocity (Figure 10.3f) and the vertical x-velocity (Figure 10.3d). These differences are due to the fact that the recirculation zone obtained in simulations is slightly shifted between ConvectionFoam and both frecon and Fluent results. These differences can be considered acceptable as they remain below 15%. As a note, it has been observed that results obtained with the numerical simulations practically overlap both Fluent and Frecon results when the horizontal and vertical lines where results are taken are slightly shifted by 0.1 mm. This confirms the previous statement.

Velocity streamlines, temperature and density scalar fields are plotted at different time of the simulation in Table 10.3. In this table, U refers to the velocity magnitude, T to the temperature and rho to the density of water. As can be seen, the hot temperature propagates from the left wall towards the right through time. This phenomenon is more visible at the top of the cavity than in other regions. Natural convection, induced by the hot left wall, generates a flow towards the right of the cavity (especially visible at the top due to gravity effects, for $t < 250\ s$) which is redirected towards the bottom of the cavity at the vicinity of the right cold wall for $t > 250\ s$. It is also clearly noticeable when looking at density profiles for $t < 250\ s$. As mentioned in Section 10.1 and shown in Figure 10.1, the polynomial function used for water density reaches a maximum for $T \sim 278\ K$. The hot and cold heat distributions collide around this temperature value at the top of the cavity where maximum density values are obtained. At later times (i.e. $t > 250\ s$) the influence of the hot wall is more important than the cold one and the maximum density values are visible near the right boundary of the cavity. Results obtained at $t = 750\ s$ and $t = 1500\ s$ show extremely close behaviour for velocity, temperature and density. The steady-state is therefore reached at $t = 1500\ s$. One can ultimately notice that the convection process is faster for $t < 250\ s$ than $t > 250\ s$ where the process starts stabilizing. The flow regime is divided into two clearly discernible recirculation regions. The polynomial water density variation is the origin of the two competing circulations seen in Table 10.3. As explained previously the flow is moving clockwise inside the cavity due to the convection current. Then, due to the density inversion point, a secondary flow is observed at the bottom right corner of the cavity, where the flow is moving counter clockwise. This phenomenon has also been observed

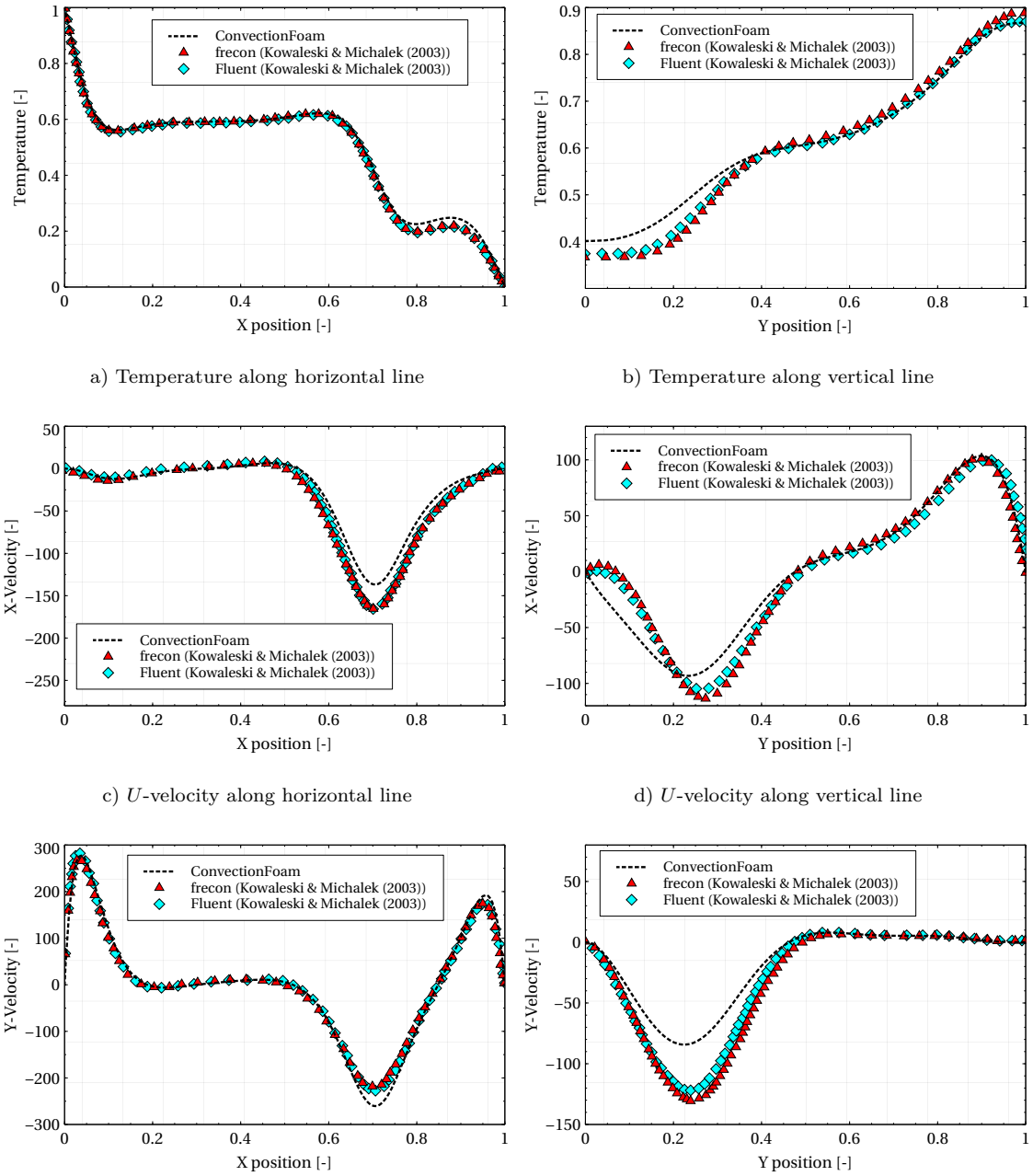

a) Temperature along horizontal line

b) Temperature along vertical line

c) U-velocity along horizontal line

d) U-velocity along vertical line

e) V-velocity along horizontal line

f) V-velocity along vertical line

FIGURE 10.3: Numerical results obtained with ConvectionFoam

in Kowaleski & Rebow (1999). Being able to simulate this feature is extremely important since such flow conditions have a direct impact on the ice layer growth rate during solidification processes. The polynomial density variation permits to simulate the physical behaviour of water as its derivation has been correlated with experimental data. To discuss further the importance of the use of this function, the same case will be discussed in the next section of this thesis, using the standard Boussinesq approximation.

Table 10.3: Numerical results of ConvectionFoam between $t = 100\ s$ and $t = 1500\ s$

$t = 100\ s$	$t = 250\ s$	$t = 750\ s$	$t = 1500\ s$
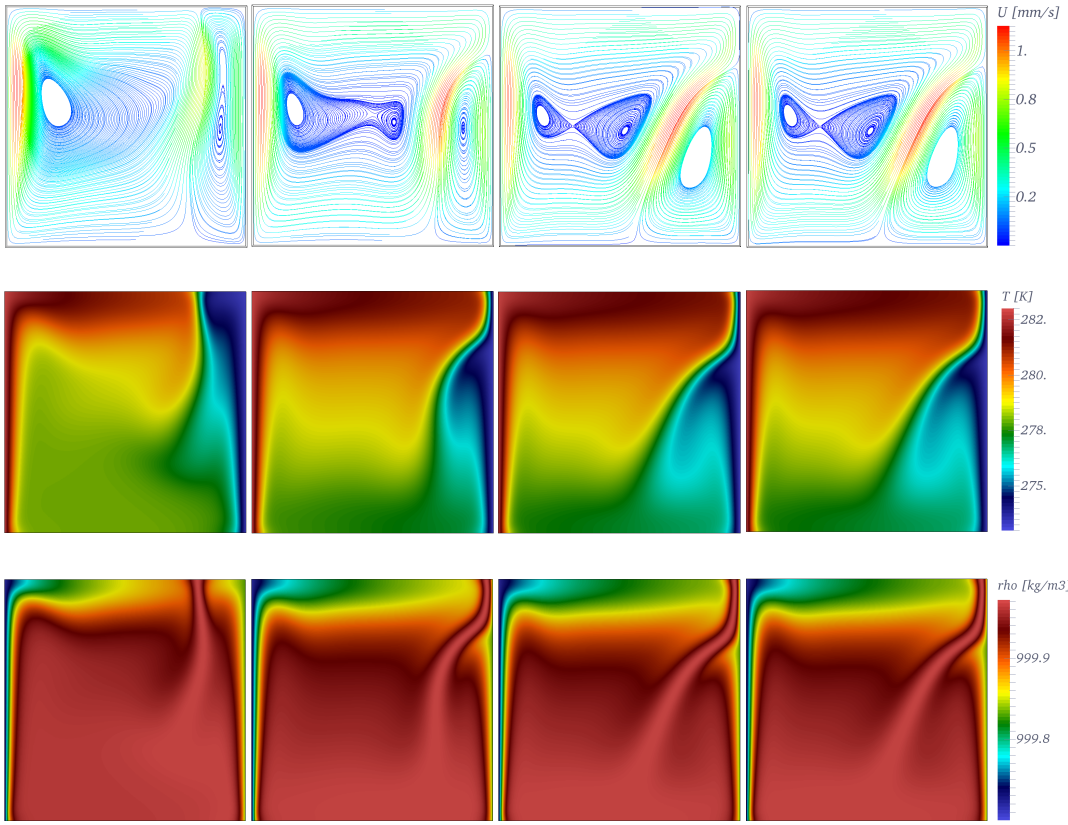			

10.2.4 Comparison with the standard Boussinesq approximation

For comparison, the convection solver distributed by OpenFOAM is used in this section. This solver is called BuoyantBoussinesqPimpleFoam (BBPF) and is suited for both laminar and turbulent unsteady heat transfer simulations of single-phase flows in the Boussinesq approximation. In this formulation, the gravity related terms are expressed as follows :

$$\mathbf{g}\Delta\rho = \mathbf{g}\rho\left[1 - \beta\left(T - T_r\right)\right] \ . \tag{10.8}$$

The density variation is linear and inversion points are no longer present as for ConvectionFoam. In ConvectionFoam, the gravity related terms are expressed as:

$$\mathbf{g}\Delta\rho = \mathbf{g}\left[\rho - \rho(T)\right] \ . \tag{10.9}$$

In the simulations, the thermal expansion coefficient has been set to $\beta = 6.734 \times 10^{-5}\ K^{-1}$ at a reference temperature $T_r = 273\ K$, following Kowaleski & Rebow

TABLE 10.4: Comparisons against standard Boussinesq approximation at $t = 1500\ s$

Quantity	BBPF	CF
Temperature	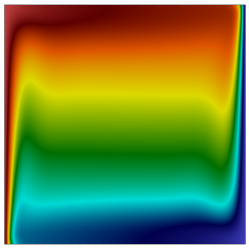	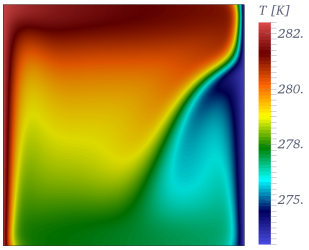
Velocity	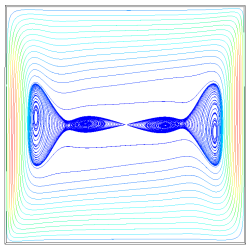	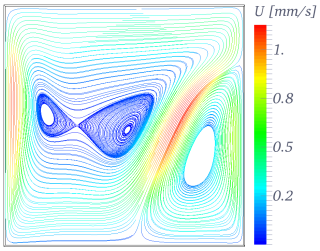

(1999). Table 10.4 presents the numerical results obtained with ConvectionFoam and BuoyantBoussinesqPimpleFoam at $t = 1500\ s$.

It is shown that the convection current obtained with the two solvers is significantly different. The solution obtained with BuoyantBoussinesqPimpleFoam shows a linear pattern for both temperature and velocity fields whereas the inversion point due to density variation is clearly visible for ConvectionFoam. Small changes in density (in this case 0.2 $kg.m^{-3}$) induce significant differences in the flow pattern. This is extremely important as the ice layer growth and shape is directly influenced by the motion of the fluid. A comparison is made against experimental measurements of water in natural convection in the next section, in order to investigate in more details the importance of the polynomial density function feature of ConvectionFoam.

10.2.5 Comparison with Experimental measurements

Experimental investigations of Giangi et al. (2000) are used here for qualitative comparisons. In this paper, the natural convection of water inside squared cavities is investigated. The operating conditions are slightly different from the case discussed so far, as a fixed heat flux of 20 $W.m^{-2}.K$ for the top and bottom walls has been used during experiments while adiabatic conditions were considered in the numerical simulations. Table 10.5 gives a comparison between experimental, BuoyantBoussinesqPimpleFoam and ConvectionFoam results at $t = 1500\ s$ of simulation.

Table 10.5 clearly shows that results obtained from ConvectionFoam are very close to the experiments of Giangi et al. (2000). Only noticeable discrepancies can be found on the exact location of the inversion point, where the two counter circulations collide. As mentioned previously, simulations differ slightly from experiments since a fixed heat flux boundary condition was used in the later case whereas the boundary conditions for simulations were set to adiabatic. Therefore, the inversion

Table 10.5: Comparisons against experiments at $t = 1500\ s$

Experiments	BBPF	CF
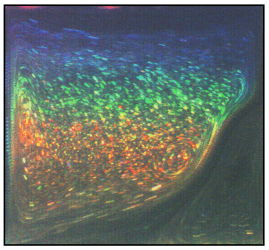	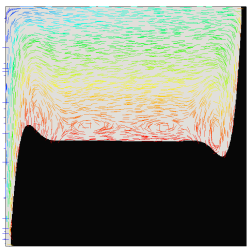	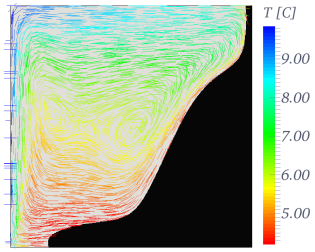
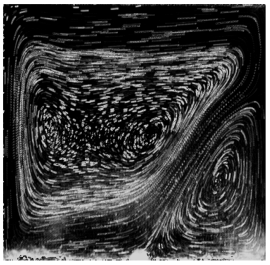	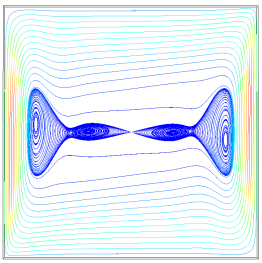	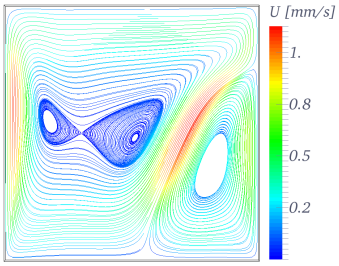

point seems shifted a bit more towards the bottom of the domain during experiments than during simulations. However the agreement remains acceptable for both temperature and velocity fields. Larger discrepancies are shown for BuoyantBoussinesqPimpleFoam. As the density variation is linear, no inversion point is obtained with this solver and only one convective current is visible in Table 10.5. The flow pattern therefore presents significant discrepancies when compared to experiments. When using this solver, the ice layer shape growing from the right wall towards the left wall is highly assumed to be linear, which is not the case for both experiments and ConvectionFoam results. Results obtained from ConvectionFoam have proven to be accurate enough to simulate solidification processes. This will be discussed in the next chapter of this thesis.

Chapter 11

Solidification process with mushy region modelling

A solidification solver is implemented in OpenFOAM and discussed in this chapter. This solver is called IcingFoam and will sometimes be referred to as IF. The solver uses an enthalpy-porosity based model and several techniques (described mostly here and in Chapter 9) are used to achieve very accurate results when compared to other numerical and experimental data. A polynomial function has been used for the density of the fluid and an error function is implemented to speed-up computations and approach correctly the transition between solid and liquid phase. Finally, the partially solidified region is treated as a mushy-region, assumed to behave as a porous media. Additional modelling effort is necessary to take into account phase changes phenomena in the momentum equations. This is accomplished by using Darcy's law. The present solver is found to behave very well for water freezing inside cavities and cylindrical enclosures.

Contents

11.1 Solidification model with mushy region (IF) **99**
11.1.1 Energy conservation equation 99
11.1.2 Temperature dependent fluid properties 101
11.1.3 Mass and momentum conservation equations 101
11.2 Numerical simulations of water freezing in cavities **102**
11.2.1 Numerical campaign 102
11.2.2 Grid independence study 102
11.2.3 Model verification and simulations results 106
11.2.4 Comparison with Experimental measurements 109
11.3 Numerical simulations of water freezing in cylinders **110**
11.3.1 Numerical campaign 110
11.3.2 Grid independence study 110
11.3.3 Model verification and simulations results 112

11.1 Solidification model with mushy region (IF)

11.1.1 Energy conservation equation

An enthalpy-porosity based model (Voller & Prakash, 1987) has been implemented to simulate water freezing. This solver is called IcingFoam (IF). The energy conservation equation is expressed as a function of the total enthalpy of the system H:

$$\frac{\partial \rho H}{\partial t} + u\frac{\partial \rho H}{\partial x} + v\frac{\partial \rho H}{\partial y} = \lambda \Delta T \ , \tag{11.1}$$

where u and v denote the velocity components in x and y directions respectively and λ is the thermal conductivity of the fluid. H can be expressed as a function of the specific sensible enthalpy h:

$$H = h + \Delta H \Rightarrow H = h + \alpha_\ell L \ , \tag{11.2}$$

where α_ℓ is the liquid volume fraction and

$$h = h_r + \int_{T_r}^{T} c_p dT \ . \tag{11.3}$$

ΔH in Equation 11.2 represents the evolution of the latent heat L, i.e. the heat released during freezing. The latent heat evolution is governed by the volume fraction of liquid water α_ℓ. The solid volume fraction (in this study case the volume fraction of ice) is denoted f_s, its value is $f_s = 1 - \alpha_\ell$. The phase change process is usually modelled by expressing the liquid volume fraction as a function of temperature (ANSYS, 2011) and (StarCCM+, 2012). Upper (T_{liq}) and lower (T_{sol}) temperature bounds are used to define when freezing or melting events occur:

$$\alpha_\ell = \begin{cases} 1 & T > T_{liq} \ , \\ \frac{T - T_{sol}}{T_{liq} - T_{sol} + \varepsilon} & T_{sol} < T < T_{liq} \ , \\ 0 & T < T_{sol} \ . \end{cases} \tag{11.4}$$

T_{liq} and T_{sol} stand for the liquidus and solidus temperatures, respectively. A small constant ($\varepsilon = 0.0001$) is added in the present model so that computation can be performed for phase change of pure materials (i.e. $T_{sol} = T_{liq}$) and to avoid numerical difficulties. Modelling the liquid volume fraction as a temperature function allows to compute phase change of impure material, $T_{liq} \neq T_{sol}$. Considering the reference specific enthalpy $h_r = 0$ for convenience, the total enthalpy can be written as:

$$H = \int_{T_r}^{T} c_p dT + \alpha_\ell L \ . \tag{11.5}$$

Substituting and deriving this expression into the energy conservation equation leads to:

$$\begin{aligned}
\frac{\partial \rho \left(C_p T + \alpha_\ell L\right)}{\partial t} + u\frac{\partial \rho \left(C_p T + \alpha_\ell L\right)}{\partial x} + v\frac{\partial \rho \left(C_p T + \alpha_\ell L\right)}{\partial y} &= \lambda \Delta T \ , \\
\frac{\partial \rho C_p T}{\partial t} + u\frac{\partial \rho C_p T}{\partial x} + v\frac{\partial \rho C_p T}{\partial y} + L\left[\frac{\partial \rho \alpha_\ell}{\partial t} + u\frac{\partial \rho \alpha_\ell}{\partial x} + v\frac{\partial \rho \alpha_\ell}{\partial y}\right] &= \lambda \Delta T \ , \\
\frac{\partial \rho C_p T}{\partial t} + u\frac{\partial \rho C_p T}{\partial x} + v\frac{\partial \rho C_p T}{\partial y} &= \lambda \Delta T + S_t \ .
\end{aligned} \tag{11.6}$$

S_t represents the source term added to the energy equation to compute the phase change process:

$$S_t = -L\left[\frac{\partial \rho \alpha_\ell}{\partial t} + u\frac{\partial \rho \alpha_\ell}{\partial x} + v\frac{\partial \rho \alpha_\ell}{\partial y}\right] \ . \tag{11.7}$$

Instead of the linear liquid volume fraction evolution in Equation 11.4, an error function has been used. This has been proposed in Rosler & Bruggermann (2011), where a melting solver based on a linear Boussinesq approximation has been validated against experiments:

$$\alpha_\ell = 0.5 + 0.5 \ erf\left(4\ \frac{T - \frac{T_{liq}+T_{sol}}{2}}{T_{liq} - T_{sol} + \varepsilon}\right) \ . \tag{11.8}$$

The deviation between the theoretical linear profile and the error function of the liquid volume fraction is displayed in Figure 11.1.

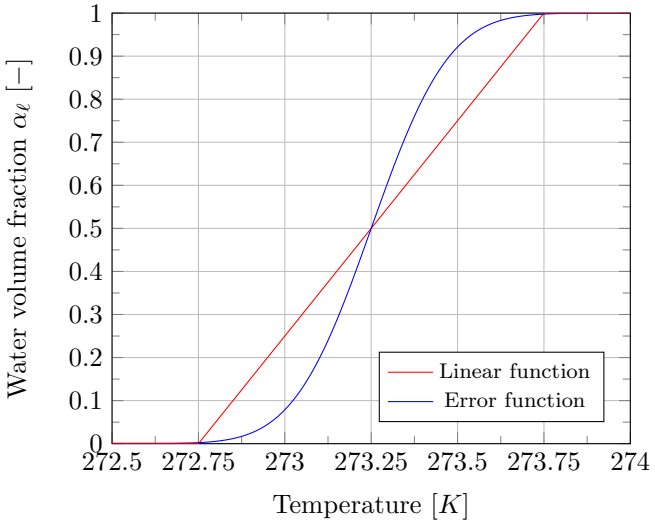

FIGURE 11.1: Deviation between linear and error function for α_ℓ between T_{sol} = 272.75K and $T_{liq} = 273.75\ K$

As shown, the deviation between the two methods is fairly low. Therefore this error function provides a promising way to decrease the computational time of solidification simulations.

11.1.2 Temperature dependent fluid properties

The polynomial density variation of water used in ConvectionFoam (Equation 10.1) is also used in IcingFoam. Figure 10.1 shows that the polynomial density variation of water is not suitable for negative temperatures as the density should take the value of the ice density. To overcome this limitation, the phase change is accounted for in IcingFoam and the total density of the medium $\rho(T)'$ is expressed as the sum of solid $\rho_s f_s$ and liquid $\rho(T)\alpha_\ell$ contributions.

$$\rho(T)' = \rho(T)\alpha_\ell + \rho_s f_s \ . \tag{11.9}$$

A smooth transition can therefore be achieved between water and ice density values, for negative temperatures. Any other medium property can be expressed in a similar way:

$$\begin{aligned} C_p &= C_{p_\ell}\alpha_\ell + C_{p_s} f_s \ , \\ \lambda &= \lambda_\ell \alpha_\ell + \lambda_s f_s \ , \\ \mu &= \mu_\ell \alpha_\ell + \mu_s f_s \ . \end{aligned} \tag{11.10}$$

11.1.3 Mass and momentum conservation equations

The effect of water freezing is only modelled in the energy equation with the enthalpy-based model. Therefore, additional source terms are necessary in the momentum equations to compute the sink of velocity in the solidified region. Solid and mushy regions are assumed to behave as porous media and the Darcy coefficient D_c is used to model the sink of velocity. Liquid and solid volume fractions act as triggers for the source term such as:

$$\begin{aligned} S_{m_x} &= D_c \frac{f_s^2}{\alpha_\ell^3 + \varepsilon} u \ , \\ S_{m_y} &= D_c \frac{f_s^2}{\alpha_\ell^3 + \varepsilon} v \ . \end{aligned} \tag{11.11}$$

S_{m_x} and S_{m_y} are the x and y additional source terms contributions to the momentum equations, respectively. The Darcy constant D_c is chosen high enough ($\simeq 10^8$) so that the velocity in the solid zone can reach zero and ε is a small constant to avoid numerical problems in the fully solid region ($\alpha_\ell = 0$). Source terms tend to zero when $f_s = 0$ and therefore, no sink of velocity is added to the momentum equations in the liquid region. Besides, when $f_s = 1$ and $\alpha_\ell = 0$ the terms tend to infinity and the velocity in the solid region tends to zero.

Momentum equations for the solidification solver can be expressed with the con-

tribution of the Darcy source terms S_{m_x} and S_{m_y}:

$$\begin{aligned}
&\frac{\partial u}{\partial x} + \frac{\partial v}{\partial y} = 0 \ , \\
&\frac{\partial \rho u}{\partial t} + u\frac{\partial \rho u}{\partial x} + v\frac{\partial \rho u}{\partial y} = -\frac{\partial p}{\partial x} + \mu \Delta u - S_{m_x} \ , \\
&\frac{\partial \rho v}{\partial t} + u\frac{\partial \rho v}{\partial x} + v\frac{\partial \rho v}{\partial y} = -\frac{\partial p}{\partial y} + \mu \Delta v - g[\rho(T)' - \rho] - S_{m_y} \ .
\end{aligned} \tag{11.12}$$

11.2 Numerical simulations of water freezing in cavities

11.2.1 Numerical campaign

The test case presented in this section stands as a numerical benchmark for water freezing studies. Numerical simulations have been performed with the commercial CFD code Fluent (ANSYS, 2011) and with the in-house code nc4 mar in Kowaleski & Rebow (1999). Simulation results obtained with the solidification solver implemented in OpenFOAM, are compared to these results. The water freezing process induced by a temperature gradient between two opposite walls is analyzed in a squared shape cavity of height $\ell = 38\ mm$. Upper and lower walls are assumed adiabatic and a temperature gradient is induced from the left wall ($T_{w_\ell} = 283\ K$) to the right wall ($T_{w_r} = 263\ K$). As mentioned previously, the natural convection solver is used initially to reach a pseudo-steady state solution.

After initializing with the natural convection solution, the solidification solver is run. For the sake of brevity, numerical results from the convection solver will not be discussed here as they have already been presented in Chapter 10. The right wall is then suddenly cooled down from $T_{w_r} = 273\ K$ to $T_{w_r} = 263\ K$ so that freezing can occur when running the solidification solver. Table 11.1 provides the fluid properties from Kowaleski & Rebow (1999) used for the solidification study.

11.2.2 Grid independence study

Simulations have been carried out for a physical time of 100 seconds. A mesh sensitivity analysis has been performed with four different quad-based structured grids. Temperature, horizontal and vertical velocity fields have been compared along the x and y mid-planes. Figures 11.2, 11.3 and 11.4 show the scalar fields, where the black lines depict the position of field evaluation (from bottom to top for the vertical lines and from left to right for the horizontal lines), and the dimensionless results obtained with all four grids.

Temperature distributions, plotted along the horizontal line in Figures 11.2a and 11.2b, show a decrease of the temperature from the left wall of the cavity to $x \simeq 0.1$, caused by the temperature gradient between the hot wall $T_{w_\ell} = 283\ K$ and the temperature field from the ConvectionFoam steady state solution. At $x > 0.1$ the

Table 11.1: Water properties for the solidification study

Water properties	Symbol	Values	Units
Water density	ρ_ℓ	999.8	$kg.m^{-3}$
Ice density	ρ_s	916.8	$kg.m^{-3}$
Dynamic viscosities	$\mu_\ell = \mu_s$	0.001003	$kg.m^{-1}.s^{-1}$
Heat capacities	$C_{p_\ell} = C_{p_s}$	4182	$J.kg^{-1}.K^{-1}$
Water thermal conductivity	λ_ℓ	0.6	$W.m^{-1}.K^{-1}$
Ice thermal conductivity	λ_s	2.26	$W.m^{-1}.K^{-1}$
Latent heat	L	335 000	$J.kg^{-1}$
Liquidus temperature	T_{liq}	273.3	K
Solidus temperature	T_{sol}	273.0	K
Darcy constant	D_c	10^8	$kg.m^{-3}.s^{-1}$

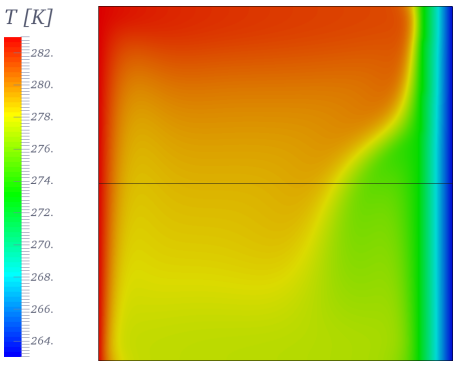

a) Temperature scalar field

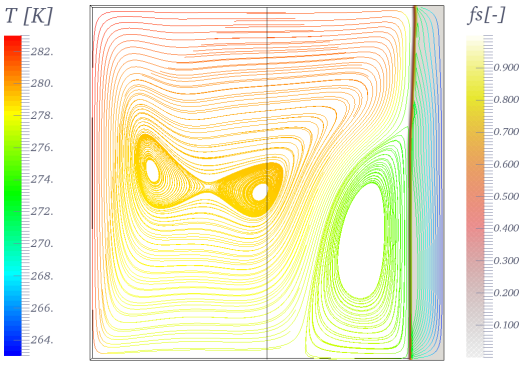

c) Temperature streams and ice volume fraction (grey)

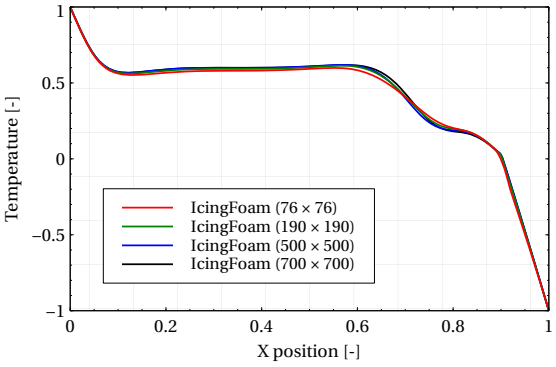

b) Temperature along horizontal line

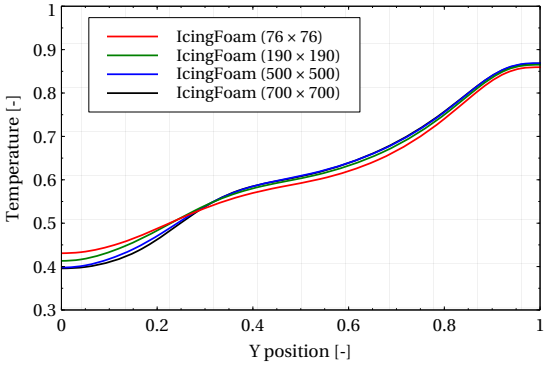

d) Temperature along vertical line

Figure 11.2: Temperature profiles obtained from the mesh sensitivity analysis

upper flow recirculation is well captured by the numerical model and induces a slow continuous increase of the temperature until $x \simeq 0.6$, where the influence of the right cold wall $T_{w_r} = 263\ K$ becomes significant. Therefore, the colliding of upper and lower circulation regions induces a sudden decrease of the temperature field in the region $0.6 < x < 0.9$. Finally, next to the right wall of the cavity, the temperature

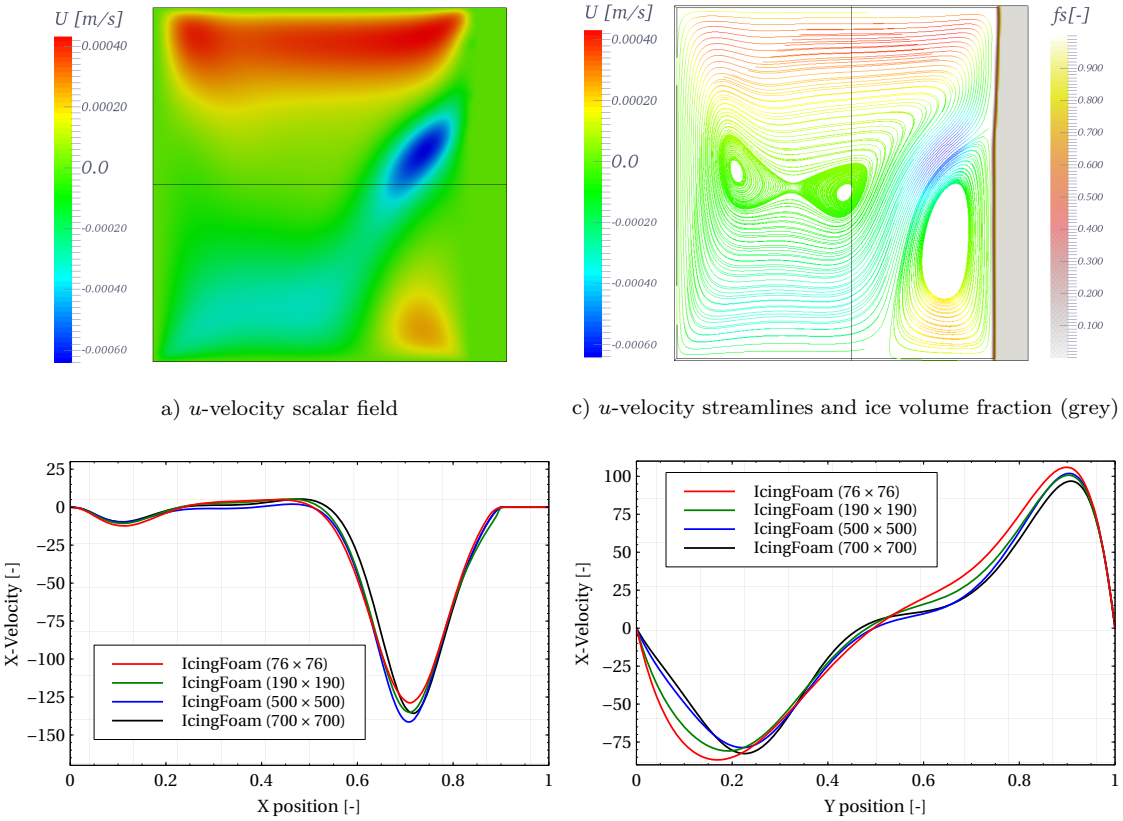

a) u-velocity scalar field

c) u-velocity streamlines and ice volume fraction (grey)

b) u-velocity along horizontal line

d) u-velocity along vertical line

FIGURE 11.3: U velocity profiles obtained from the mesh sensitivity analysis

decreases drastically to reach the minimal wall temperature $T_{w_r} = 263\ K$.

On the contrary, the temperature field, along the vertical line increases continuously from the bottom to the top of the cavity, see Figures 11.2c and 11.2d. Due to the natural convection and buoyancy effects, the temperature at the bottom of the cavity is relatively low and increases slowly in the region $0 < y < 0.15$. The interaction between lower and upper recirculations, clearly visible in Figure 11.2c, occurs at $y \simeq 0.15$ and induces a faster increase of the temperature in the region $0.15 < y < 0.4$. In the upper recirculation region $0.4 < y < 1$, the temperature increases continuously since gravity effects are less important and thus the temperature is higher than at the bottom of the cavity.

The u-velocity in Figure 11.3a, plotted along the horizontal line in Figure 11.3b, shows a nearly flat profile, slightly oscillating from the left hot wall to $x \simeq 0.5$. A sudden decrease of the velocity is visible around $x \simeq 0.6$, where the hot and cold recirculation regions collide. This decrease corresponds to negative velocity vectors induced by the cooling of the upper recirculation by the ice layer which forms next to the cold wall. Therefore, velocity components of the upper recirculation are reflected by the solid ice layer and this phenomenon affects the central part of the cavity. The velocity components increase in the direction of the right wall for $0.7 < x < 0.9$ to reach a constant null value corresponding to the fluid velocity in the iced region $0.9 < x < 1$.

The u-velocity profiles, along the vertical line, in Figures 11.3c and 11.3d show a

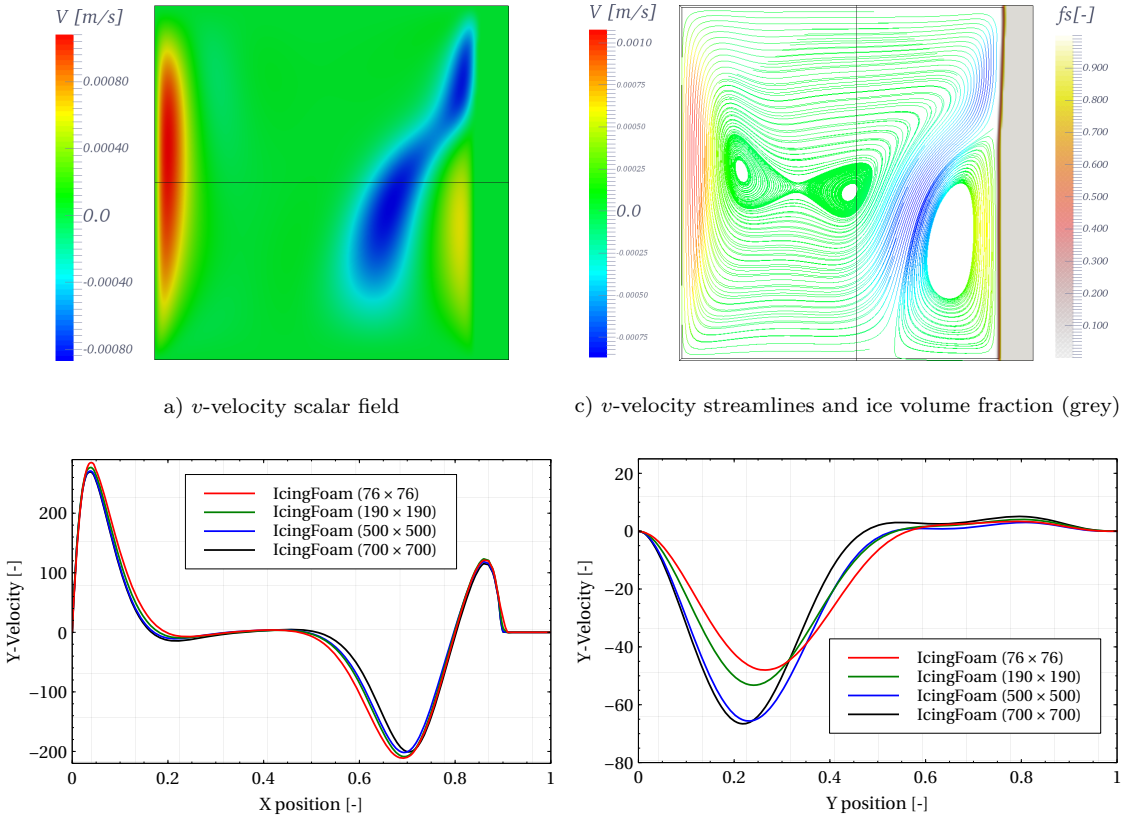

a) v-velocity scalar field

c) v-velocity streamlines and ice volume fraction (grey)

b) v-velocity along horizontal line

d) v-velocity along vertical line

Figure 11.4: V velocity profile obtained from the mesh sensitivity analysis

first negative peak around $y \simeq 0.2$ due to the negative velocity vectors created by the interaction between the upper recirculation and the solid ice layer. Past this region $0.2 < y < 0.9$, the velocity profile displays a constant increase. This phenomenon is due to the upper recirculation where the velocity magnitude appears higher in the top region. As the wall is adiabatic and the velocity is zero at the top and bottom walls, a sink of velocity is observed for $0.9 < y < 1$ to reach zero.

The v-velocity profiles, along the horizontal line, in Figures 11.4a and 11.4b show a first positive peak in the vicinity of the left hot wall for $0 < x < 0.15$. This corresponds to the first part of the upper recirculation region, where the upward velocity flux induced by the hot left wall is added to the momentum equation. The horizontal y-velocity profile seems to stabilize around zero for $0.2 < y < 0.5$ as no velocity components are formed in the middle part of the upper recirculation region. Similarly to the u-velocity profile along the horizontal line shown in Figures 11.3a and 11.3b, the colliding between the upper flow circulation and the ice layer forming from the right cold wall, induces negative velocity vectors in the y mid plane for $0.5 < x < 0.7$. The horizontal v-velocity profile then increases in the region $0.7 < x < 0.85$. This increase reflects the effect that the lower recirculation region has on the flow structure. Finally the velocity tends to zero in the region $0.85 < x < 1$, which corresponds to the sink of velocity in the iced region.

The v-velocity profiles, along the vertical line, shown in Figures 11.4c and 11.4d display a negative peak at $y \simeq 0.25$ which corresponds to the negative velocity vec-

tors caused by the collision between the upper recirculation region and the growing ice layer on the right cold wall.

The mesh sensitivity analysis in Figure 11.2 to 11.4 shows that for all fields of study, results obtained with the two finest grids (500×500 and 700×700) nearly overlap each other. The finer of these two meshes has however been selected for the second part of this study since the increase of simulation time is marginal and the results are slightly more accurate.

Note that for all meshes, the time-step has been chosen so that the critical courant number remained less than 1.0 in each computational cell. The time-step value $\Delta t = 0.05\ s$ was used to meet this requirement.

11.2.3 Model verification and simulations results

Dimensionless simulated results obtained with the solidification model implemented in OpenFOAM are compared to Fluent and nc4 mar solutions (Kowaleski & Rebow, 1999) in Figure 11.6.

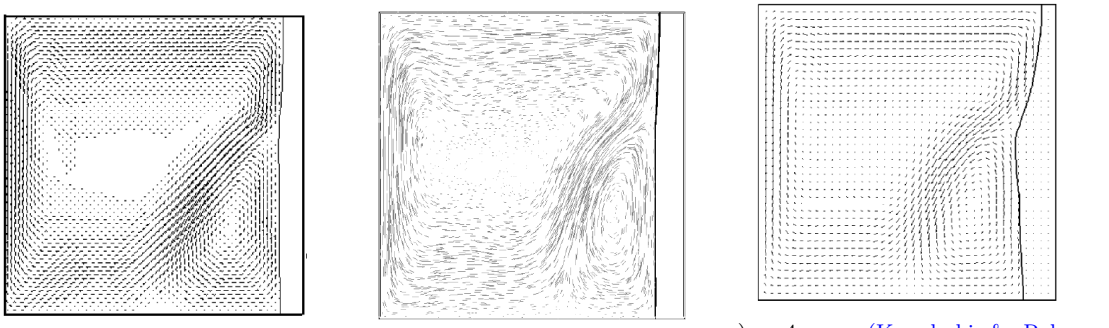

a) Fluent (Kowaleski & Rebow, 1999) b) IcingFoam c) nc4 mar (Kowaleski & Rebow, 1999)

FIGURE 11.5: Details of the liquid-solid interface at $t = 100\ s$

Results obtained with IcingFoam show good agreement with Fluent. Maximum local differences are visible for the vertical y-velocity (Figure 11.6f). It has been noticed during the numerical simulations, that the IcingFoam results, when plotted 0.1 mm far from the vertical line position (i.e. $x = 19\ mm$) nearly overlapped Fluent's results. This shows that the ice shape forming on the right hand side of the domain can affect slightly the results. Larger differences are visible between IcingFoam and the nc4 mar university code. These discrepancies might be due to the different formulation of the source term S_t in Equation 11.7. In nc4 mar, the source term S_t is expressed as:

$$S_t = -L\left(\frac{\partial \rho \alpha_\ell}{\partial t}\right) , \tag{11.13}$$

whereas the contribution of the latent heat released during the freezing process is extended to include the divergence part of the velocity components in both IcingFoam and Fluent solvers. The authors in Kowaleski & Rebow (1999) also discussed the discrepancies between nc4 mar and Fluent concerning the liquid-solid interface.

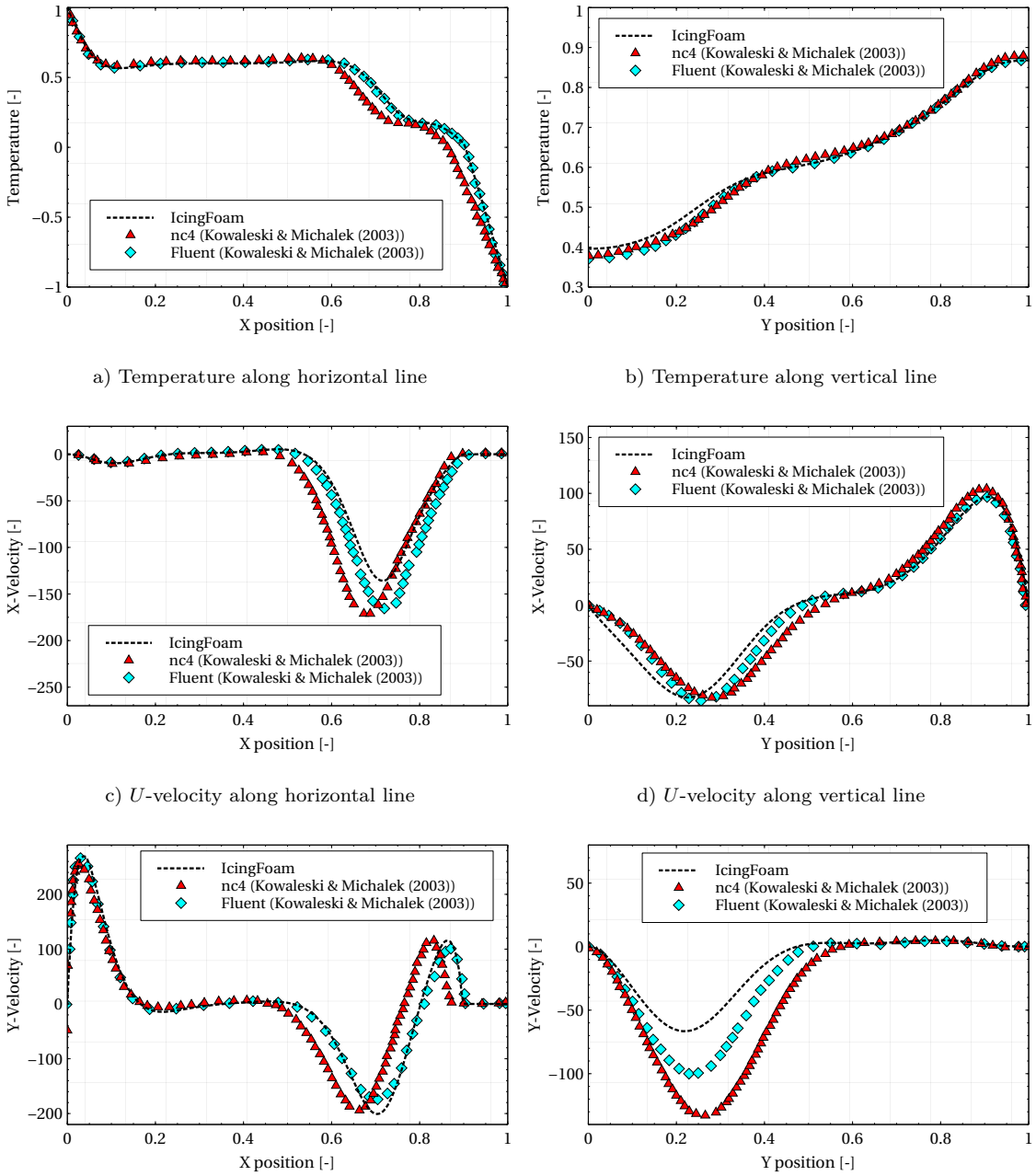

a) Temperature along horizontal line

b) Temperature along vertical line

c) U-velocity along horizontal line

d) U-velocity along vertical line

e) V-velocity along horizontal line

f) V-velocity along vertical line

Figure 11.6: Numerical results obtained with IcingFoam

They obtained a well-developed "belly" shape front in the middle part of the ice layer at $t = 100\ s$ with nc4 mar while Fluent predicted a rather uniform flat ice layer, see Figure 11.5.

Numerical simulations with IcingFoam also revealed the formation of a near flat layer at $t = 100\ s$, similarly to the Fluent solution. The differences between nc4 mar and both Fluent and IcingFoam at the solid/liquid interface might be caused by the over-prediction of the velocity magnitude by nc4 mar, which therefore predicts a faster formation of the belly-shaped ice front.

Scalar solid volume fraction, velocity magnitude streamlines, temperature scalar

TABLE 11.2: Solidification rate process with IcingFoam between $t = 100\ s$ and $t = 1500\ s$

$t = 100\ s$	$t = 250\ s$	$t = 750\ s$	$t = 1500\ s$
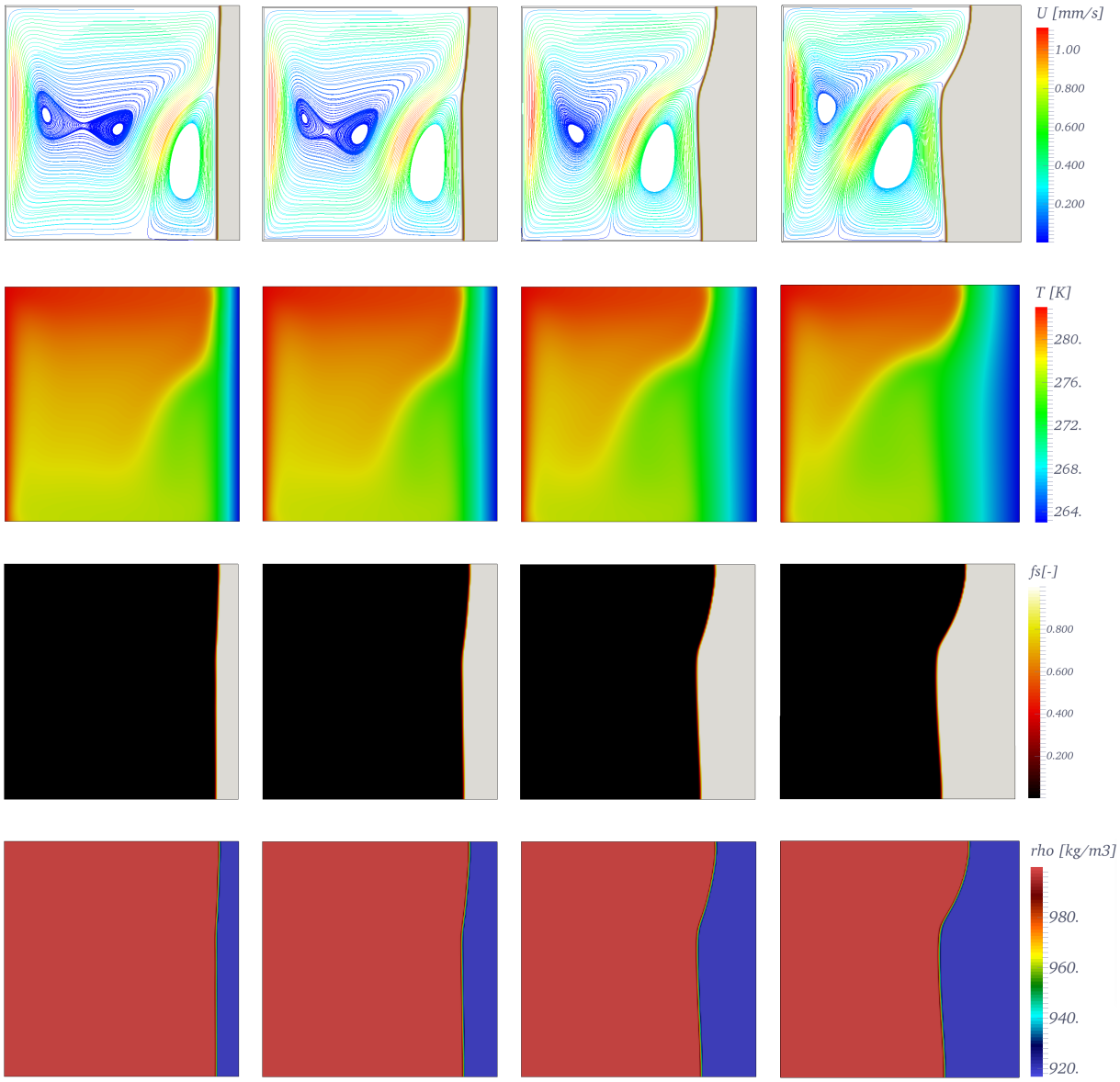			

and density scalar fields obtained with IcingFoam, at different times, are shown on Table 11.2. In this table, the grey color corresponds to a solid volume fraction equal to 1 (i.e. ice region) and the black color corresponds to a solid volume fraction equal to 0 (i.e. water region). As can be seen, the belly-shaped ice layer is present, but appears at a later time. The solidification rate seems much faster at $t < 750$ s than at $t > 750$ s. The ice layer formed in the vicinity of the right cold wall seems to expand uniformly in the bulk region at the beginning of the simulation ($t < 100$ s) whereas at later times ($t > 100$ s), the upper recirculation lowers drastically the solidification rate in the top region of the cavity. This has also been noticed in Kowaleski & Rebow (1999).

To summarize, results obtained with the IcingFoam solver showed good agreement with the industry standard CFD code Fluent at the liquid-solid interface. A qualitative good agreement was also obtained for temperature, horizontal and vertical velocity distributions. Increasing the number of iterations per time-step might slightly improve the results even if a decrease of 4 orders of magnitude has been obtained for all residuals. The current simulations were performed with 5 iterations/time-step for the pressure-velocity correction while 15 were used in Fluent. However, this would significantly decrease the computational efficiency of the current solver. Results obtained are finally compared to experimental measurements in the next section of this thesis.

11.2.4 Comparison with Experimental measurements

Experiments have been performed to obtain the solidification of water in cavities (Giangi et al., 2000). As mentioned previously, the operating conditions between experiments and simulations were slightly different. Figure 11.7 gives a comparison between the experimental work from Giangi et al. (2000) and presents the numerical solution obtained with IcingFoam.

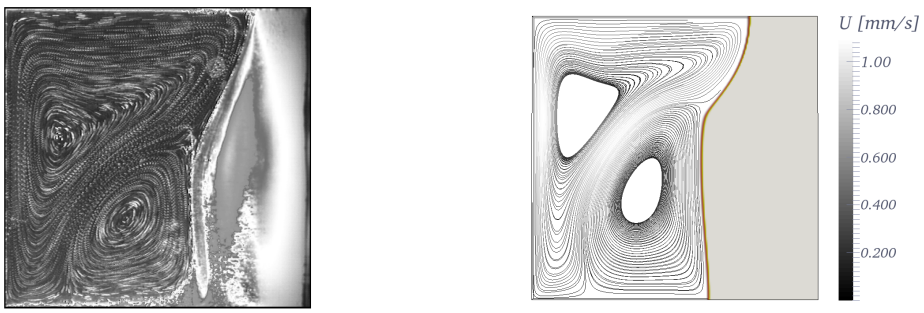

a) Experimental solution

b) IcingFoam solution

Figure 11.7: Comparisons between experimental work and IcingFoam solution for water freezing inside cavities at $t = 2600\ s$

A good agreement is found between the experimental data and the numerical solution of IcingFoam. The top circulation region is slightly larger in simulations when compared to experiments. As a result, the ice layer (at the top) is smoother in experiments. This is attributed to the fact that a heat flux boundary condition was used in experiments. The natural convection solution was therefore different in simulations and experiments, producing these local discrepancies. The overall result obtained with IcingFoam is however very close to measurements.

11.3 Numerical simulations of water freezing in cylinders

11.3.1 Numerical campaign

The validation of IcingFoam is extended further to investigate the water freezing process in a cylindrical enclosure of diameter $d = 82.8$ mm slowly cooled down by a coolant flowing around its external surface at $T_c = -18\ °C$ (Chen & Lee, 1998). The cylindrical enclosure used in experiments is $t_h = 2.5$ mm thick and is initially filled up with pure water at temperature $T_i = 21\ °C$. For the sake of simplicity, the thickness of the enclosure has been ignored in the numerical simulations. The test section and operating conditions will be discussed further later in this section. A 2D model has been designed to reproduce the experimental results. The cooling effect is obtained by keeping the wall temperature at $T_w = -18\ °C$. Table 11.3 provides the water properties from Chen & Lee (1998) used in this study.

TABLE 11.3: Water properties for the freezing process in the cylindrical enclosure

Water properties	Symbol	Values	Units
Water density	ρ_ℓ	999.8	$kg.m^{-3}$
Ice density	ρ_s	916.8	$kg.m^{-3}$
Water kinematic viscosity	ν_ℓ	1.79×10^{-6}	$m^2.s^{-1}$
Ice kinematic viscosity	ν_s	2.0×10^{-6}	$m^2.s^{-1}$
Heat capacities	$c_{p_\ell} = c_{p_s}$	4202	$J.kg^{-1}.K^{-1}$
Water thermal conductivity	λ_ℓ	0.56	$W.m^{-1}.K^{-1}$
Ice thermal conductivity	λ_s	2.26	$W.m^{-1}.K^{-1}$
Latent heat	L	335 000	$J.kg^{-1}$
Liquidus temperature	T_{liq}	$273.3; 0.15$	$K;° C$
Solidus temperature	T_{sol}	$273.0; -0.15$	$K;° C$
Darcy constant	D_c	10^8	$kg.m^{-3}.s^{-1}$

11.3.2 Grid independence study

A mesh sensitivity analysis is performed with five different O-grid structured meshes. Tables 11.4 and 11.5 give a representation of these meshes. Only the top left part of the cylindrical enclosure is displayed on these tables.

Velocity components are plotted at $t = 2500\ s$ along the horizontal axis in the middle of the enclosure, see Figure 11.8. A time step $\Delta t = 0.05\ s$ has been used and the constraint $CFL_m < 1$ has been respected in all simulations. As can be noticed, numerical results of velocity obtained with the two finest meshes (Meshes 4 and 5) perfectly overlap each other. Results obtained with Mesh 4 have therefore been selected and compared with experiments from Chen & Lee (1998), these numerical results being mesh-independent.

Table 11.4: Structured meshes for cylindrical enclosure cases (M1, M2 and M3)

Mesh 1 (3 104 nodes)	Mesh 2 (7 684 nodes)	Mesh 3 (39 784 nodes)
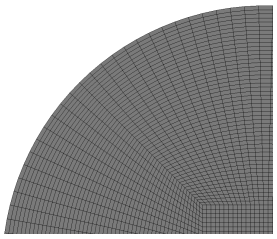	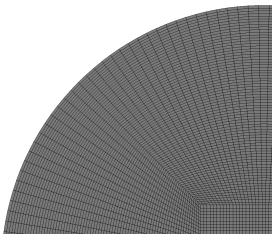	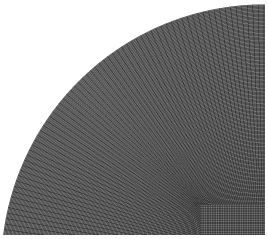

Table 11.5: Structured meshes for cylindrical enclosure cases (M4 and M5)

Mesh 4 (111 304 nodes)	Mesh 5 (198 404 nodes)
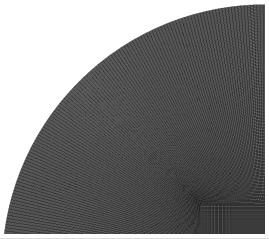	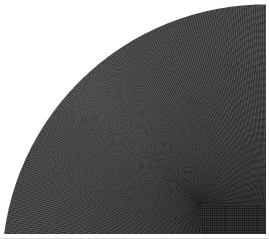

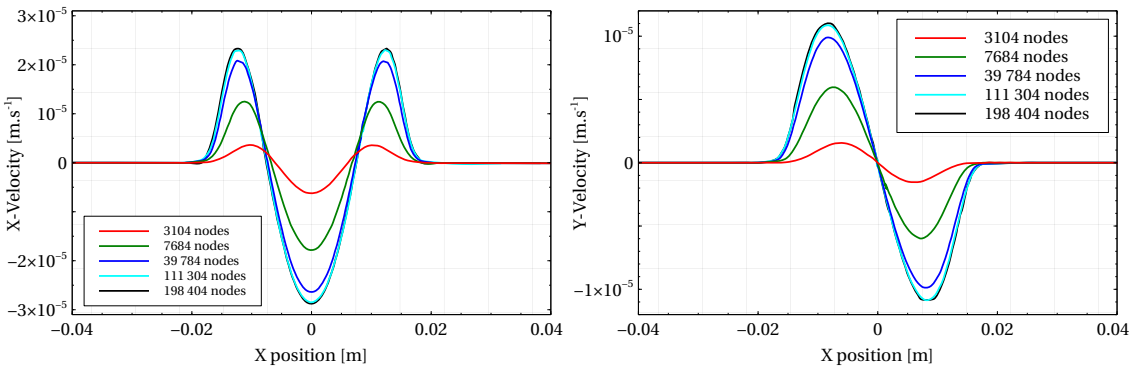

a) U velocity profile

b) V velocity profile

Figure 11.8: Mesh sensitivity analysis for a water freezing process in a cylindrical enclosure after 42 minutes of physical time, along x-axis in the y-middle plane

11.3.3 Model verification and simulations results

Simulations have been run for a physical time $t = 5000\ s$. Figure 11.9 shows the temperature profiles on the top, center, side and bottom parts of the computational domain, keeping the wall temperature at $T_w = -18\ °C$. The temperature in each part of the cylindrical enclosure decreases slowly in time from the ambient temperature ($T = 21\ °C$) to the wall temperature. The water therefore progressively turns into ice.

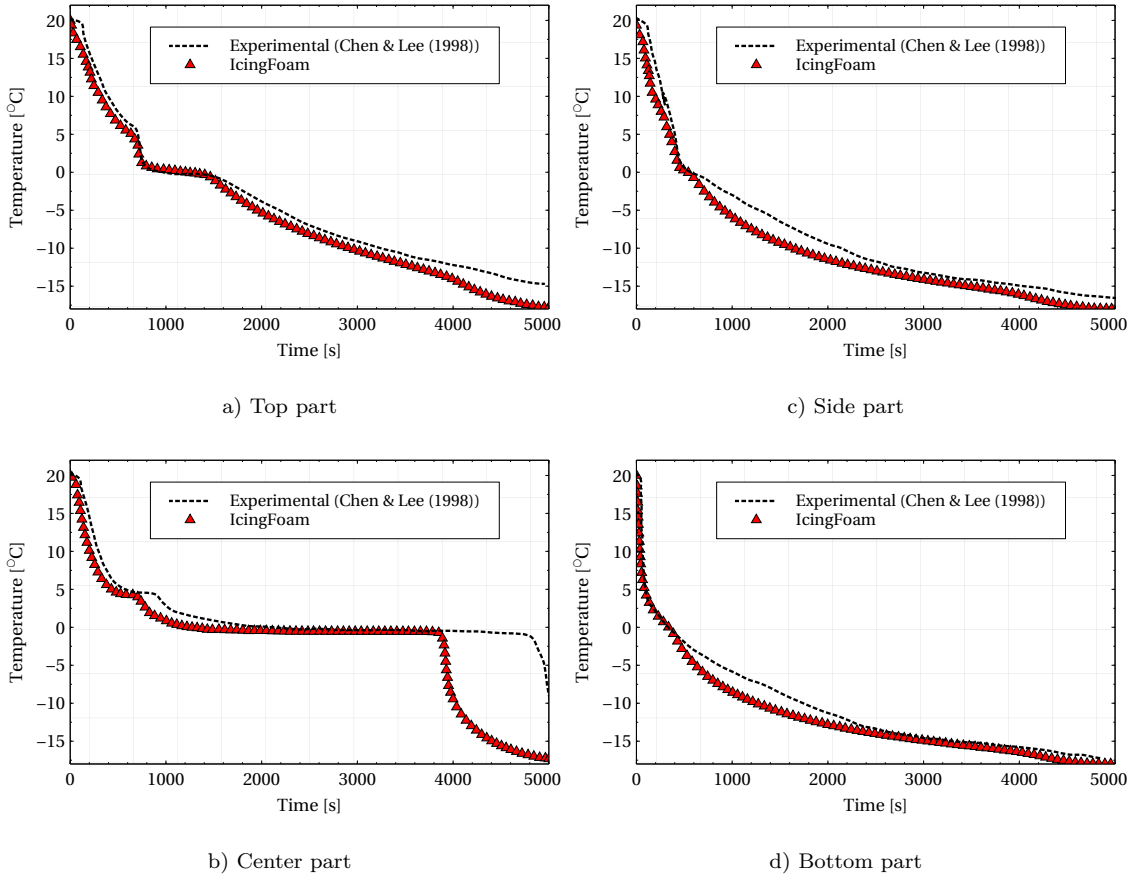

FIGURE 11.9: Numerical temperature profiles at different locations in the cylindrical enclosure with IcingFoam and comparison with experimental data - Wall temperature= -18^oC

Overall, a good agreement between the IcingFoam numerical results and the experimental data is obtained for each part of the cylindrical enclosure, up to 3900 s. Although a good agreement is still obtained on the side (Figure 11.9 c) and bottom (Figure 11.9 d) parts of the enclosure after 3900 s and acceptable on the top part (Figure 11.9 a), discrepancies are clearly visible in the central part of the computational domain (Figure 11.9 b). Three distinct regions can be defined in this central part: the convected heat transfer zone (Region 1) for $0\ s\ < t < 500\ s$, the mushy zone (Region 2) for $500\ s\ < t < 3900\ s$ and the solidification zone (Region 3) for $t > 3900\ s$.

The transition between Regions 1 and 2 is initiated numerically by the polynomial density variation of water plotted previously on Figure 10.1, where the inversion

point in density occurs for temperatures close to $T_i \simeq 5\ °C$. This phenomenon observed on Figure 11.9 b in experiments is well captured in the numerical simulations. After $t \simeq 1500\ s$, a plateau appears in the middle of the cylindrical enclosure for temperatures close to $T_i \simeq\ 0\ °C$, in Region 2. While the ice layer that grows slowly from the wall has not affected the temperature in the central part of the cylindrical enclosure yet, the latent heat prevents further cooling in this region.

When the ice layer gets to the center of the domain, the temperature suddenly falls down to reach the wall temperature $T_w = -18\ °C$ in Region 3. This sudden temperature fall happens in both experimental and numerical results, however at a different time. The transition from Region 2 to Region 3 is faster numerically and occurs at $t \simeq 3900\ s$ while it appears at $t \simeq 4800\ s$ in experiments.

These discrepancies can be explained by the different operating conditions used in Chen & Lee (1998) and in the present work. The test section from Chen & Lee (1998) contains a hollow copper cylinder with an inside diameter of 82.8 mm (test cell) and a thickness of 2.5 mm, filled with water at $T_i = 21°C$. On its external surface, alcohol (coolant fluid at $T_c = -18°C$ with a specifying cooling rate of $3.2°/min$) is flowing around the cylinder inside a cooling chamber. At $t = 0\ s$ the temperature of the surface of the inner diameter is therefore higher than the coolant fluid ($T_c = -18°C$) since the thickness of the cylinder reduces the cooling effect between the cooling chamber and the test cell. This set-up has been disregarded during numerical simulations and the test case was reduced to a cylindrical enclosure with no thickness, filled with water at $T_i = 21°C$ and cooled down using a wall temperature $T_w = -18°C$.

Due to the reasons mentioned above, the simulated temperature is slightly lower for each part of the cylindrical enclosure (Figures 11.9 a, b, c and d). The simulated ice layer therefore grows faster from the wall towards the center of the domain, leading to a sooner transition between Regions 2 and 3 (Figure 11.9 b). Figure 11.9 also shows that the temperature reaches $T_w = -18°C$ more quickly in simulations than in experiments. At the end of the experiment ($t = 5000\ s$), only the bottom part of the cylindrical domain has reached the critical wall temperature. The error between experimental and numerical results on the exact transition time between Regions 2 and 3 is evaluated around 15 %.

As the top, bottom and side parts are closer to the wall than the central part of the cylindrical enclosure, their temperature distribution is different and the mushy zone is not present. In these regions, two zones only are present: the convected heat transfer zone and the solidification zone.

To compare the evolution of temperature inside the domain during the freezing process, temperatures from all parts are plotted together on Figure 11.10.

Following the temperature decrease, the ice growth is expected to be the fastest at the bottom region of the cylindrical enclosure due to gravity and recirculation effects and the slowest in the middle part, this part being the most distant physical point from the cold wall. In the time interval corresponding to the plateau shown on Figure 11.10 (center part) between $1000\ s < t < 3900\ s$, the temperature remains quasi-constant with a value close to $T_i = 0\ °C$ before being affected by the expanding ice layer from the wall surface towards the center of the domain at $t \simeq 3900$s.

The increase of the ice layer inside the cylindrical enclosure is shown in Ta-

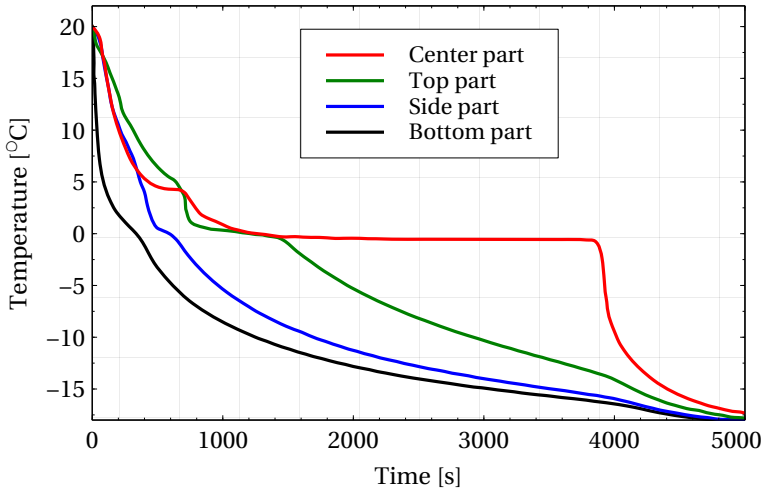

FIGURE 11.10: Temperature evolution, through time, at different locations inside the cylindrical enclosure

TABLE 11.6: Solidification rate process with IcingFoam for cylinders between $t = 300\ s$ and $t = 1000\ s$

$t = 300\ s$	$t = 500\ s$	$t = 750\ s$
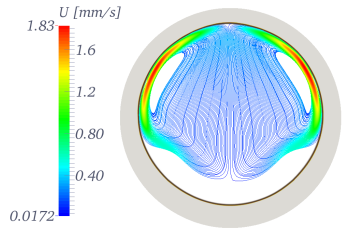	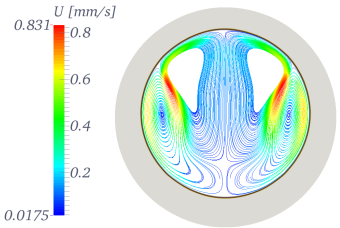	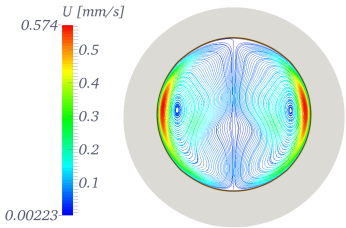
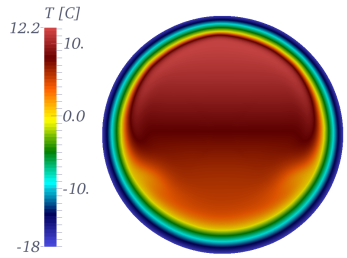	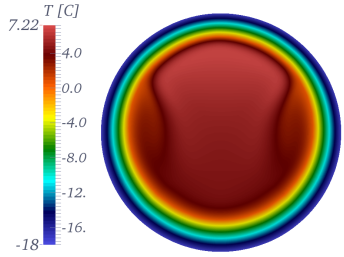	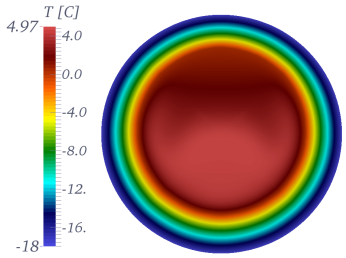
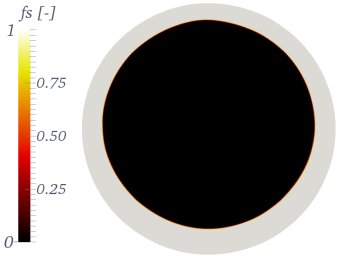	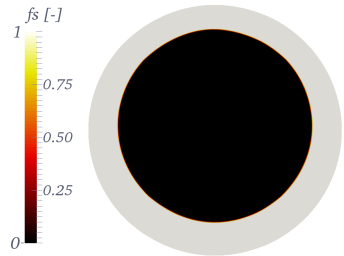	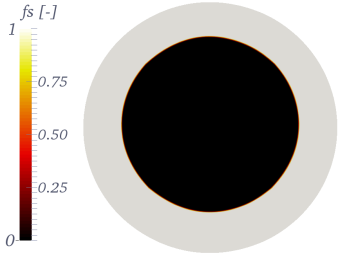

ble 11.6, which includes the ice volume fraction, velocity vectors and temperature distribution obtained after 300 s, 500 s and 750 s of simulation.

As previously discussed for the other cases, the flow consists in multiple recirculation regions, evolving through time. At $t = 300\ s$, two symmetric recirculations are present at the bottom of the cylindrical enclosure, see Table 11.6. Due to the recirculations, the temperature field presents a non-uniform structure and smaller values of temperature and velocity are present near the bottom. This is in agreement with the temperature profile obtained at $t = 300\ s$ on Figure 11.10.

After 500 s, recirculations are clearly visible, where the magnitude and direction of the velocity vectors influence directly the temperature distribution. Locally, due to the recirculations which warm the water up, temperatures are higher in the middle right and middle left parts of the cylindrical enclosure than near the ice layer on the right and left parts of the domain. The middle right and middle left parts correspond to the location of the highest velocity vectors seen on Table 11.6. The water is colder on the sides than in the middle or top regions, as shown in Figures 11.10 for $t = 500\ s$.

At $t = 750\ s$ in Table 11.6, recirculations have nearly vanished and a direction inversion is observed in the velocity vectors, due to previous collisions of the recirculation with the bottom ice layer. After reflecting on the bottom ice layer, velocities move up and follow the ice layer simultaneously on the right and left hand sides of the cylindrical enclosure. As the velocity magnitude in the top region of the domain is very low, the water temperature in this region is no longer warmed up by the fluctuating velocity and thus becomes slightly lower than in the middle part of the cylindrical enclosure.

The inversion point was also clearly visible in Figure 11.10, where the temperature at the top was higher than in the center for $t < 800\ s$ and became lower for $t > 800\ s$.

Similarly to the cavity case discussed in Section 11.2.3, a non-uniform ice-layer thickness appeared due to the water density variation. In addition, the decrease of temperature and growing of the ice were faster at the beginning of the simulations. To further describe the ice growth phenomenon, the solver has been extended to a Slurry-Mushy model. Results are presented in the following section.

Chapter 12

Solidification process with slurry-mushy regions modelling

The second solidification solver implemented in OpenFOAM is presented in this chapter. This solver is called IcingFoamSlurryMushy and will sometimes be referred to as IFSM. This model uses most of the findings presented in Chapter 11. However, the partially solidified region is approached differently here. The accuracy of the partially solidified region is further increased by distinguishing two states depending on a critical ice fraction value ($f_{s_{crit}}$). A distinction is made between the newly formed ice particles not interacting with each other (slurry region) and the mixture of compact ice and liquid (mushy region). As a result, the problem becomes a four phase study (i.e. liquid region, slurry region, mushy region and solid region). This solver is validated against the same cases as those presented in Chapter 11. Results showed good agreement with the previous solidification solver (IF) and explanations concerning the local discrepancies obtained between the two models are provided. In particular, velocity fields obtained with IFSM are slightly higher than those obtained with IF. As a result, small ice shape differences are obtained.

Contents

12.1 Solidification model with slurry-Mushy regions (IFSM) **117**
12.1.1 Energy conservation equation 118
12.1.2 Mass and momentum conservation equations 118
12.2 Numerical simulations of water freezing in cavities **121**
12.2.1 Model verification and comparisons with IcingFoam . . . 121
12.3 Numerical simulations of water freezing in cylinders **124**
12.3.1 Model verification and comparison with IcingFoam . . . 124

12.1 Solidification model with slurry-Mushy regions (IFSM)

For the Slurry-Mushy solidification model, the partially solidified region ($T_{sol} < T < T_{liq}$) is approached differently than with the IcingFoam solver described in the previous chapter. The present method aims at modeling the effects of solid ice particles on the flow, based on the amount of expected solid particles in a given region. An additional viscosity term is added to the flow when a solid volume fraction is below a critical threshold ($f_{s_{crit}}$) in the slurry region, where the recently formed solid grains do not interact with each other, see Figure 12.1. Above this critical threshold ($f_s > f_{s_{crit}}$), the additional viscosity is not sufficient to accurately model the sink of velocity caused by a compact solid layer. Thus, a transition is observed between the slurry and the mushy regions where additional source terms are added to the momentum equations.

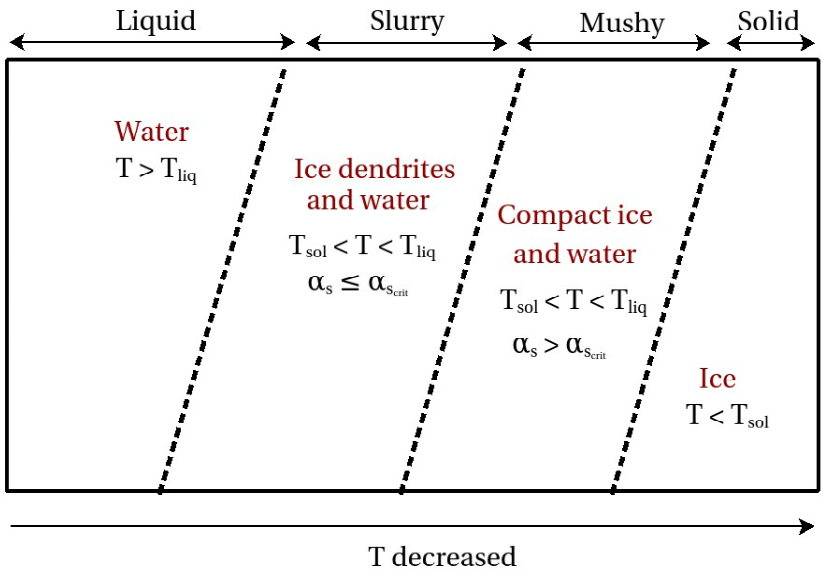

Figure 12.1: liquid, slurry, mushy, solid regions transitions

The slurry model implemented in OpenFOAM is based on the work from Metzner (1985) and the transition between slurry and mushy regions is performed through switching functions, similar to StarCCM+ (2012) model. The mushy model added to IcingFoamSlurryMushy is however based on Darcy's law and uses an error function for the water volume fraction along with the modified polynomial density variation $\rho(T)'$. StarCCM+ uses a linear function for the water volume fraction (Equation 11.4), the Carman-Kozeny model for the mushy region (Carman, 1937) and the Metzner model for the slurry region (Metzner, 1985).

12.1.1 Energy conservation equation

The energy equation used in the Slurry-Mushy solidification model is the same as in IcingFoam solver described previously in Section 11.

$$\frac{\partial \rho C_p T}{\partial t} + u\frac{\partial \rho C_p T}{\partial x} + v\frac{\partial \rho C_p T}{\partial y} = \lambda \Delta T + S_t \ . \tag{12.1}$$

Here again, the liquid fraction is computed with the error function in Equation 11.8. However, the expression of the dynamic viscosity in IcingFoam (Equation 11.10) is no longer used. Instead, the dynamic viscosity is now a function of the solid volume fraction f_s such as:

$$\mu = \begin{cases} \mu_\ell & f_s = 0 \Rightarrow \text{liquid region} \\ \mu_\ell \left(1 - \frac{F_s}{A}\right)^{-2} & f_s \leq f_{s_{crit}} \text{ and } f_s \neq 0 \Rightarrow \text{slurry region} \\ \mu_\ell \alpha_\ell + \mu_s \alpha_s & f_s > f_{s_{crit}} \text{ and } f_s \neq 1 \Rightarrow \text{mushy region} \\ \mu_s & f_s = 1 \Rightarrow \text{solid region} \end{cases} \tag{12.2}$$

The dynamic viscosity of the mixture μ is equal to the water dynamic viscosity μ_ℓ in the liquid region. In the slurry region, an additional viscosity term is added to the water dynamic viscosity μ_ℓ, following Metzner's model (Metzner, 1985):

$$\mu = \mu_\ell \ \left(1 - \frac{F_s}{A}\right)^{-2} \ . \tag{12.3}$$

In Equation 12.3, A stands for a constant which depends on the aspect ratio and surface roughness of the crystals formed in the slurry region. F_s is a switching function to activate or deactivate the slurry model. It is expressed as a function of both solid volume fraction (f_s) and critical volume fraction ($f_{s_{crit}}$) and with a switching constant (c_s) acting as an initiator for the function:

$$F_s = 0.5 - \frac{\arctan[c_s(f_s - f_{s_{crit}})]}{\pi} \ . \tag{12.4}$$

For a solid fraction above the critical threshold $f_{s_{crit}}$, both liquid and solid contributions are taken into account in the mixture viscosity μ of the mushy region. Finally, in the solid region ($f_s = 1$), only the ice viscosity is taken into account.

12.1.2 Mass and momentum conservation equations

The momentum equations have been modified for this solver:

$$\begin{aligned} &\frac{\partial u}{\partial x} + \frac{\partial v}{\partial y} = 0 \ , \\ &\frac{\partial \rho u}{\partial t} + u\frac{\partial \rho u}{\partial x} + v\frac{\partial \rho u}{\partial y} = -\frac{\partial p}{\partial x} + \mu \Delta u - S'_{m_x} \ , \\ &\frac{\partial \rho v}{\partial t} + u\frac{\partial \rho v}{\partial x} + v\frac{\partial \rho v}{\partial y} = -\frac{\partial p}{\partial y} + \mu \Delta v - g[\rho(T)' - \rho] - S'_{m_y} \ . \end{aligned} \tag{12.5}$$

The mushy source terms S'_{m_x} and S'_{m_y} are expressed through a switching function F_m. As for the slurry part, this switching function acts as a trigger for the initialization of the mushy model. The mushy switching function F_m is therefore expressed as the opposite of the slurry switching function F_s so that the transition between slurry and mushy zones is performed:

$$F_m = 1 - F_s = 0.5 + \frac{\arctan[c_s(f_s - f_{s_{crit}})]}{\pi} \ . \tag{12.6}$$

Based on the Carman-Kozeny mushy permeability model (Carman, 1937) and Darcy's law previously used in IcingFoam, the new mushy source terms S'_{m_x} and S'_{m_y} are computed as:

$$\begin{aligned} S'_{m_x} &= F_m D_c \frac{f_s^2}{\alpha_\ell^3 + \varepsilon} u \ , \\ S'_{m_y} &= F_m D_c \frac{f_s^2}{\alpha_\ell^3 + \varepsilon} v \ . \end{aligned} \tag{12.7}$$

The present solver can therefore handle solidification problems by solving governing equations differently in four distinct regions: i) Liquid, ii) Slurry, iii) Mushy and iv) Solid. This is summarized in Table 12.1. Figure 12.2 shows a plot of both slurry F_s and mushy switching functions F_m for an arbitrary critical solid fraction $f_{s_{crit}} = 0.35$.

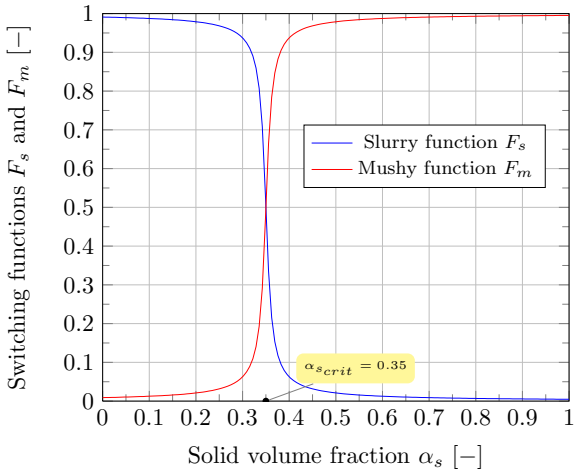

Figure 12.2: Slurry and mushy switching functions plot

Energy and momentum equations for the liquid water phase are solved in the fully liquid region ($T > T_{liq}$) using liquid viscosity (μ_ℓ), specific heat capacity (C_{p_ℓ}), thermal conductivity (λ_ℓ) and density ($\rho(T)$).

When phase change occurs ($T_{sol} < T < T_{liq}$), the flow is slowed down due to the appearance of solid ice particles. These particles do not interact with each other and they are associated with low volume fractions ($f_s \leq f_{s_{crit}}$).

TABLE 12.1: Governing equations of the IcingFoamSlurryMushy solver.

Regions	Temperature	f_s	$\rho(T)'$	C_p, λ, and μ	Energy, continuity and momentum equations
Liquid	$T > T_{liq}$	$f_s = 0$	$\rho(T)$	C_{p_ℓ} λ_ℓ μ_ℓ	$\frac{\partial \rho C_{p_\ell} T}{\partial t} + u\frac{\partial \rho C_{p_\ell} T}{\partial x} + v\frac{\partial \rho C_{p_\ell} T}{\partial y} = \Delta(\lambda_\ell T) + S_t$ $\frac{\partial u}{\partial x} + \frac{\partial v}{\partial y} = 0$ $\frac{\partial \rho u}{\partial t} + u\frac{\partial \rho u}{\partial x} + v\frac{\partial \rho u}{\partial y} = -\frac{\partial p}{\partial x} + \Delta(\mu_\ell u)$ $\frac{\partial \rho v}{\partial t} + u\frac{\partial \rho v}{\partial x} + v\frac{\partial \rho v}{\partial y} = -\frac{\partial p}{\partial y} + \Delta(\mu_\ell v) - g[\rho(T)' - \rho]$
Slurry	$T_{sol} < T < T_{liq}$	$f_s \leq f_{s_{crit}}$	$\rho(T)\alpha_\ell + \rho_s f_s$	$C_{p_\ell}\alpha_\ell + C_{p_s} f_s$ $\lambda_\ell \alpha_\ell + \lambda_s f_s$ $\mu_\ell \times \left(1 - \frac{F_s}{A}\right)^{-2}$	$\frac{\partial \rho C_p T}{\partial t} + u\frac{\partial \rho C_p T}{\partial x} + v\frac{\partial \rho C_p T}{\partial y} = \Delta(\lambda T) + S_t$ $\frac{\partial u}{\partial x} + \frac{\partial v}{\partial y} = 0$ $\frac{\partial \rho u}{\partial t} + u\frac{\partial \rho u}{\partial x} + v\frac{\partial \rho u}{\partial y} = -\frac{\partial p}{\partial x} + \Delta(\mu u) - F_m D_c \frac{f_s^2}{\alpha_\ell^3 + \varepsilon} u$ $\frac{\partial \rho v}{\partial t} + u\frac{\partial \rho v}{\partial x} + v\frac{\partial \rho v}{\partial y} = -\frac{\partial p}{\partial y} + \Delta(\mu v) - g[\rho(T)' - \rho] - F_m D_c \frac{f_s^2}{\alpha_\ell^3 + \varepsilon} v$
Mushy	$T_{sol} < T < T_{liq}$	$f_s > f_{s_{crit}}$	$\rho(T)\alpha_\ell + \rho_s f_s$	$C_{p_\ell}\alpha_\ell + C_{p_s} f_s$ $\lambda_\ell \alpha_\ell + \lambda_s f_s$ $\mu_\ell \alpha_\ell + \mu_s f_s$	$\frac{\partial \rho C_p T}{\partial t} + u\frac{\partial \rho C_p T}{\partial x} + v\frac{\partial \rho C_p T}{\partial y} = \Delta(\lambda T) + S_t$ $\frac{\partial u}{\partial x} + \frac{\partial v}{\partial y} = 0$ $\frac{\partial \rho u}{\partial t} + u\frac{\partial \rho u}{\partial x} + v\frac{\partial \rho u}{\partial y} = -\frac{\partial p}{\partial x} + \Delta(\mu u) - F_m D_c \frac{f_s^2}{\alpha_\ell^3 + \varepsilon} u$ $\frac{\partial \rho v}{\partial t} + u\frac{\partial \rho v}{\partial x} + v\frac{\partial \rho v}{\partial y} = -\frac{\partial p}{\partial y} + \Delta(\mu v) - g[\rho(T)' - \rho] - F_m D_c \frac{f_s^2}{\alpha_\ell^3 + \varepsilon} v$
Solid	$T < T_{sol}$	$f_s = 1$	ρ_s	C_{p_s} λ_s μ_s	$\frac{\partial \rho C_{p_s} T}{\partial t} + u\frac{\partial \rho C_{p_s} T}{\partial x} + v\frac{\partial \rho C_{p_s} T}{\partial y} = \Delta(\lambda_s T)$ $\frac{\partial u}{\partial x} + \frac{\partial v}{\partial y} = 0$ $\frac{\partial \rho u}{\partial t} + u\frac{\partial \rho u}{\partial x} + v\frac{\partial \rho u}{\partial y} = -\frac{\partial p}{\partial x} + \Delta(\mu_s u) - \frac{F_m D_c}{\varepsilon} u$ $\frac{\partial \rho v}{\partial t} + u\frac{\partial \rho v}{\partial x} + v\frac{\partial \rho v}{\partial y} = -\frac{\partial p}{\partial y} + \Delta(\mu_s v) - \frac{F_m D_c}{\varepsilon} v$

To model the sink of velocity caused by the interaction between the water and these solid ice components, an additional viscosity term provided by Equation 12.3 is added to the governing equations. In this slurry region, both liquid and solid contributions are computed for the resolution of the specific heat capacity, thermal conductivity and density. When the partially solidified layer becomes more compact ($f_s > f_{s_{crit}}$), the sink of velocity is not sufficient to predict the flow with accuracy. Therefore, a switching between the slurry ($f_s \leq f_{s_{crit}}$) and the mushy ($f_s > f_{scrit}$) region is required. This is achieved by adding a source term in the momentum equation. In the mushy model (Carman, 1937), viscosity, density, specific heat capacity and thermal conductivity are computed based on both liquid and solid contributions.

Finally, in the solid region ($T < T_{sol}$), the mushy source terms tends to infinity so that no water velocity is computed in the iced region. Therefore, only solid specific heat capacity, density, thermal conductivity and viscosity are used for the governing equations in the fully iced region.

12.2 Numerical simulations of water freezing in cavities

12.2.1 Model verification and comparisons with IcingFoam

The differentially heated cavity test case previously discussed in Section 11.2.3 with IcingFoam, is used here for the validation of the IcingFoamSlurryMushy solver.

Table 12.2: Water properties for the solidification study in IcingFoamSlurryMushy

Water properties	Symbol	Values	Units
Crystal constant	A	0.3	–
Switching constant	c_s	100	–
Darcy constant	D_c	10^8	$kg.m^{-3}.s^{-1}$
Ice critical volume fraction	$f_{s_{crit}}$	0.27	–

Although same input parameters have been used in both studies, additional terms from StarCCM+ (2012) have been necessary for the calibration of the slurry and mushy regions in the IcingFoamSlurryMushy solver, see Table 12.2. Figure 12.3 shows the results obtained with the IcingFoamSlurryMushy solver. They are compared to the previous results obtained with IcingFoam and to those obtained with the Slurry-Mushy solidification model available in StarCCM+. It appears clearly that additional terms for the treatment of the partially solidified region induce differences in the behaviour of the flow, even if a similar flow structure is observed between the two solvers implemented in OpenFOAM. Larger discrepancies between IcingFoam and IcingFoamSlurryMushy are observed for the four velocity fields due to differences in the momentum equations.

A different velocity magnitude induces differences in the energy equation which explains the discrepancies in the temperature profiles between IcingFoam and Icing-

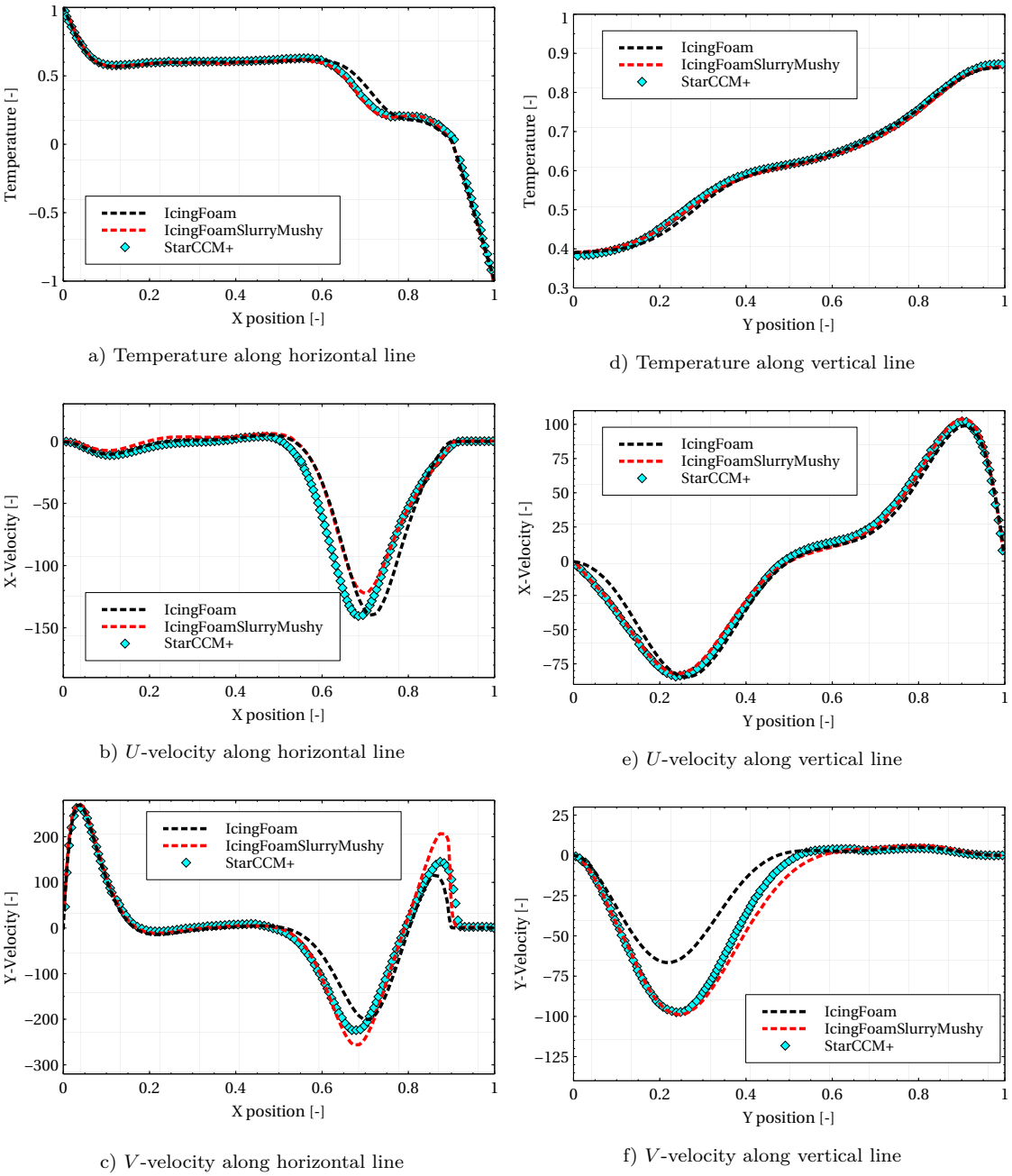

a) Temperature along horizontal line

d) Temperature along vertical line

b) U-velocity along horizontal line

e) U-velocity along vertical line

c) V-velocity along horizontal line

f) V-velocity along vertical line

FIGURE 12.3: IcingFoamSlurryMushy numerical results - Temperature and velocity fields along horizontal and vertical line

FoamSlurryMushy. Results obtained with IcingFoamSlurryMushy, however, show a good agreement with StarCCM+. Maximum local discrepancies are fairly low, 7 % for the U-velocity along the horizontal line (Figure 12.3b) and 15 % for the V-velocity along the horizontal line (Figure 12.3c). The present solver is therefore able to produce similar results to those generated with the StarCCM+ solver for slurry-mushy solidification problems.

Finally, Figure 12.4 gives the values and behaviours of both slurry (F_s) and mushy (F_m) switching functions. As can be seen, $F_s \sim 1$ in the fully liquid zone (red color in Figure 12.4a) and is close to 0 in the ice zone (blue color in Fig-

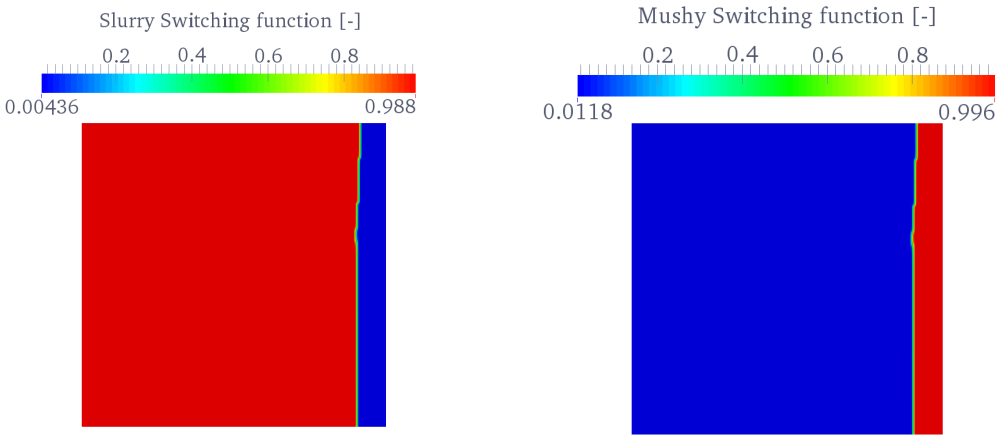

a) Slurry switching Function (F_s)

b) Mushy switching Function (F_m)

Figure 12.4: Slurry and Mushy switching functions behaviour during water solidification in cavity at $t = 100\ s$

ure 12.4a). The opposite behaviour is observed for the mushy switching function F_m. Inside the partially solidified zone, Figure 12.4 shows that both functions take values between 0 and 1. Therefore, the present solver (i.e. IcingFoamSlurryMushy) computes correctly the effects of both slurry and mushy regions.

Tables 12.3 and 12.4 present a comparison between IcingFoam and IcingFoam-SlurryMushy results at times $t = 100\ s$ and $t = 1500\ s$ respectively. In Tables 12.3 and 12.4, the abbrevations IF and IFSM stand for IcingFoam and IcingFoamSlurry-Mushy solvers respectively.

Table 12.3: Comparisons between IF and IFSM for cavity at $t = 100\ s$

Solver	Velocity	Temperature	Ice fraction
IF	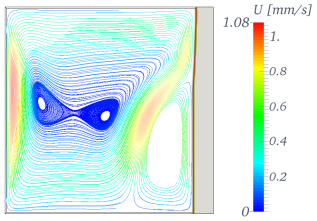	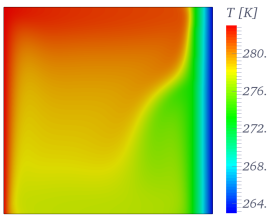	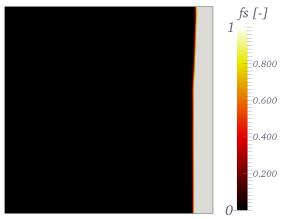
IFSM	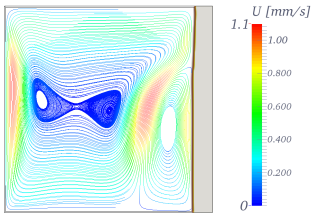	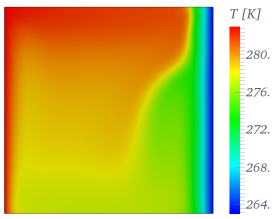	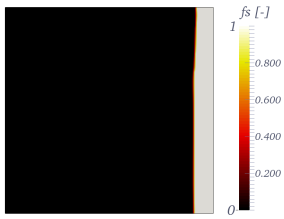

Table 12.3 shows that results obtained from the two solvers are extremely close. The only noticeable discrepancies are visible for the magnitude of the velocities (i.e. 1.08 $mm.s^{-1}$ for IcingFoam and 1.10 $mm.s^{-1}$ for IcingFoamSlurryMushy). The second solver therefore produces slightly higher velocities when compared to IcingFoam.

Table 12.4: Comparisons between IF and IFSM for cavity at $t = 1500\ s$

Solver	Velocity	Temperature	Ice fraction
IF	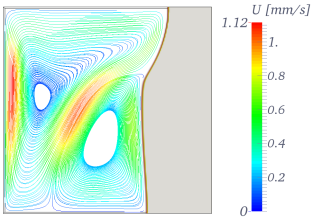	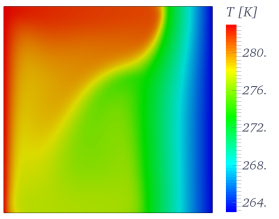	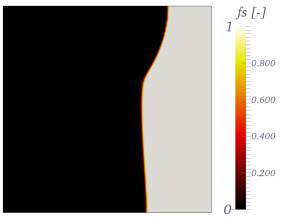
IFSM	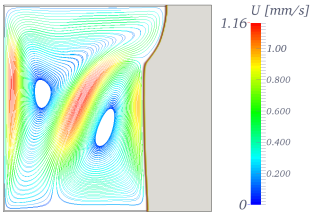	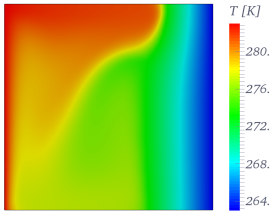	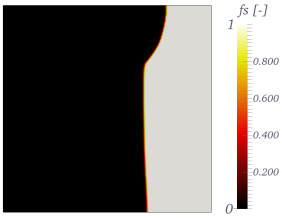

This statement is also valid at a later time ($t = 1500\ s$) as shown in Table 12.4. Discrepancies for the ice-layer shape are also visible at that time. It seems that, at the top region, the water carves deeper into the ice-layer for IcingFoamSlurryMushy than for IcingFoam. This is correlated to the previous observation. Higher velocity magnitude vectors warm up the water in the vicinity of the ice-layer, therefore leading to a more shallow belly-shape for IcingFoamSlurryMushy. Results from both solvers remain close. It is shown that the slurry region has an impact on the ice growth and the fluid motion inside the cavity. The validation of IcingFoamSlurryMushy is extended further to investigate the effects of the added slurry region on the cylindrical enclosure test case previously discussed in Section 11.3.3.

12.3 Numerical simulations of water freezing in cylinders

12.3.1 Model verification and comparison with IcingFoam

Same conditions as those described in Section 11.3.3 are used here for the validation of the Slurry-Mushy solidification solver. As for the differentially heated cavity, terms have been added for the calibration of both slurry and mushy regions when dealing with the IcingFoamSlurryMushy model. They are those listed in Table 12.2.

Results obtained with this solver are shown in Figure 12.5. They are compared with those obtained with IcingFoam and with experimental data from Chen & Lee (1998).

The IcingFoamSlurryMushy results are in good agreement with the experimental data. As previously discussed for IcingFoam in Section 11.3.3, differences are noticeable in the central part of the cylindrical enclosure after $t \simeq 3800$s, see Figure 12.5b. The difference of initial operating conditions for the wall tempera-

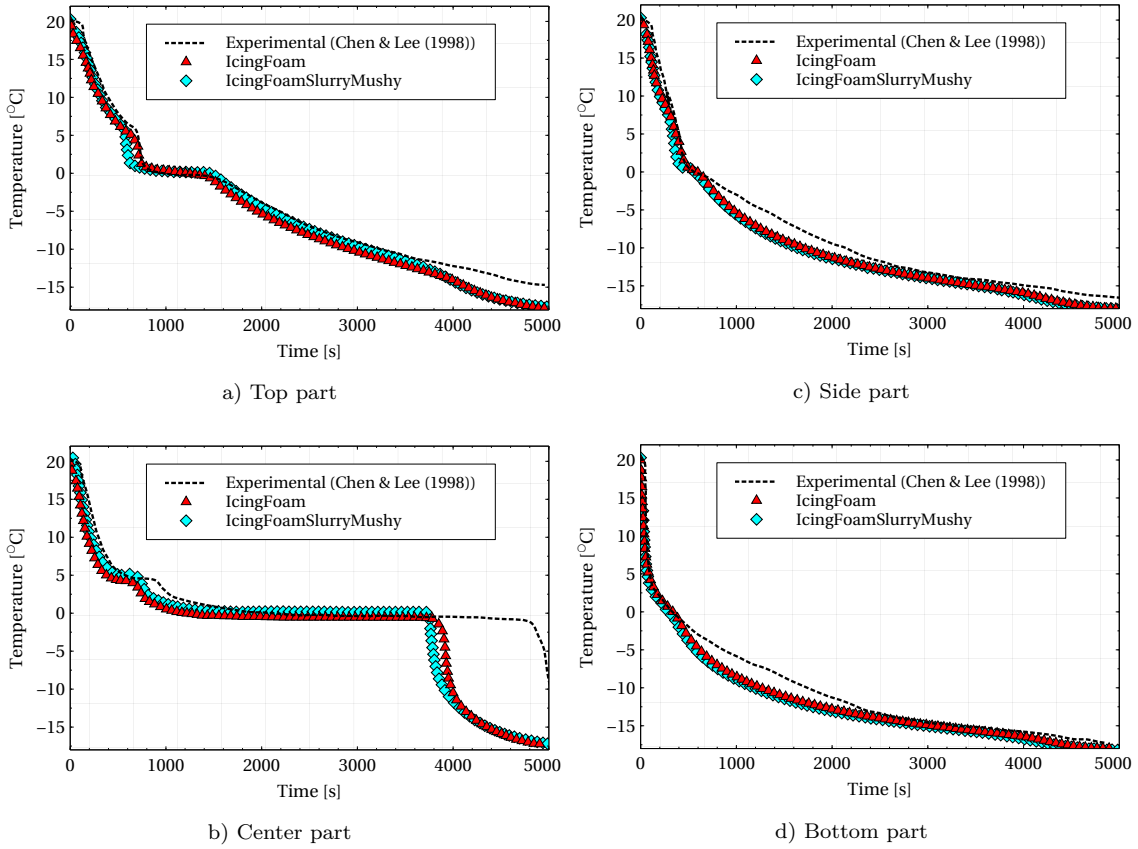

Figure 12.5: Numerical temperature profiles at the top, center, side and bottom parts of the cylindrical enclosure with IcingFoamSlurryMushy and comparison with experimental data - Wall temperature= -18^oC

ture between experimental and numerical studies can again explain the differences obtained here.

Slight discrepancies are noticeable between IcingFoam and IcingFoamSlurryMushy results shown on Figure 12.5. As the partially solidified region ($0 < \alpha_s < 1$) is treated differently, discrepancies are present between IcingFoam and IcingFoamSlurryMushy results. The ice shape is therefore slightly different during the solidification process. As discussed previously (Section 11.2.3), small changes in the ice layer structure imply that velocities behave slightly differently after colliding onto it (see Figures 12.3 and Table 12.5). As a result, temperature evolutions are slightly different between the two solvers, see Figures 12.5 and Table 12.6. It appears that the addition of a viscosity term in the slurry region generates an under-prediction of the overall temperature. However, as there is only little difference in the results when using any of these solvers, they are therefore equally effective for this type of study. The use of variable properties for the heat capacity and the thermal conductivity of water (similarly to the approach used in this work for density and viscosity properties) might improve the results further.

To explain more thoroughly the sudden temperature decrease obtained in the central part of the domain (Figure 12.5 b) which appears earlier numerically, two additional simulations have been performed with initial wall temperatures set to

TABLE 12.5: Comparisons between velocity and ice layer profiles obtained with IF and IFSM

Time	IcingFoam	IcingFoamSlurryMushy
$t = 500\ s$	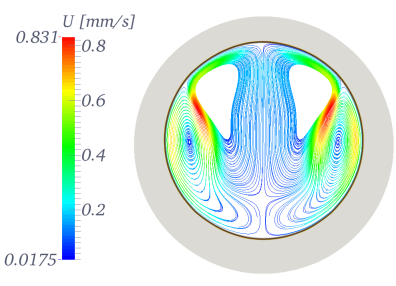	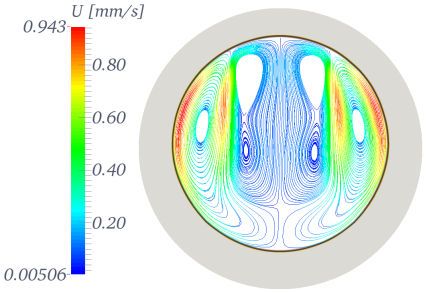
$t = 750\ s$	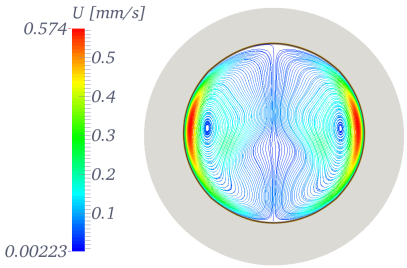	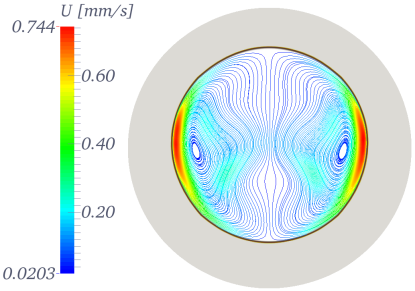

TABLE 12.6: Comparisons between temperature profiles obtained with IF and IFSM

Time	IcingFoam	IcingFoamSlurryMushy
$t = 500\ s$	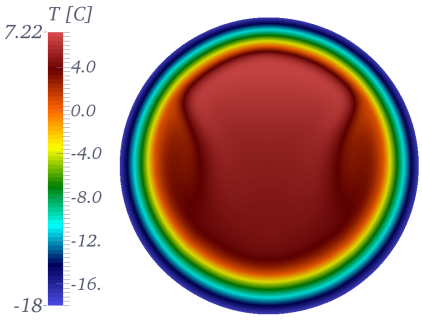	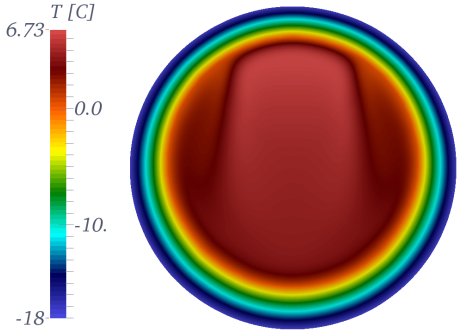
$t = 750\ s$	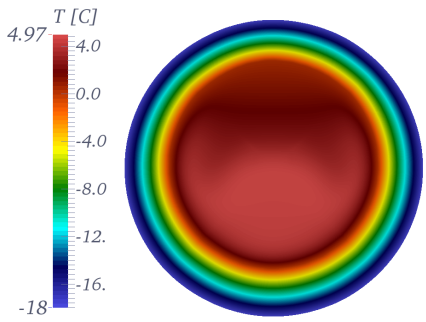	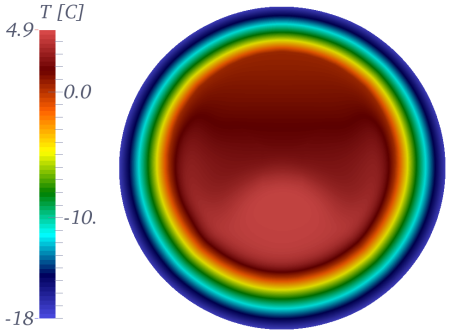

$-16\ ^\circ C$ and $-14\ ^\circ C$. The objective was to establish the influence of the initial wall temperature on the time required to get full solidification inside the cylindrical enclosure. Figure 12.6 shows the corresponding final temperatures.

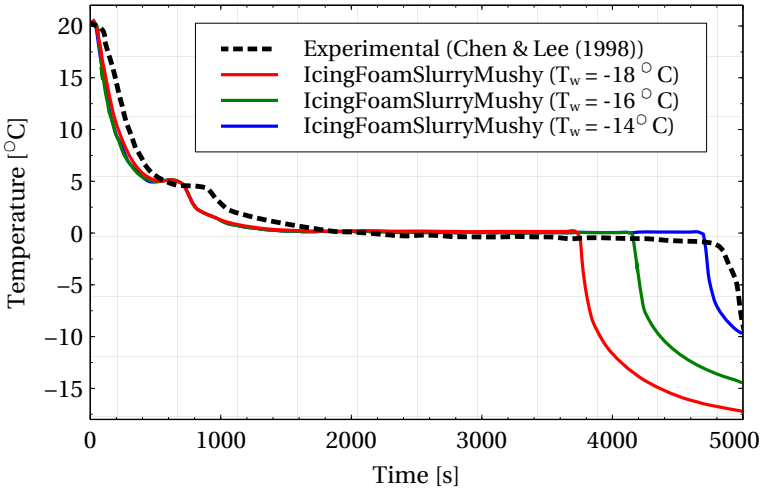

Figure 12.6: Numerical temperature profiles at the center of the cylindrical enclosure with IcingFoamSlurryMushy for different wall temperatures and comparison with experiments

As can be seen, if the wall temperature is increased, the time for complete solidification inside the cylindrical enclosure increases too. This confirms the previous statements, i.e. the thickness of the cylinder and the thermal conductivity of the wall structure influence strongly the internal temperature of the domain and the time required to reach full solidification. This has also been discussed in Ismail et al. (2003). Additional studies would however be useful to investigate fully the effects of the thermal conductivity of the wall structure.

Chapter 13

Conclusions and discussions

The natural convection of water has been investigated inside cavities. For this task, a modified version of BuoyantBoussinesqPimpleFoam (convection solver using a standard Boussinesq approximation developed by OpenFOAM) has been designed. The new solver which has been developed for this purpose uses a modified Boussinesq approximation, where the density related terms are expressed as a fourth order polynomial function, correlated with experimental data. It is shown that this model behaves extremely well when compared to experimental measurements for water in natural convection inside cavities. The most important finding is related to the fluid properties to be used in natural convection. In particular, a small density change (of the order of 0.2 $kg.m^{-3}$ in this case) engendered an entirely different flow pattern. For example, when analysing the flow structures obtained with BBPF and CF after 1500 s of simulations, only one convection current was visible for the first solver whereas two clearly discernible counteracting circulations were obtained for the later. The two competing circulations were also observed in the experimental work. As a result, the convection solver developed in this PhD gives more accurate results for water in natural convection inside cavities than the solver distributed by OpenFOAM. Obtaining a good steady-state solution of natural convection is very important to further investigate solidification processes accurately. When compared to other numerical work, this new solver behaves fairly well, with maximum local discrepancies being evaluated below 15% in the worst case scenario.

Water solidification has then been investigated with an enthalpy-porosity based solidification model also implemented in OpenFOAM. The natural convection solution is used as a starting point for simulating the solidification process. This solidification solver uses several techniques to achieve very accurate results when compared to other numerical and experimental data. Among them, a polynomial function has been used for the density of the fluid and an error function has been implemented to speed-up computation and correctly approach the transition between solid and liquid. Finally, the partially solidified region is treated as a mushy-region, assumed to behave as a porous media. Additional modelling effort was necessary to take into account phase changes phenomena in the momentum equations. This has been accomplished using Darcy's law. The present solver is found to behave very well for the water freezing study inside cavities. The maximal discrepancies ob-

tained are below 10 % when compared to numerical results from commercial codes. A good agreement is also found for the details of the ice-layer growth and shape between simulations and experiments. However, at that stage, the model could not be validated fully due to lack of experimental data for the squared cavity. The solver has therefore been tested further for ice formation in a cylindrical enclosure and successfully compared with experiments. Although an overall good agreement has been obtained, the largest discrepancies (around 15 %) were observed for the temperature evolution in the central part of the computational domain. The different operating conditions between experiments and numerical simulations have explained these discrepancies.

The enthalpy-porosity based solidification solver has finally been enhanced with a new slurry-mushy model where the partially solidified region has been decomposed in two regions, depending on the volume fraction of ice. This solver showed good agreement with results from StarCCM+, based on a different slurry-mushy model, and with experimental data in a cylindrical enclosure. Slight differences were present between results from both solidification solvers implemented in OpenFOAM. For the slurry-mushy based model, the additional viscosity terms generated an under-prediction of the overall temperature which produced larger errors on time for region transitions. However, results were still acceptable with 17 % maximum error when compared to experiments for the cylindrical enclosure case. The reason for such large discrepancies are those stated previously, i.e. the thickness of the cylindrical enclosure and its associated thermal conductivity which are different in experiments and simulations. Differences concerning velocity magnitudes predictions were also noticed between IcingFoamSlurryMushy and IcingFoam. The IcingFoamSlurryMushy solver starts its procedure by increasing slightly the viscosity in the newly solidified region. The viscosity keeps increasing exponentially as the ice layer becomes more compact and where the ice particles starts agglomerating. As a result, the velocity sink in the partially solidified region is less sudden than for IcingFoam where a maximum viscosity is automatically set as soon as the ice starts forming in the domain. This explains why velocity magnitudes obtained with IcingFoamSlurryMushy are slightly larger than those produced by IcingFoam. One consequence of these effects is that different ice shapes are obtained between the two models.

This work has permitted to identify that the addition of a slurry region during the computation is extremely important for an accurate ice growth rate prediction. Overall, both solidification solvers have provided good agreement with experiments and commercial code solutions. It is therefore advised to use IF rather than IFSM for icing simulations as it is slightly faster. Additional investigation may prove that the addition of the slurry regions might be mandatory for specific icing study cases however. The variable density of the water phase has proven to be accurate and to efficiently model the behaviour observed in experiments. Additional studies would be useful to investigate the effects from different slurry models and the critical solid fraction value on the flow in both the enthalpy-porosity and the slurry-mushy based models. Finally, similarly to the approach used here for density and viscosity of

water, variable thermal conductivity and heat capacity could be implemented in the solvers. It is expected that this approach will improve the results further. This statement is addressed in the next part of this thesis (Part IV) where, based on all the findings discussed here, a new solidification solver for multi-fluid application is implemented in OpenFOAM. This new solver could be used for a coupling with a population balance model.

Part of the work presented in this Part (Part III) has been published in Bourdillon et al. (2015). It has also been extended to investigate the modelling of macroscopic solidification of binary mixtures. The IFSM solver has been used as a starting point for this model and a manuscript has been submitted to a journal. On a final note, both solvers presented here (IF and IFSM), permit to simulate the solidification process quickly in OpenFOAM. It has been built in such a manner that the difficulty to implement different temperature dependent properties (for other fluids than water as an example) is reduced. Therefore, these solvers can be applied for a future coupling with population balance modelling and for a wide range of fluids and flow conditions. Further investigations on this statement are performed in the Part IV of this PhD.

Nomenclature

Dimensionless numbers

CFL	Courant, Friedrichs and Lewy condition	$[-]$
erf	Error function	$[-]$
P_r	Prandtl number	$[-]$
R_a	Rayleigh number	$[-]$

Greek letters

α	Volume fraction	$[-]$
β	Thermal expansion coefficient	$[K^{-1}]$
Δt	Time step	$[s]$
γ	Thermal diffusivity	$[m^2.s^{-1}]$
λ	Thermal conductivity	$[W.m^{-1}.K^{-1}]$
μ	Dynamic viscosity	$[kg.m^{-1}.s^{-1}]$
ν	Kinematic viscosity	$[m^2.s^{-1}]$
$\rho(T)$	Polynomial density variation	$[kg.m^{-3}]$
ρ	Density	$[kg.m^{-3}]$
ε	Small constant	$[-]$

Roman letters

ℓ	Length	$[mm]$
A	Constant	$[-]$
C_p	Specific heat capacity	$[J.kg^{-1}.K^{-1}]$
C_s	Switching constant	$[-]$
d	Diameter	$[mm]$
D'_c	Darcy constant in slurry model	$[kg.m^{-3}.s^{-1}]$
D_c	Darcy constant	$[kg.m^{-3}.s^{-1}]$
E	Internal energy a system	$[J]$
f_s	Ice fraction	$[-]$
F_m	Mushy switching function	$[-]$
F_s	Slurry switching function	$[-]$
g	Gravitational acceleration value	$[m.s^{-2}]$

H	Enthalpy	$[J]$
h	Specific sensible enthalpy	$[J]$
L	Latent heat of fusion	$[J.kg^{-1}]$
m	Mass	$[kg]$
p	Pressure	$[Pa]$
Q	Heat	$[kJ]$
T	Temperature	$[K, ^\circ C]$
t	Time	$[s]$
t_h	Thickness	$[mm]$
T_{liq}	Liquidus temperature	$[K]$
T_{sol}	Solidus temperature	$[K]$
u	x-velocity	$[m.s^{-1}]$
v	y-velocity	$[m.s^{-1}]$
W	Work of a system	$[J]$
x	Horizontal coordinate	$[-]$
y	Vertical coordinate	$[-]$

Subscripts

ℓ	Liquid phase	$[-]$
$\tilde{}$	Dimensionless values	$[-]$
c	Coolant	$[-]$
$crit$	Critical value	$[-]$
i	Internal field	$[-]$
m	Maximum value	$[-]$
r	Reference value	$[-]$
s	Solid phase	$[-]$
w	Wall	$[-]$
w_l	Left wall	$[-]$
w_r	Right wall	$[-]$

Source terms

S'_{m_x}	x-source term in slurry model	$[kg.m^{-3}.s^{-1}]$
S'_{m_y}	y-source term in slurry model	$[kg.m^{-3}.s^{-1}]$
S_{m_x}	x-source term in mushy model	$[kg.m^{-3}.s^{-1}]$
S_{m_y}	y-source term in mushy model	$[kg.m^{-3}.s^{-1}]$
S_t	Source term in energy equation	$[J.m^{-3}.s^{-1}]$

Part IV

Towards a possible coupling between population balance and solidification models

14 Summary 134

15 Introduction 135

16 Solidification process for multiphase flows 136
16.1 Multiphase solidification solver . . . 137
16.2 Natural convection process modelling . . . 142
16.3 Solidification process modelling . . . 143

17 Population balance modelling for multiphase flow 148
17.1 Continuity, momentum and energy equations . . . 149
17.2 Break-up modelling . . . 150
17.3 Coalescence modelling . . . 151
17.4 Interfacial forces . . . 152
17.5 Preliminary results . . . 154

18 Conclusions and discussions 157

Nomenclature 158

Chapter 14

Summary

This part exposes numerical simulations and theoretical studies towards a possible coupling between population balance and solidification solvers. Chapter 15 briefly presents the scope of this part along with the positionning taken for this PhD. Several new elements extracted from a literature review are also provided. The main focus of this part is to present recent development in this PhD concerning a multi-fluid solidification solver and a population balance model both developped in OpenFOAM. Among interesting findings, it is shown that the developed multi-fluid solidification solver gives good results when compared with experimental measurements and numerical studies. The numerical results and the solver definition are detailed in Chapter 16. Additionally, the population balance model, developed based on a standard method of moment and from the findings extracted from Part II is derived and, in particular, implementation and development methods are deeply explained in Chapter 17. This solver is currently undergoing additional development and improvement as explained in the future work section of this thesis. Overall, the main idea of the work flow for these solvers is to run the PBE solver and from a steady-state, extract the sensible parameters (such as volume fraction, temperature and velocity fields) and use them as an initial boundary condition for the multi-fluid solidification solver. This will ensure a coupling between the two solvers since the effect of a PBM approach could be taken into account in the solidification process. This part is shorter than the previous ones. It can be seen as an expanded future work description, based on the comments and findings detailed in the previous two parts of this thesis.

Chapter 15

Introduction

The first Chapter of this part focuses on the development of a multi-fluid solidification solver in OpenFOAM within an Eulerian-Eulerian framework. Such a model remains extremely new and only few similar studies have been performed over the last few years. Among them, Lei et al. (2009) developed a model for solidification and collision-growth in slab continuous casting caster and Vakhrushev et al. (2013) developed a Lagrangian model, based on the DPM theory for bubbles motion and coupled it with a solidification model in OpenFoam. However, no model able to compute phase change processes from liquid to solid with the help of a PBM approach hasn't, from the author's knowledge, been implemented yet in an Eulerian-Eulerian framework. Moreover, models based on a particle distribution to simulate change of size of the liquid phase, and solidification models, are not available yet, within OpenFOAM. As a result, the work presented in this section constitutes a novelty in the field of solidification modelling. The solver developed here is based on the previous findings detailed in Part III. The previous solvers have been enhanced and reformulated to handle solidification where more than one phase is present. A novel formulation for the phase change computation as a function of temperature has been designed. A heat transfer correlation has been used in order to model the exchange of heat between dispersed and continuous phases based on the diameter of the phase and variable properties for thermal conductivity, heat capacity and viscosity have been created. It is shown that the current solver provides accurate results when compared to experimental data.

Secondly, a population balance solver has been implemented in OpenFOAM, which takes into account both break-up and coalescence events, based on the PBM model used in Part II. The model of Lo & Rao (2007), described in the previous section of this thesis has been reformulated to ensure a possible implementation in OpenFOAM and to simplify its use. Futhermore, the break-up and coalescence terms computation has been redesigned as possible ways to enhance the current model have been discovered in the previous parts of this thesis. This new PBM model is presented in this section. The solver is curently only partially validated and additional ways to validate it further are discussed in the future work section.

Chapter 16

Solidification process for multiphase flows

Based on the findings of the single-phase solidification part (Part III), a multiphase solidification solver is created. The aim is to compute phase change processes (solidification) of a dispersed water phase, separated or mixed with a continuous oil phase. This constitutes a first step toward a coupling between population balance type models and solidification processes. The solver and the validation cases are presented in this chapter. It is shown that the current solver gives good agreement when compared to both experimental and numerical results from the literature.

16.1 Multiphase solidification solver

Two solvers have been created so far. These solvers can handle solidification problems where more than one fluid is present. The first one is suitable for solidification problems where a clear interface is present between the two fluids whereas the second one permits to compute phase change processes inside a mixture of two fluids where only one can solidify. For the single-fluid solver presented previously in this thesis, water only was considered in the domain. In order to increase the range of applicability of these solvers a multi fluid solidification solver has been designed. This solver can handle solidification problems of water in a domain containing water and oil. The oil phase is considered to be the continuous phase and is not supposed to solidify in the scope of this work. The water phase however, is considered as the dispersed phase and can be subjected to solidification. This water phase is considered as drops or a fully-liquid phase. This solver handles water solidification in a multifluid domain in 3D or 2D, transient and for laminar or turbulent flows. The phase change process has been handled in a similar manner as the single-fluid solvers and its effect is taken into account in both energy and momentum equations through a mushy region for the dispersed water phase.

16.1.1 Temperature dependent fluid properties

The fluid properties in the liquid zone are all computed as a function of the temperature. This is an improvement compared to the single fluid solver where only the density was computed as a function of the temperature. The water density function, already used in Sections 11 and 12 is computed from (Kohlrausch, 1968). The remaining properties evolution (heat capacity, thermal conductivity and viscosity) are extrapolated from (Reizes et al., 1985). Equations 16.1 give the fluid properties evolution as a function of temperature. The variable density polynomial function is given here in Kelvin, to ensure consistency with the remaining properties.

$$\begin{aligned}
\rho(T) &= \rho_0 + \rho_1 T + \rho_2 T^2 + \rho_3 T^3 + \rho_4 T^4 \ [kg/m^3] \ , \\
C_p(T) &= C_{p_0} + C_{p_1} T + C_{p_2} T^2 + C_{p_3} T^3 \ [J/kg.K] \ , \\
\lambda(T) &= \lambda_0 + \lambda_1 T \ [W/m.K] \ , \\
\mu(T) &= \mu_0 \exp\left[\mu_1 \left(\frac{1}{T^3} - \frac{1}{273.15^3}\right)\right] \ [kg/m.s] \ ,
\end{aligned} \tag{16.1}$$

Table 16.1 gives the values of the corresponding coefficients. The variable density polynomial coefficients are here different from (Kohlrausch, 1968) since the temperature is given in Kelvin, to ensure consistency with the remaining properties.

Figure 16.1 shows the coresponding values for each properties between $0°C$ $(273.15K)$ and $20°C$ $(293.15\ K)$. In the solid zone, the ice properties are used.

Therefore, the total fluid properties can be defined as a sum between liquid water, solid water (i.e. ice) and oil properties. Oil properties can, if required by the user, be defined through polynomial functions depending on the temperature values, similarly to the liquid water properties. The ice properties, are however, considered

TABLE 16.1: Coefficients for the variable properties functions.

Fluid property	Function	Coefficients
Density	$\rho(T[K])$	$\rho_0 = -5162.2312187478$
		$\rho_1 = 78.5943390276$
		$\rho_2 = -0.3773476496$
		$\rho_3 = 8.113002.10^{-4}$
		$\rho_4 = -6.62139792627547.10^{-7}$
Heat capacity	$C_p(T[K])$	$C_{p_0} = 8958.66$
		$C_{p_1} = -40.534$
		$C_{p_2} = 0.11234$
		$C_{p_3} = -0.000101379$
Thermal conductivity	$\lambda(T[K])$	$\lambda_0 = 0.566$
		$\lambda_1 = 0.000566$
Viscosity	$\mu(T[K])$	$\mu_0 = 1.79 \times 10^{-3}$
		$\mu_1 = 6.18 \times 10^{7}$

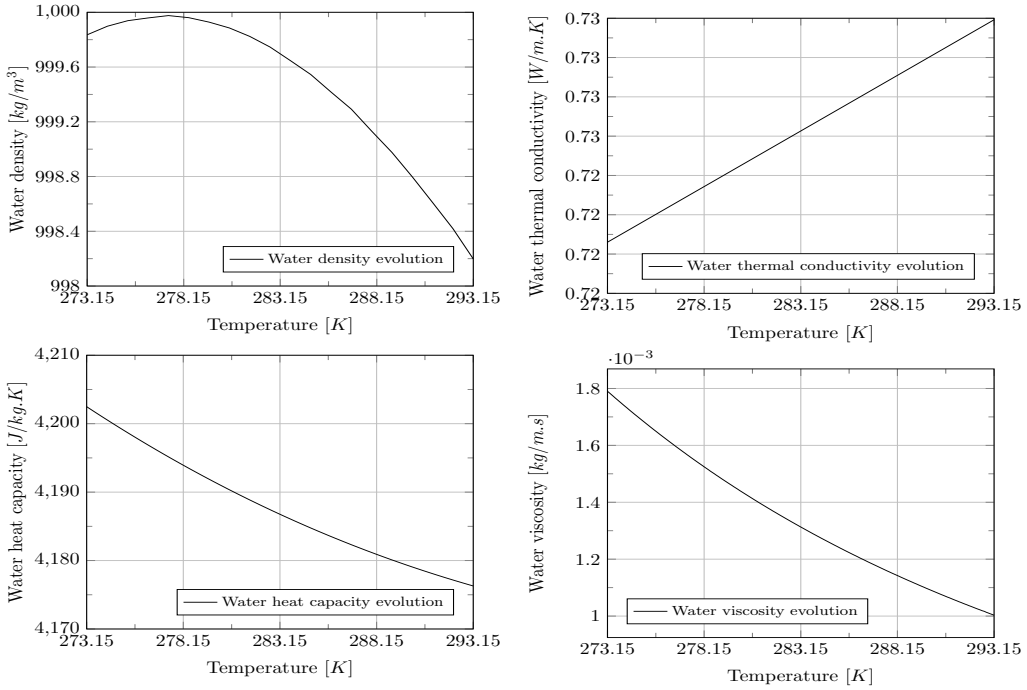

FIGURE 16.1: Variable water properties values between $0°C$ and $20°C$

constant. Equation 16.3 gives the formulation of how the total fluid properties values are computed in each computational cell.

$$\begin{aligned}
\rho &= \alpha_\ell \rho(T) + \alpha_s \rho_s + \alpha_{oil} \rho_{oil}, \\
C_p &= \alpha_\ell C_p(T) + \alpha_s C_{p_s} + \alpha_{oil} C_{p_{oil}}, \\
\lambda &= \alpha_\ell \lambda(T) + \alpha_s \lambda_s + \alpha_{oil} \lambda_{oil}, \\
\mu &= \alpha_\ell \mu(T) + \alpha_s \mu_s + \alpha_{oil} \mu_{oil} \ ,
\end{aligned} \tag{16.2}$$

The volume fraction of water is computed slightly differently from the single phase solidification solver. The same error function is used as before but it is modified to account for the fact that more than one phase is present in the domain. The function used to compute the volume fraction of water is therefore:

$$\begin{aligned}
\alpha_\ell &= \alpha_w \times erf_{singlefluid} \ , \\
\alpha_\ell &= \alpha_w \times \left[0.5 + 0.5 \ erf \left(4 \ \frac{T - \frac{T_{liq}+T_{sol}}{2}}{T_{liq} - T_{sol} + \varepsilon} \right) \right] \ , \\
\alpha_s &= \alpha_w - \alpha_\ell \ ,
\end{aligned} \tag{16.3}$$

The error function is multiplied by the volume fraction of water present in a cell. This permits to compute the correct amount of liquid or ice depending on the temperature. As an example, a case of mixing has been considered with 50% of water and 50% of oil in a cell where the temperature is below the freezing point of water. The error function for phase change gives 50% of water turning into ice. This problem leads to $\alpha_w = 0.5$, $\alpha_{oil} = 0.5$ and $erf(T) = 0.5$. Therefore, applying the new relationship to compute α_ℓ, the following is obtained:

$$\begin{aligned}
\alpha_\ell &= 0.5 \times 0.5 = 0.25 \ , \\
\alpha_s &= 0.5 - 0.25 = 0.25 \ ,
\end{aligned} \tag{16.4}$$

For this particular case and in this specific cell, 25 % of liquid water, 25 % of solid ice and 50 % of oil is obtained, which sums correctly to 100 % in volume. If the old relationship derived in the single-fluid solidification solver had been used here, 50 % of liquid water, 50 % of ice and 50 % of oil would have been obtained. This, obviously, sums over 100 % and is therefore not applicable. As a conclusion, the following relationships for the volume fractions are always satisfied in the solver:

$$\begin{aligned}
\alpha_w &= \alpha_\ell + \alpha s \ , \\
\alpha_{total} &= 1 = \alpha_w + \alpha_{oil} = \alpha_\ell + \alpha s + \alpha_{oil} \ , \\
\alpha_{fluid} &= \alpha_\ell + \alpha_{oil} \ , \\
\alpha_{solid} &= \alpha_s \ .
\end{aligned} \tag{16.5}$$

This simplification has been chosen to ensure fast computation when a linear function of temperature relationship is very computer demanding. Such factor can explain the discrepancies obtained when comparing the current simulations with numerical results from the literature, even if a general good agreement is visible for a relatively fast computing time.

16.1.2 Energy equations for continuous and dispersed phases

The energy equations used for this solver are based on the previous work presented in this report along with the solver twoPhaseEulerFoam from the official OpenFOAM distribution package. The two phases considered here are denoted α_1 for the dispersed water phase and α_2 for the continuous oil phase. The distinction between liquid and solid zone (in the scope of this work, only for the dispersed water phase, i.e for α_1) is performed through the error function discussed previously. Source terms for phase change processes are used for the dispersed phase in both energy and momentum equations. Equations 16.6 and 16.7 give the energy equations for dispersed and continuous phases, respectively.

$$\frac{\partial \alpha_1 T_1}{\partial t} + u\nabla \cdot \alpha_1 T_1 = \alpha_1 \gamma_1 \Delta T_1 + S_t + S_{T_{1-2}} \ . \tag{16.6}$$

$$\frac{\partial \alpha_2 T_2}{\partial t} + u\nabla \cdot \alpha_2 T_2 = \alpha_2 \gamma_2 \Delta T_2 + S_{T_{2-1}} \ . \tag{16.7}$$

Where the term $u\nabla \cdot \alpha_1 T_1$ is expressed (in this example in 2 dimensions) as:

$$u\nabla \cdot \alpha_1 T_1 = u_1 \frac{\partial \alpha_1 T_1}{\partial x} + v_1 \frac{\partial \alpha_1 T_1}{\partial y} \tag{16.8}$$

Left hand sides of both equations (Equations 16.6 and 16.7) are similar to the single-fluid solidification solvers. However, each term is multiplied by the volume fraction of the phase concerned so that water temperature is computed only in the water zone and in a similar manner oil temperature has to be solved only in the oil phase.

The source term (S_t) responsible for phase change in the dispersed energy equation (i.e equation 16.6) is similar to the single-fluid property but applied for the dispersed phase. This source term is not incorporated in the continuous oil equation as no phase change is desired for the continuous phase. The laplacian term is composed of the term γ. This term permits to incorporate turbulence effects into the energy equation. It is expressed as:

$$\gamma = \frac{\lambda}{\rho C_p} + \frac{\nu_t}{P_r} \ . \tag{16.9}$$

where ν_t/P_r represents the turbulence contribution of the phase studied and is equal to zero for laminar cases. This leads to an expression of the laplacian term similar to the single-fluid solver such as:

$$\gamma = \frac{\lambda}{\rho C_p} \ . \tag{16.10}$$

The energy equations presented here represent the heat transfer produced by the interaction of velocity fields, boundary conditions and phase change process. The interaction between dispersed and continuous phases also induce variation of heat. This is accounted for in the last source terms $S_{T_{1-2}}$ and $S_{T_{2-1}}$ of Equations 16.6 and 16.7.

$$S_{T_{1-2}} = \frac{h_{T_1} T_2}{\rho_1 C_{p_1}} \ , \qquad S_{T_{2-1}} = \frac{h_{T_2} T_1}{\rho_2 C_{p_2}} \ , \tag{16.11}$$

The term h_T represents the heat transfer coefficient. The Ranz & Marshall (1958) heat transfer coefficient correlation has been implemented. This correlation is suitable for spherical drops and for the range $0 < R_{e_p} < 200$ and $0 < P_r < 250$. Therefore, in case of a coupling with a PBE solver, the actual diameter of the drops will be used to compute the particulate Reynolds number. The Ranz and Marshall correlation uses the Nusselt number such as:

$$N_u = 2 + 0.6 R_{e_p}^{0.5} P_r^{1/3} \ . \tag{16.12}$$

From Equation 16.12, one can deduce the heat transfer coefficient from phase 1 to phase 2 using :

$$h_{T_1} = \frac{6\lambda_2 \alpha_1 \alpha_2 N_u}{d^2} \ , \qquad h_{T_2} = \frac{6\lambda_1 \alpha_1 \alpha_2 N_u}{d^2} \ . \tag{16.13}$$

16.1.3 Momentum equations for continuous and dispersed phases

The momentum equations presented in this section of the report are based on the previous work for the single-fluid solidification solver along with the solver twoPhaseEulerFoam available from the OpenFOAM official distribution. Equations 16.14 give the momentum equations used for this solver for dispersed and continuous phases, respectively.

$$\begin{aligned}
&\frac{\partial \rho_1 \alpha_1 u_1}{\partial t} + u\nabla \cdot \rho_1 \alpha_1 u_1 + S_{turb} = -\nabla p_1 + \mu_1 \Delta u_1 - g[\rho(T)' - \rho_1] - S_m - S_{forces} \ , \\
&\frac{\partial \rho_2 \alpha_2 u_2}{\partial t} + u\nabla \cdot \rho_2 \alpha_2 u_2 + S_{turb} = -\nabla p_2 + \mu_2 \Delta u_2 - g\rho_2 - S_{forces} \ .
\end{aligned} \tag{16.14}$$

These equations are similar to the single-fluid solvers but applied for multiphase solidification processes. However, few terms have been added to this solver. The term S_{turb} represents the turbulence contribution to the momentum equations. It is possible to use several RANS turbulence models with this solver (i.e k-ε, k-ω ...). This term is expressed as:

$$S_{turb} = \frac{\partial}{\partial x_j}\left[\nu_{eff}\left(\frac{\partial u_i}{\partial x_j} + \frac{\partial u_j}{\partial x_j} - \frac{1}{3}\frac{\partial u_k}{\partial x_k}\delta_{i,j}\right)\right] \ . \tag{16.15}$$

The term S_m represents the sink of velocity in the fully solid zone, as for the single-fluid solver. It is a combination of ice and water volume fractions along with a Darcy source term. This term is only present for the dispersed phase momentum equation as the oil (continuous phase) has been prevented from solidification in this solver. Finally, the term S_{forces} represents the contribution of the interfacial forces acting between the continuous and the dispersed phase. This term can contain drag, lift, turbulent dispersion and virtual mass or a combination of each of them. A full explanation of these forces and a selection of different model available is given in the previous part of this thesis.

16.2 Natural convection process modelling

In this section, a bi-dimensional single-fluid simulation of water in natural convection is investigated in a cavity of height $\ell = 80\ mm$. The numerical results presented here are compared with experimental data from Giangi et al. (2000). The top and bottom walls of the numerical are assumed adiabatic and a temperature gradient is induced from the left wall ($T_\ell = 10\ °C$) to the right wall ($T_r = 0\ °C$). During experiments, a heat flux condition has been used for the adiabatic walls as designing an adiabatic condition can be complicated in the experimental work. The multiphase solidification solver (IMP) is validated against these experiments. A comparison between experimental results for y-velocity and temperature fields is performed along two lines inside the computational domain, at $x = 0.9\ell = 72\ mm$ and at $y = 0.5\ell = 40\ mm$. Figure 16.2 presents the results obtained, once the steady-state is achieved.

As can be seen from Figure 16.2 the results obtained are fairly close to experiments. This statement proves that the solver, presently developed, is able to compute natural convection processes. It can be noted that slight discrepancies are observed however. In particular, for each one of the four sets of results, a slight shift is present between experimental work of Giangi et al. (2000) and the present numerical simulations. As mentioned previously in this thesis, this is mainly attributed to the differences betweeen the experimental and the numerical set-up.

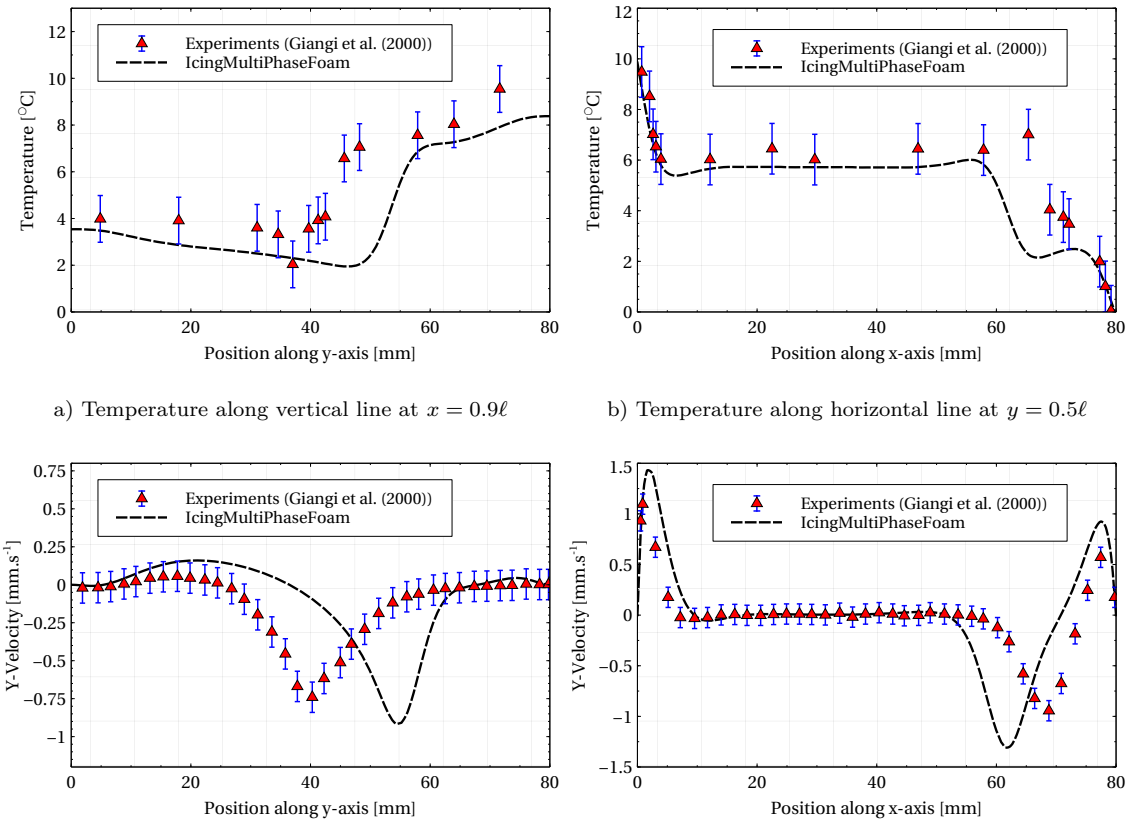

a) Temperature along vertical line at $x = 0.9\ell$

b) Temperature along horizontal line at $y = 0.5\ell$

c) V-velocity along vertical line at $x = 0.9\ell$

d) V-velocity along along horizontal line at $y = 0.5\ell$

FIGURE 16.2: Numerical results obtained with IcingMultiPhase for convection problem

16.3 Solidification process modelling

The test case presented here is a three dimensional solidification problem in a cubic cavity. All walls are kept at a fixed temperature which varies for the different cases studied (i.e. Case 1 $T_h = 5°C$, Case 2 $T_h = 10°C$, Case 3 $T_h = 15°C$ and Case 4 $T_h = 20°C$) except from the top wall, which is kept at $T_c = -10°C$. Ice formation from the top wall toward the centre of the computational domain is recorded through time. Results are compared with experimental data. The ice-layer height is made dimensionless using the relationship shown in Equation 16.16.

$$I_\ell = \frac{\ell - f_s}{\ell} \ , \tag{16.16}$$

where ℓ is the ice layer and f_s is the solid fraction. Figure 16.3 shows the velocity streamlines, the temperature iso-contours and the ice shape and growth under the lid at $t = 5.8\ min$, $t = 30\ min$ and $t = 50\ min$. It is shown that the solidification rate happens faster at the beginning ($t < 350$ s) before slowing down to reach a pseudo-constant evolution at later time ($t > 1800$ s).

Figure 16.4 gives a comparison between the numerical results obtained with IcingMultiPhaseFoam and the experimental study of Kowaleski and Cybulski.

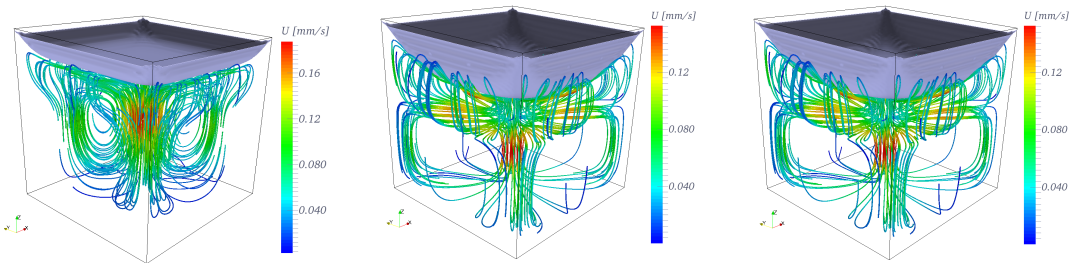

a) Velocity streamlines ($t = 350\ s$) b) Velocity streamlines ($t = 1800\ s$) c) Velocity streamlines ($t = 3000\ s$)

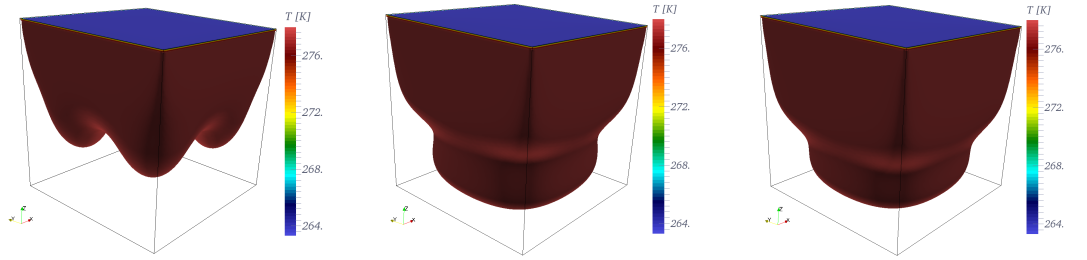

d) Temperature contours ($t = 350\ s$) e) Temperature contours ($t = 1800\ s$) f) Temperature contours ($t = 3000\ s$)

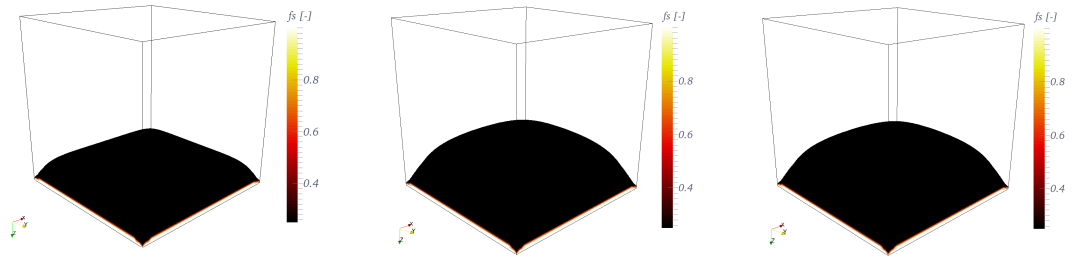

g) Ice-layer under the lid ($t = 350\ s$) h) Ice-layer under the lid ($t = 1800\ s$) i) Ice-layer under the lid ($t = 3000\ s$)

FIGURE 16.3: Numerical results obtained with MultiIcingFOAM for solidification problem

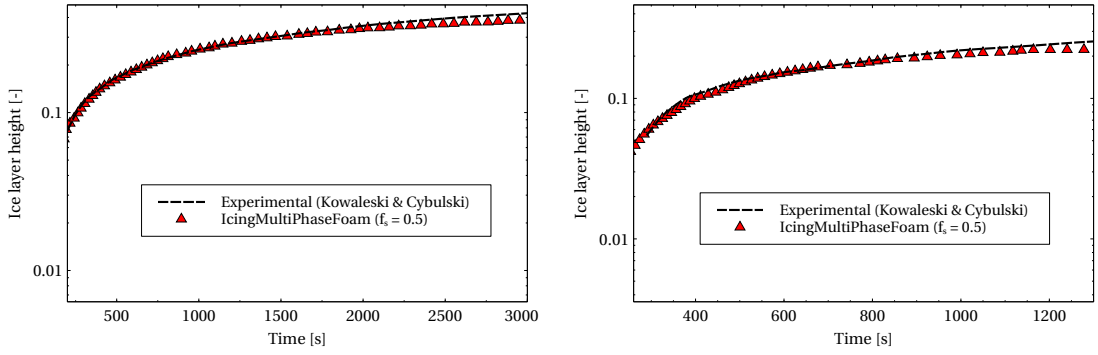

a) $T_h = 5°C$ b) $T_h = 10°C$

FIGURE 16.4: Comparisons between MultiIcingFOAM and experimental ice-layer

It can be seen, from Figure 16.4, that the numerical results obtained with the newly designed mutli-fluid solidification solver are very close to the experimental measurements of Kowaleski and Cybulski and thus for both initial temperatures. As observed in Figure 16.3 and for the previous solidification studies (i.e. Part III)

the solidification process is much faster at the beginning of the simulation before reaching an almost constant slope over time where boundary conditions and internal parameters seem to be in equilibrium. The present results confirm that the multi-fluid solidification solver provides very accurate results for solidification process in 3 dimensional domains. Additional studies could be performed in order to validate this solver further.

Finally, the same case as the one presented in Section 11.2 is studied here. The difference is that, in this section, the new multi-fluid solver is used for the numerical simulations. To achieve this, the presence of the oil phase is neglected and only the water equations are solved. This test has been performed to check wether or not this multi-fluid solver is suitable for single-fluid problems and if the energy and momentum equations have been implemented correctly. Specifications and boundary conditions will not be detailed here as they are those previously discussed in Section 11.2. Numerical results obtained with this solver (MultiIcingFoam) are compared to those from IcingFOAM and Fluent results, being extracted from the literature. Figure 16.5 shows a comparison of the water velocity magnitude and the ice layer obtained after 100 seconds of simulation for single-fluid solver (IcingFoam) and multi-fluid solver (MultiIcingFoam).

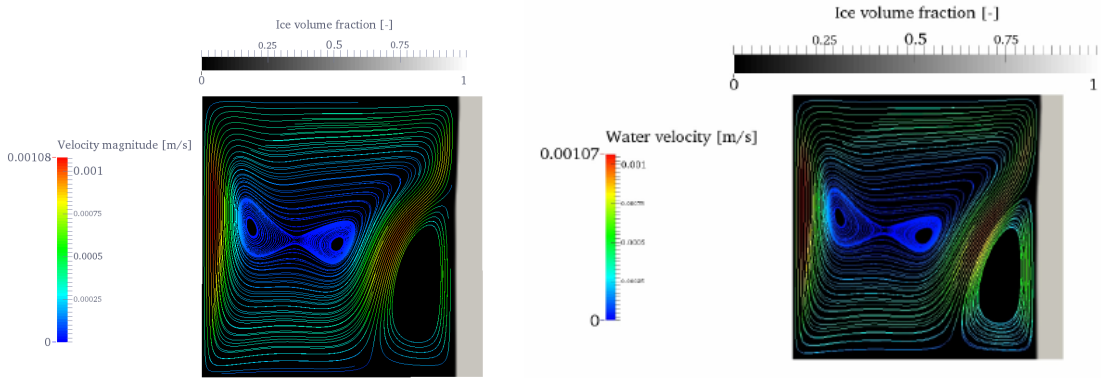

a) $t = 100\ s$ IcingFoam

b) $t = 100\ s$ MultiIcingFoam

Figure 16.5: Solidification rate process with IcingFoam and MultiIcingFOAM

Figure 16.5 shows that results obtained with both solver are extremely close. A better comparison is given in Figure 16.6 where temperature, axial and vertical components of velocity are plotted along both horizontal and vertical lines. Results obtained from MultiIcingFoam are compared to IcingFoam (Bourdillon et al., 2015) and Fluent (Michalek & Kowaleski, 2002).

Numerical results show good agreement with the previous single-fluid solver validated against literature data. Small discrepancies are observed between the two solvers. This is attributed to the fact that different correlations have been used for heat capacity, viscosity and thermal conductivity in the solvers, as explained in Section 16.1.1 of this thesis. Overall both approaches are comparable, which confirms that energy and momentum equations implemented in the multi-fluid solver are suitable and accurate when applied to single-fluid problems.

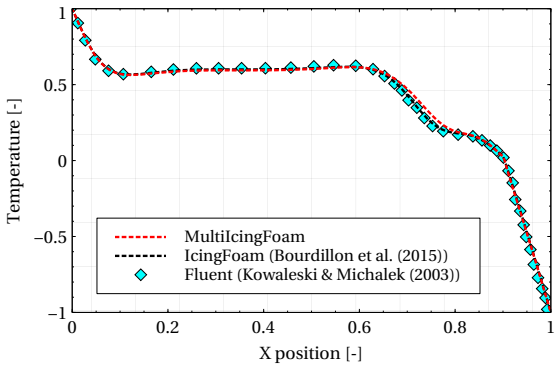

a) Temperature along horizontal line

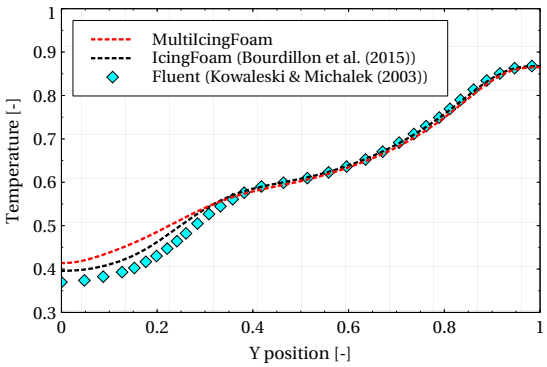

b) Temperature along vertical line

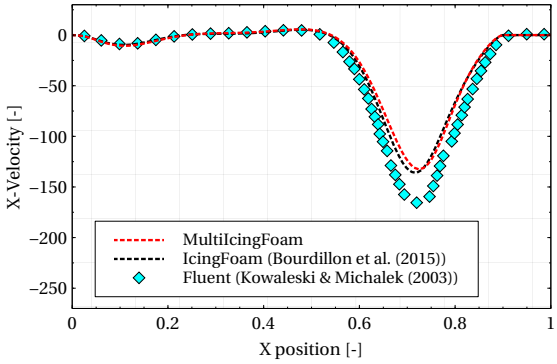

c) U-velocity along horizontal line

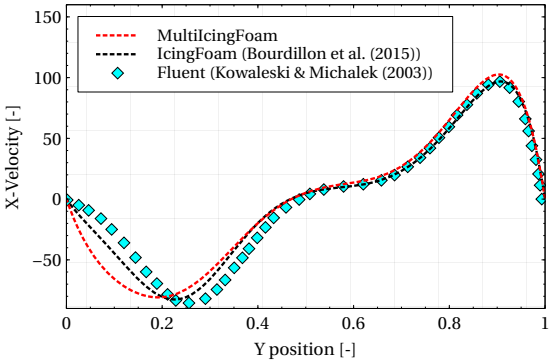

d) U-velocity along vertical line

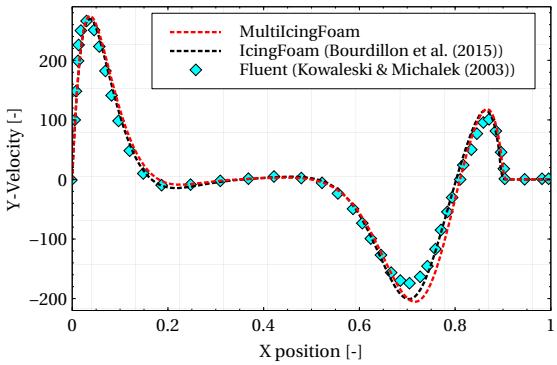

e) V-velocity along horizontal line

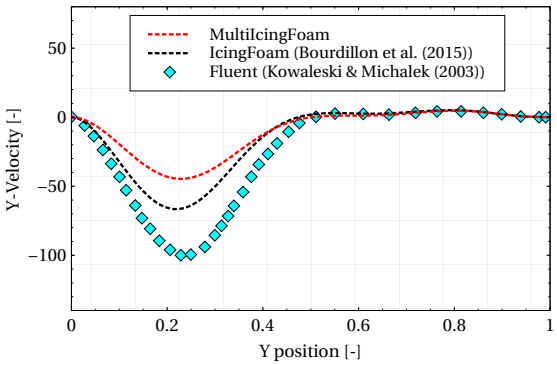

f) V-velocity along vertical line

FIGURE 16.6: Numerical results obtained with IcingFoam and MultiIcingFOAM

This chapter provided a derivation of the numerical model implemented in the open source software OpenFOAM. Thanks to the findings from Part III, a thorough literature review and implementation choices, the multi-fluid solidification solver has been proven to be accurate for both 2D and 3D freezing studies. Additionally, its Eulerian-Eulerian formulation has been specifically chosen to reduce computational time and has been designed so that key parameters (volume fraction, velocity and temperature fields) mandatory for freezing studies could be retrieved from a population balance solver. This is discussed in the next Chapter of this thesis, Chapter 17.

Chapter 17

Population balance modelling for multiphase flow

This chapter presents the numerical model developed to handle population balance modelling in OpenFoam environment. It is, partly, based on findings from Part II of this thesis. As a result, the Lo and Rao model for break-up and coalescence and interface term handling have been implemented. Development choices to make the solver more robust and much easier to maintain are discussed in this chapter. Additional develoment taken in an attempt to improve further the current break-up model are also detailed. Preliminary results are presented and finally, the design choices taken to ensure a future possible coupling are explained in the conclusion section of this part.

The model developed here is based on a standard method of moment. This type of model has been chosen for its relative ease of implementation compared to the most recent QMOM or DQMOM methods (see Part II for a full explanation). More importantly, it has been shown by several researchers to be more computationally efficient than other standard methods such as Monte-Carlo or method of classes (see Part II). Additionally to a standard method of moment, the break-up and coalescence models of Lo and Rao have been implemented as previous findings in this PhD work have proven that this model can give accurate results when properly used. To address the comments in Part II (i.e. that a possible further enhancement of the break-up model could lead to a better overall model) new features have been added to this solver. Momentum and energy equations derived from the twoPhaseEulerFoam solver, standard method of moment implementation, break-up and coalescence models and finally interfacial terms treatment are presented.

17.1 Continuity, momentum and energy equations

The PBM implemented in this work is based on an Eulerian-Eulerian framework. All phases are assumed to be in equilibrium state. Each one has its own velocity, energy and material properties. The continuity equations, in this solver and in twoPhaseEulerFoam can be written as shown in Equation 17.1:

$$\begin{aligned} \frac{\partial \alpha_i \rho_i}{\partial t} + \nabla \cdot (\alpha_i \rho_i \mathbf{u}_i) = 0, \\ \frac{\partial \alpha_j \rho_j}{\partial t} + \nabla \cdot (\alpha_j \rho_j \mathbf{u}_j) = 0. \end{aligned} \tag{17.1}$$

Equation 17.1 is written here in its most basic form, without taking into account any mass transfer between phases. In Equation 17.1, α denotes the volume fraction, $\mathbf{u}$ the velocity vectors and ρ the density whereas the subscript i refers to the phase i (continuous phase) and the subscript j stands for the dispersed phase.

Momentum equations (Equation 17.2) can be written as:

$$\begin{aligned} \frac{\partial \alpha_i \rho_i \mathbf{u}_i}{\partial t} + \nabla \cdot (\alpha_i \rho_i \mathbf{u}_i \mathbf{u}_i) = \alpha_i \rho_i \mathbf{g} - \alpha_i \Delta p + \nabla \cdot [\alpha_i (\tau_i + \tau_i^t)] + \mathbf{F}_i^{int}, \\ \frac{\partial \alpha_j \rho_j \mathbf{u}_j}{\partial t} + \nabla \cdot (\alpha_j \rho_j \mathbf{u}_j \mathbf{u}_j) = \alpha_j \rho_j \mathbf{g} - \alpha_j \Delta p + \nabla \cdot [\alpha_j (\tau_j + \tau_j^t)] + \mathbf{F}_j^{int}, \end{aligned} \tag{17.2}$$

where p stands for the pressure field, $\mathbf{g}$ is the gravitational acceleration vector, $\mathbf{F}^{int}$ represents the internal forces acting on the phase i (this term is derived in the next section of this thesis), τ and τ^t are the molecular and turbulent stress tensor, respectively. Similarly to the continuity equation (Equation 17.1), the momentum equations are derived without taking into account the mass transfer between the phases.

Finally the energy equations are solved in this solver to handle heat transfer between phases (Equation 17.3).

$$\begin{aligned}\frac{\partial[\alpha_i\rho_i(h_i+K_i)]}{\partial t}+\nabla\cdot[\alpha_i\rho_i(h_i+K_i)\mathbf{u}_i]&=\alpha_i\gamma_i\Delta T_i+S_{T_{1-2}},\\ \frac{\partial[\alpha_j\rho_j(h_j+K_j)]}{\partial t}+\nabla\cdot[\alpha_j\rho_j(h_j+K_j)\mathbf{u}_j]&=+\alpha_j\gamma_j\Delta T_j+S_{T_{2-1}}.\end{aligned} \tag{17.3}$$

In Equation 17.3, the terms h and K stand for the specific enthalpy of the phase concerned and the kinetic energy respectively. The additional terms present in Equation 17.3 have been explained previously in this thesis. It can be noted that, by expressing the specific enthalpy as a function of the heat capacity, by neglecting the heat transfer between continuous and dispersed phases and the kinetic energy contribution, one can retrieve a similar energy equation as in the convection solver derived in Part III.

These three sets of two equations are solved within the PBM solver and velocity and temperature fields can be extracted. Conjointly, the moments are computed and break-up and coalescence events are taken into account. This is discussed in the next section of this thesis.

17.2 Break-up modelling

Moment-based methods can be used to overcome the closure problem of the population balance equations. The $S-\gamma$ model has been used here. This model solves the transport equations for the moments (m) of the diameter size distribution as:

$$m_\gamma = n\int_0^\infty d^\gamma P(d)d(d)\ , \tag{17.4}$$

with γ the order of the moment, n the number of particles per volume, d the particle diameter and $P(d)$ the probability density function of particle diameter.

For the present solver, simplifications and improvments have been made when compared to the Lo and Rao (Lo & Rao, 2007) model.

Equations have been rewritten in such a way that the random variables are dimensionless. Instead of using a log-normal distribution for the diameter d (as in the current Lo & Rao (2007) model), a log-normal distribution for d/d_{32} is used.

As a result, the probability density function $P(d)$, can be rewritten as in Equation 17.5:

$$P(d)=\frac{1}{d\sqrt{2\sigma}}\exp\left(-\frac{\log^2(d/d_{32})}{\sigma^2}\right). \tag{17.5}$$

The moment calculation for a log-normal distribution can be written as:

$$m_k=\exp\left(k\mu+\frac{k^2\sigma^2}{2}\right). \tag{17.6}$$

As $\mu = 0$, Equation 17.6 can be further simplified and, in particular, leads to the expression given in Equation 17.7 for the second order moment:

$$m_2 = \frac{S_2}{S_0 d_{32}^{-2}}. \tag{17.7}$$

Finally, the expressions for viscous and inertia break-up can be reformulated as given in Equation 17.8 for the second order moment:

$$\begin{aligned} S_{br,v} &\sim \int_{d_{cr}}^{L_k} \exp\left(-\frac{\log^2(d/d_{32})}{2\sigma^2}\right) d(d), \\ S_{br,i} &\sim \int_{max(d_{cr,i},L_k)}^{\infty} d^{-1/2} \exp\left(-\frac{\log^2(d/d_{32})}{2\sigma^2}\right) d(d). \end{aligned} \tag{17.8}$$

Due to these simplifications and improvements, only a single transport equation is solved for S_2. As droplets are considered spherical, this assumed tha $d_{32} = d_{30}$ and therefore, S_0 is calculated based on this statement. Finally, the moment inversion method is changed to only use S_0, S_2 and S_3. By expanding these relationships, the following three set of Equations are obtained:

$$\begin{aligned} d_{32} &= \frac{S_3}{S_2} = \frac{\pi\alpha}{6S_2}, \\ d_{30} &= \frac{S_3}{S_0}^{1/3} = \left(\frac{\pi\alpha}{6S_0}\right)^{1/3}, \\ S_0 &= \frac{S_2^3}{S_3^2} = S_2^3\left(\frac{6}{\alpha\pi}\right)^2. \end{aligned} \tag{17.9}$$

As a conclusion, the following transport equations are solved for each moment γ of the distribution in the $S - \gamma$ model:

$$\frac{\partial m_\gamma}{\partial t} + \nabla \cdot (m_\gamma \mathbf{u}) = S = S_{br} + S_{coal} \ . \tag{17.10}$$

The right hand-side of Equation 17.10 contains the source terms responsible for break-up S_{br} and coalescence S_{coal} during the droplet transport. Break-up and coalescence terms are a sum of birth and death rates, as expressed in Equation 4.11. This is similar to the S-γ model of Lo and Rao and the rest of this solver is very similar to it. Finally, the assumptions and simplifications made in this new solver implemented in OpenFOAM permit to greatly simplify the model. Additional simplifications and improvments of the coalescence model of Lo and Rao (Lo & Rao, 2007) have been implemented and are discussed in the next section of this thesis.

17.3 Coalescence modelling

The coalescence model used here, described in Lo & Rao (2007), is based on a standard method of moments. It considers the probability of collision of droplets,

the contact time of two colliding droplets and the drainage time of the liquid film between them. This model uses an equivalent diameter d_{eq} for each moment from which the expression of the source term for coalescence event can be obtained (Lo & Zhang, 2009):

$$\frac{dm_\gamma}{dt} = C_{coll}(2^{\gamma/3} - 2)K_{coll}P_{coll}(d_{eq})d_{eq}^{\gamma}. \tag{17.11}$$

By further investigating the model and the parameters, an important simplification can be made, based on the rewritting of the break-up equations. For the second order moment, the coalescence term can be expressed as:

$$S_{c,2} = C_{coll}\left(2^{2/3} - 2\right)K_{coll}P_{coll}(d_{eq})d_{eq}^{-2}S_3^2 u_{rel}. \tag{17.12}$$

However, the equivalent diameter can be rewritten in the following form:

$$d_{eq} = k_{cl,1}d_{32} = k_{cl,1}\frac{S_3}{S_2}. \tag{17.13}$$

By substituting Equation 17.13 into Equation 17.12, the following expression can be deduced:

$$S_{c,2} = C_{coll}\left(2^{2/3} - 2\right)K_{coll}P_{coll}(d_{eq})\frac{k_{cl,1}^{-2}S_2^2}{S_3^2}S_3^2 u_{rel}. \tag{17.14}$$

The term S_3 can therefore be eliminated. Futhermore, it removes arbritariness regarding the definition of S_3. As a result, the final definition of the coalescence term can be written as follows for the second order moment:

$$S_{c,2} = C_{coll}\left(2^{2/3} - 2\right)K_{coll}P_{coll}(d_{eq})k_{cl,1}^{-2}S_2^2 u_{rel}. \tag{17.15}$$

This finding simplifies the model as it removes the need to perform an additional division by S_3. The rest of the coalescence model is similar to the Lo and Rao mode. In particular, the viscous collision, inertial collision and drainage time model are similar.

The numerical model for this solver has been presented. In particular, the continuity, momentum and energy equations have been derived. Interfacial terms are derived in the next section and the numerical choices are explained. As a final section, the preliminary results obtained with this new solver are presented. This solver is still in development and additional improvements are discussed in the future work section of this thesis.

17.4 Interfacial forces

The previous findings in this thesis (Part II) show that, usually, the interfacial forces are computed as a sum of drag, lift, turbulent dispersion and virtual mass forces. However, it has been noticed that the virtual mass force can be neglected. As a

result, only the contribution of the drag, lift and turbulent dispersion forces have been taken into account and implemented in this new PBM solver. The next sections of this thesis details a derivation of each force and the model implemented.

17.4.1 Drag force

The drag force can be expressed in the following general form:

$$F^D = C^D \frac{\rho_c}{2} \pi r_p^2 |\mathbf{u_r}| \mathbf{u_r}, \tag{17.16}$$

where r_p is the radius of a particle, $\mathbf{u_r}$ is the relative velocity between the different phases and C^D is the actual drag coefficient. In order to take account of an eventual non-spherical shape of droplets, any correction can be added to the general expression of the drag force through the drag coefficient. The drag coefficient is therefore expressed as the multiplication of a single-particle drag coefficient (C^D_∞) and a drag correction factor (f^D) which can correct several important parameters such as the droplet size, shape or terminal velocities:

$$C^D = C^D_\infty f^D. \tag{17.17}$$

As mentioned previously, the Richardson & Zaki (1997) correction model is the most suitable for droplet of relatively small diameters (i.e from 1.0×10^{-9} to 1.0×10^{-3} m). This correlation model has been implemented along with two drag models (based on the findings from Part II of this thesis): the Schiller and Naumann model (Schiller & Naumann, 1935) and the Snyder et al. model (Snyder et al., 2007). For the sake of clarity their formulation is briefly recalled in the following two subsections.

17.4.1.1 Schiller and Naumann model

This model is based on the drag law of Stokes, which approaches the drag coefficient as $C^D = \frac{24}{\mathrm{Re}_d}$ for $\mathrm{Re} < 1$. Schiller & Naumann (1935) extended the applicability of the model to intermediate Re by means of a dimensionless multiplication factor which takes into account the inertial effects on the drag force. The model is acurate for spherical and non-deformable particles as Klaseboer et al. (2001) have experimentally proved.

The expression of the drag coefficient in the Schiller & Naumann (1935) model is based on the particle Reynold's number defined as follows:

$$\mathrm{Re}_d = \frac{\rho_c |\mathbf{u_r}| d}{\mu_c}, \tag{17.18}$$

where d stands for the particle diameter. The standard drag coefficient is then expressed as:

$$C^D = \begin{cases} \frac{24\left(1+0.15\mathrm{Re}_d^{0.687}\right)}{\mathrm{Re}_d} & \mathrm{Re}_d \leq 1000 \\ 0.44 & \mathrm{Re}_d > 1000 \end{cases} \tag{17.19}$$

17.4.1.2 Snyder et al. model

More recently, Snyder et al. (2007) developed a new drag model based on the particle Reynolds number where the drag coefficient is defined as:

$$C^D = \begin{cases} \frac{24}{\mathrm{Re}_d} & \mathrm{Re}_d < 1 \\ \frac{24}{\mathrm{Re}_d}\left[1 + \frac{3.6}{\mathrm{Re}_d^{0.313}}\left(\frac{\mathrm{Re}_d - 1}{19}\right)^2\right] & 1 \leq \mathrm{Re}_d \leq 20 \\ \frac{24}{\mathrm{Re}_d}\left(1 + 0.15\mathrm{Re}_d^{0.687}\right) & 20 \leq \mathrm{Re}_d \end{cases} \tag{17.20}$$

17.4.2 Lift force

The lift force expression, used in this model, is derived from Auton & Hunt (1988) and it is based on the curl of the continuous phase velocity following:

$$F^\ell = \alpha_d C^\ell \rho_c \left[\mathbf{u_r} \text{ x } (\nabla \text{ x } \mathbf{u_c})\right]. \tag{17.21}$$

It has been shown in Part II that the lift force acts perpendicular to the relative motion of a droplet and tends to enhance the break-up rate in the cases investigated here. Hence, the presence of this force can have a significant impact on the droplet size prediction, especially when break-up and coalescence phenomena are considered and known to be closely dependent of both shear stress and turbulence rate.

17.4.3 Turbulent dispersion force

The turbulent dispersion force results from the combined actions of the interphase drag and the turbulent surrounding eddies of the continuous phase. The physical effect of the force results in moving the particles from high to low concentration areas and get transported by the effects of the drag force. This force is very important for our study case and has to be taken into account as the initial conditions of the problem separate very high concentration of droplet from very low.

The turbulent dispersion force is expressed, in this model, as follows:

$$F_{ij}^{td} = C^D \frac{\rho_c}{2} \frac{a_{ij}}{4} |\mathbf{u_r}| \frac{\nu_c^t}{\sigma_\alpha} \left(\frac{\nabla \alpha_j}{\alpha_j} - \frac{\nabla \alpha_i}{\alpha_i}\right), \tag{17.22}$$

where the first part of Equation 17.22 is deduced from the drag coefficient C^D, the term ν_c^t represents the continuous phase turbulent kinematic viscosity and σ_α is the turbulent Prandtl number, usually taken to be equal to unity.

17.5 Preliminary results

For consistency with the previous part of this thesis (Part II), the same numerical studies have been performed. The test case selected for this study has been taken from Simmons & Azzopardi (2001) experiments. During their experiments they

have conducted multiple test cases for droplets dispersed in oil in both horizontal and vertical pipes. By injecting droplets near the inlet of the pipe with several diameters, they were able to capture the evolution of the droplet diameter travelling through the pipe. The experiments were conducted in a 4.5 m long pipe were droplets were transported by an oil continuous phase within a diameter conduit of 63 mm. The dispersed phase used was an aqueous potassium carbonate solution, slightly heavier than water, to represents the salted water. The continuous phase has been chosen to be kerosene. The interfacial tension has been set, according to experiments, to $\sigma = 0.01\ N/m$.

Table 17.1 gives the material properties of the two phases used in the experiments.

Table 17.1: Material properties of the two phases

Phase	Type	$\rho\ [Kg.m^{-3}]$	$\mu\ [kg.m^{-1}.s^{-1}]$	u $[m.s^{-1}]$	α [%]
Kerosene	Continuous	797	0.0018	2.393	93.8
Aqueous potassium	Dispersed	1166	0.0016	0.158	6.2

In order to minimize the formation of dispersion at the inlet, a special inlet arrangement for the experiment has been designed. The droplets are introduced in the pipe through perforated hole in the wall near the inlet. This inlet arrangement allows the droplets to be created by turbulence and mixing within the pipe, where they start their motion in regions where turbulence and break-up rates are the strongest. To accurately represent this inlet arrangement, the inlet of the computational domain has been separated into two sections, following Lo & Rao (2007) recommendations who conducted the same sort of numerical analysis of this case. Hence, the droplets are injected in the computational domain through a ring close to the wall only whereas the center of the pipe is filled with kerosene only. During the experiments, different initial droplet diameters were used, from 750, 1000 and 1500 μm. It has been shown by Lo & Rao (2007) that within this range of diameters, only little difference on the result appears. For the numerical simulation presented in this chapter, a standard initial diameter of 1000 μm was used.

For this particular new solver designed in OpenFOAM, simplifications and improvements have been made. Only the S_2 moment is specifically solved compared to the Lo and Rao model (Lo & Rao, 2007). As a result, for the water inlet, the boundary condition is reduced to $\alpha_{water} = 1$ and $S_3 = \frac{6}{\pi}$.

As an example, for $d_{32} = 400\mu m$, S_2 is computed as follows:

$$S_2 = \frac{6}{\pi 400} \sim 4770 m^{-1}. \tag{17.23}$$

Figure 17.1 gives the preliminary results obtained with this solver. It gives a representation of both the break-up and coalescence rate along the pipeline.

It is shown, in Figure 17.1 that the fields for break-up and coalescence are comparable so far. Further enhancements are however needed, especially for the magnitude of the break-up terms and to further enhance the calibration of the model. A similar settling of droplets as of Part II is observed with this model and, additionally,

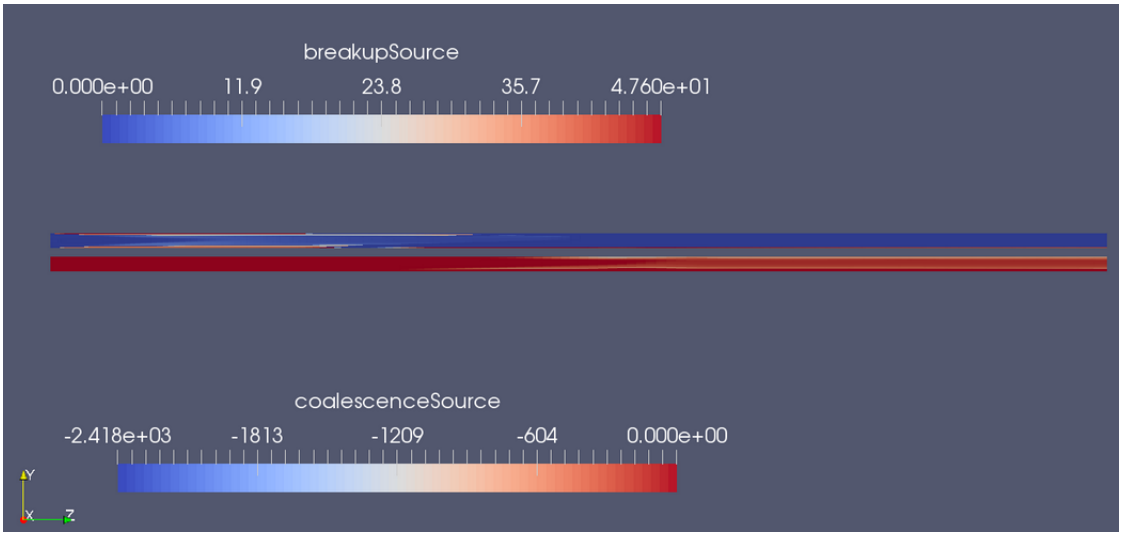

FIGURE 17.1: Break-up and coalescence rate obtained with PBMFoam solver

the largest droplets tend to move toward the bottom of the pipe due to gravity effects. This shows that, qualitatively, the results computed with this new PBM solver match those previously presented.

This model is currently undergoing several testing, improvements and scaling. As it stands, and based on the findings described in this thesis, one can easily use it and improve it for further investigations.

Chapter 18

Conclusions and discussions

The recent developments and enhancements based on findings from both PartII and Part III have been presented. First of all, an introduction has been given. It has been pointed out that this Part will only present partially achieved results as the field of study is quite new. To the author's knowledge, no researcher has attempted to couple a PBM and a solidification solver within an Eulerian-Eulerian framework. A promising multi-fluid solidification solver has been derived and partially validated against both numerical and experimental results. It has been shown that the current solver produces accurate results for ice-layer growth inside a 3D cavity. Further validation are necessary, however, due to the lack of experimental studies in this particular field, this could not be achieved within the scope of this thesis. Nonetheless, the developed solver could be easily enhanced as all the necessary parameters are computed. In addition, a population balance model, based on a standard method of moment has been developped, based on the existing model from Lo & Rao (2007). So far, only in house tests have been performed and the model is still undergoing significant changes and improvements. It has been shown that both break-up and coalescence rates obtained with this solver when used for experimental case in the literature are comparable. As a conclusion, all solvers described in this work could be used conjointly, to tackle solidification problems where change of droplet size is taken into account. This is discussed further in the future work section of this thesis.

Nomenclature

Dimensionless numbers

A_H	Hamaker constant	$[-]$
C_a	Capillary number	$[-]$
E_o	Eötvös number	$[-]$
W_e	Weber number	$[-]$
R_e	Reynolds number	$[-]$
y^+	Non-dimensional wall distance	$[-]$
CFL	Courant, Friedrichs and Lewy condition	$[-]$
erf	Error function	$[-]$
P_r	Prandtl number	$[-]$
R_a	Rayleigh number	$[-]$

Greek letters

α	Volume fraction	$[-]$
β	Thermal expansion coefficient	$[K^{-1}]$
γ	Thermal diffusivity	$[m^2.s^{-1}]$
λ	Thermal conductivity	$[W.m^{-1}.K^{-1}]$
μ	Dynamic viscosity	$[kg.m^{-1}.s^{-1}]$
ν	Kinematic viscosity	$[m^2.s^{-1}]$
$\rho(T)$	Polynomial density variation	$[kg.m^{-3}]$
ρ	Density	$[kg.m^{-3}]$
χ	Shear rate	$[s^{-1}]$
Δt	Time step	$[s]$
η	Log-normal distribution	$[-]$
Φ	Phase difference	$[-]$
σ	Surface tension	$[kg.s^{-2}]$
$\tau(d)$	Time scale	$[s]$
ε	Turbulent energy dissipation rate	$[m^2.s^{-3}]$
ξ	Internal properties	$[-]$
ζ	Free-stream fraction	$[-]$

Roman letters

ℓ	Length	$[mm]$
C_p	Specific heat capacity	$[J.kg^{-1}.K^{-1}]$
C_s	Switching constant	$[-]$
d	Diameter	$[mm]$
D'_c	Darcy constant in slurry model	$[kg.m^{-3}.s^{-1}]$
D_c	Darcy constant	$[kg.m^{-3}.s^{-1}]$
F_m	Mushy switching function	$[-]$
F_s	Slurry switching function	$[-]$
g	Gravitational acceleration value	$[m.s^{-2}]$
H	Enthalpy	$[J]$
h	Specific sensible enthalpy	$[J]$
L	Latent heat of fusion	$[J.kg^{-1}]$
p	Pressure	$[Pa]$
T	Temperature	$[K, ^\circ C]$
t	Time	$[s]$
t_h	Thickness	$[mm]$
T_{liq}	Liquidus temperature	$[K]$
T_{sol}	Solidus temperature	$[K]$
u	x-velocity	$[m.s^{-1}]$
v	y-velocity	$[m.s^{-1}]$
x	Horizontal coordinate	$[-]$
y	Vertical coordinate	$[-]$
$\dot{m}$	Mean	$[-]$
$\dot{w}$	Width	$[-]$
ℓ_ε	Length scale	$[m]$
ℓ_l	Lower limit	$[-]$
A	Area	$[m^2]$
a	Acceleration component	$[m.s^2]$
$d_{3,0}$	Three-zero diameter	$[m]$
$d_{3,2}$	Sauter mean diameter	$[m]$
E	Production terms	$[-]$
F	Forces	$[kg.m.s^{-2}]$
f	Film	$[-]$
G	Rate change of particle properties	$[s^{-1}, kg^{-1}, m^{-1}]$
g	Gravitational acceleration value	$[m.s^{-2}]$
K	Rate	$[s^{-1}, kg^{-1}, m^{-1}]$
k	Turbulent kinetic energy	$[m^2.s^{-2}]$
L_K	Kolmogorov length scale	$[m]$
M	Interphase momentum transfer	$[-]$
N	Total number density	$[-]$
n	Number density function	$[-]$
$N(d)$	Child produced during break-up	$[-]$
P	Probability density function	$[-]$
R	Modulus of mean strain rate tensor	$[s^{-1}]$
r	Radius	$[m]$
S	Source term	$[-]$

u_l	Upper limit	[−]

Subscripts

ℓ	Liquid phase	[−]
	Dimensionless values	[−]
c	Coolant	[−]
$crit$	Critical value	[−]
i	Internal field	[−]
m	Maximum value	[−]
r	Reference value	[−]
s	Solid phase	[−]
w	Wall	[−]
w_l	Left wall	[−]
w_r	Right wall	[−]
∞	Single-particle	[−]
b	Buoyancy	[−]
br	Break-up	[−]
c	Continuous phase	[−]
$coall$	Coalescence	[−]
$coll$	Collision	[−]
$crit$	Critical value	[−]
d	Dispersed phase	[−]
$drain$	Drainage	[−]
eq	Equivalent value	[−]
Hy	Hydraulic	[−]
i, j, l	Phases i, j or l	[−]
if	Interfacial	[−]
in	Inertial	[−]
k	Kinetic energy contribution	[−]
m	Mixture	[−]
max	Maximum value	[−]
min	Minimum value	[−]
p	Particle	[−]
vi	Viscous	[−]

Superscripts

$'$	Fluctuating part	[−]
ℓ	Lift	[−]
$Birth$	Birth of droplet	[−]
D	Drag	[−]
$Death$	Death of droplet	[−]
int	Internal	[−]
$mass$	Mass	[−]

mom	Moment	$[-]$
T	Transpose	$[-]$
t	Turbulent	$[-]$
td	Turbulent dispersion	$[-]$
th	Thickness	$[m]$
vm	Virtual mass	$[-]$

Source terms

S'_{m_x}	x-source term in slurry model	$[kg.m^{-3}.s^{-1}]$
S'_{m_y}	y-source term in slurry model	$[kg.m^{-3}.s^{-1}]$
S_{m_x}	x-source term in mushy model	$[kg.m^{-3}.s^{-1}]$
S_{m_y}	y-source term in mushy model	$[kg.m^{-3}.s^{-1}]$
S_t	Source term in energy equation	$[J.m^{-3}.s^{-1}]$

Part V

Final conclusions and future work

19 Final conclusions and discussions 163

20 Future work 166

References 166

Chapter 19

Final conclusions and discussions

The aim of this PhD was to investigate, numerically, two very important phenomena observed during the transport of water and oil in pipelines under extreme conditions. They are the evolution of the droplet size distribution and the freezing events. The main goal was, for each of these problems, to identify which parameters are important to improve the current models and generate a possible coupling between population balance and solidification models. This thesis therefore focused on the analysis of key parameters, often depreciated, to improve the way these problems are currently tackled. A new approach has been proposed towards a coupling between population balance and solidification models. In order to ensure the completion of this final objective, several new solvers have been implemented in the open-source CFD code: OpenFOAM and validated against experimental data.

A thorough numerical investigation of droplets size distribution evolution in an horizontal pipeline (through a PBM approach) has highlighted important findings. It has been shown that the forces acting at the droplets interphase have a large impact on their diameters. In particular, it has been found that the lift force tends to enhance the break-up rate of droplets by pushing them towards the wall of the computational domain where both turbulence and shear stress are the strongest. In addition, the turbulent dispersion force has an overall significant impact on the flow motion and makes the droplets move from high concentration to low concentration regions. This phenomenom, only obtained when the turbulent dispersion force is added to the model, engenders a different flow behavior. This study also showed that, for the chosen model, the number of droplets generated during a break-up event has a negligeable impact on its rate. However, the specification of both critical Weber number and coalescence drainage time models play an important role for minimum and maximum droplet diameter predictions. As a result, it is adviced, prior to any PBM simulation, to perform a preliminary study to compute the expected critical werber number and the corresponding coalescence drainage time model. This would ensure that a correct set of numerical parameters is chosen based on the problem specification. Thanks to these findings numerical results have been improved by up to 30% when compared to experimental data and previous simulations with similar models. It is however shown that the minimum size of droplets computed with the current model is relatively far from the one observed in exper-

iments (maximum discrepancies close to 20%). In an attempt to tackle this issue, a new PBM solver has been implemented in OpenFOAM. The break-up model has been entirely reworked and simplifications have been applied to render the model easier to use. Promising results showed that both coalescence and break-up fields are comparable. However, this new model is undergoing active development and improvement. Therefore, further validations are still needed before a clear conclusion can be presented. The limitation of the current model comes with the necessity to manually compute, in advance, the correct set of parameters to be used within the simulation (volume fraction, temperature, velocity or pressure) as boundary conditions. This can become difficult depending on the complexity of the problem specifications.

Due to its relative ease of implementation and its validation performed over the past few years, an enthalpy-porosity based approach has been used in this PhD. Two new single-fluid solidification models have been implemented using this method. These solvers use, respectively, a mushy and a slurry-mushy models. Numerical results obtained in a square cavity have been initialized with the steady state solution of a convection model also implemented in the Open source software. It is shown that both these solvers provide accurate results of water solidification inside both cavities and cylindrical enclosures when compared to experimental data. The maximum local discrepancies are evaluated below 17% for the worst possible scenario. This work has revealed that a variable density of the water phase is mandatory to efficiently model the behaviour observed in experiments. If not use, the convection process is linear and does not represent real physical behavior. It has also been highlighted that the use of an error function to compute the phase change process between liquid and ice is more accurate and faster than a standard linear function. Finally, it has been found that for the slurry-mushy based model, the additional viscosity terms generated an under-prediction of the overall temperature which therefore produced larger errors on time for region transitions between liquid and solid states of water. Even if these solvers permit to obtain result of sufficient quality, 3D simulations on very long domain, requiring a large number of computational cells, could be difficult to perform under reasonable time. This type of numerical simulations requires high computing resources and is time consuming.

These solification solvers have been enhanced further. A multi-fluid version has been implemented and the results obtained showed very good agreement for the ice formation rate (maximum discrepancies below 10%) when compared to experiments. Among interesting findings, it has been shown that the use of variable water properties as a function of the temperature instead of constant ones has very little effect on the quality of the results. This solver ensured that the main objective of this PhD is fulfilled. Even if this work provides a good first step towards a coupling between population balance and solidification models, some clear limitations were discovered. First of all, the present multi-fluid solvers could be used conjointly but not in a "fully-coupled" manner. The work flow is decomposed into two parts. The initial PBM solver is run in advance and the useful quantities (volume fraction, temperature, velocity, droplets diameter and pressure fields) are extracted from the

pseudo-steady state solution. They are then injected as a boundary condition for the multi-fluid solidification solver where the diameter of droplets plays a role into the solidification rate. The current models have limitations, they are not currently able to compute the effect of a change in droplet diameter when the solidification process has begun. As this field of research is extremely new, deposition and mass transfer events have been intentionally neglected.

As a final conclusion, the solvers implemented in this PhD can be used for both research and industrial purposes. Used together, they provide a new approach to simulate more accurately complex flows observed inside pipelines under extreme conditions. The current method however requires additional development. When used separately, they provide accurate results for PBM and solidification studies of multiphase flows.

Chapter 20

Future work

The work performed in this PhD has permitted to identify several gaps in research that may have been depreciated in the past and possible ways to improve the currently available models.

It has been shown that the break-up model used in this PhD probably required additional development. This comment has been adressed and a new formulation has been presented. This, however, requires additional validations. In addition to the method of moment approach developed here, a method of classes model and a quadrature method of moment solver are also being developed and implemented in OpenFOAM. Numerical results from these approaches will be compared against the same numerical results as those discussed in this thesis.

It has also been identified that a thorough analysis of different slurry models and their impacts on solidification rate could be performed to help researchers to choose between different models, depending on the field of applications they are interested in. Similarly to the approach applied in this work concerning variable properties of water, the use of temperature-dependent ice properties could lead to even more realistic results. Finally, the single-fluid solidification solvers have been extended further to handle binary mixture solidification. This work has been investigated in a manuscript pending acceptance.

A full coupling of the population balance and solidification models could be developed and enhanced further, based on the results presented in this PhD. It however requires a full-scale validation of the current multi-fluid models. Hydrates and corrosion studies could, ultimately, emerge from the findings of this PhD.

All these fields of study are currently of great importance and will gain in popularity as pipelines facing extreme conditions become more and more common. In addition, parts of this work could be applied to a wide range of research domains such as the food industry or aerospace since similar phenomena are present.

References

Al-Taweel, A., Madhavan, S., Podila, K., Koksal, M., & Troshko, A. (2006). Cfd simulation of multiphase flow : closure recommendations for fluid-fluid systems. *12th European conference on mixing*, *12*.

ANSYS (2011). *FLUENT User's Guide*. Release 14.0.

Argyropoulos, S. (1981). *Dissolution of high melting point additions in liquid steel*. Ph.D. thesis, McGill University.

Auton, T., & Hunt, J. (1988). The force exerted on a body in inviscid unsteady non-uniform rotational flow. *Journal of Fluid Mechanics*, *197*.

Azzopardi, B., Mudde, R., Lo, S., Morvan, S., Yan, Y., & Zhao, D. (2011). *Macroscale modelling, in Hydrodynamics of gas-liquid reactors: Normal operation and upset conditions*. John Wiley and Sons Ltd.

Barnea, E., & Mizrahi, J. (1975). A generalyzed approach to the fluid dynamics of particulate systems part 2: Sedimentation and fluidization of clouds of spherical liquid drops. *Canadian Journal of chemical engineering*, *53*.

Basu, B., & Date, A. (1988). Numerical modelling of melting and solidification problems:a review. *Sadhana*, *13*.

Bell, G., & Wood, S. (1983). On the performance of the enthalpy method in the region of a singularity. *International Journal of Numerical Methods in Engineering*, *19*.

Bourdillon, A., Verdin, P., & Thompson, C. (2015). Numerical simulations of water freezing processes in cavities and cylindrical enclosures. *Applied thermal engineering*, *75*.

Bourdillon, A., Verdin, P., & Thompson, C. (2016). Numerical simulations of drop size evolution in a horizontal pipeline. *International Journal of Multiphase Flow*, *78*.

Boussinesq, M. (1897). *Theorie de l'ecoulement tourbillonant et tumultueux des liquides dans les lits rectilignes a grande section*. Gauthier-Villars et fils.

BP (2009). Bp statistical review of world energy. Tech. rep., BP.

Burns, A., Frank, T., Hamill, I., & Shi, J. (2004). The favre averaged drag model for turbulent dispersion in eulerian multiphase flows. In *5th Int conference on multiphase flows, 2004, Yokohama, Japan.*

Carman, P. (1937). Fluid flow through granular beds. *Institute of Chemical Engineers*, *15*.

Chen, S., & Lee, T. (1998). A study of supercooling phenomenon and freezing probability of water inside horizontal cylinder. *International Journal of Heat and Mass Transfer*, *41*.

Chhabra, R. (1992). Bubbles, drops and particles in non-newtonian fluids. *CRC Press*, *2*.

Chong, J., Christiansen, E., & Baer, A. (1971). Rheology of concentrated suspensions. *Journal of applied polymer science*, *15*.

Conde, R., Parra, M., Castro, F., Villafruela, J., Rodriguez, M., & Mendez, C. (1976). Transient freezing of liquidus in tube flow. *Nuclear science and engineering*, *60*.

Conde, R., Parra, M., Castro, F., Villafruela, J., Rodriguez, M., & Mendez, C. (2004). Numerical model for two-phase solidification problem in a pipe. *Applied thermal engineering*, *24*.

Coulaloglou, C., & Tavlarides, L. (1977). Description of interaction processes in agitated liquid-liquid dispersions. *Chemical engineering science*, *32*.

Crowe, C., Sommerfield, M., & Tsuji, Y. (1998). *Multiphase flows with droplets and particles.* Boca Raton.

Dabak, T., & Yucel, O. (1986). Shear viscosity behaviour of highly concentrated suspensions at low and high shear rates. *Rheologica acta*, *25*.

Darcy, H. (1856). Les fontaines publiques de la ville de dijon.

Drew, H., & Lahey, R. (1987). The virtual mass and lift force on a sphere in rotating and straining inviscid flow. *International Journal of multiphase flow*, *13*.

Dusinberre, G. (1945). Numerical methods for transient heat flow. *Trans ASME*, *67*.

Ervin, E., & Tryggvason, G. (1997). The rise of bubbles in a vertical shear flow. *Journal of Fluid engineering*, *119*.

Fortune (2009). Global500. Tech. rep., Fortune.

Friesen, W., & Dabros, T. (2003). Constant-number monte carlo simulation of aggregating and fragmenting particles. *Journal of chemical physics*, *119*.

Gartling, D. (1980). Finite element analysis of convective heat transfer problems with phase change of phase. *Computer methods in fluids.*

Giangi, M., Kowaleski, T., Stella, F., & Leonardi, E. (2000). Natural convection during ice formation:numerical simulation vs. experimental results. *Computer assisted mechanics and engineering sciences*, *7*.

Gong, Z., & Mujumdar, A. (1997). Finite element analysis of cyclic heat transfer in a shell-and-tube latent heat energy storage exchanger. *Applied Thermal Engineering*, *17*.

Goodman, T. (1958). The heat-balance integral and its application to problems involving a change of phase. *Trans AMSE*, *80*.

Gupta, P., & Pagalthivarthi, K. (2006). A comparative study of the effect of model lift coefficients on particle trajectory. *Indian journal of engineering and materials sciences*, *13*.

Hamaker, H. (1937). The london-van der waals attraction between spherical particles. *Physica*, *4*.

Harlow, H., & Cook, L. (1984). Virtual mass in multihase flow. *International Journal of multiphase flow*, *10*.

Hashemi, H., & Sliepcevich, C. (1967). A numerical method for solving two-dimensional problems of heat conduction with change of phase. *Chemical Engineering Progress Symposium*, *63*.

Heitz, W., & Westwater, J. (1970). Extension of the numerical method for melting and freezing problems. *International Journal of Heat and mass transfer*, *13*.

Hesketh, R., Etchells, A., & Russell, T. (1991). Bubble breakage in pipeline flows. *Chemical engineering science*, *46*.

Hibiki, T., & Ishii, M. (2007). Lift force in bubbly flow systems. *Chemical engineering science*, *62*.

Hill, D. (1998). *The Computer Simulation of Dispersed Two Phase Flows*. Ph.D. thesis, Imperial College, London.

Hounslow, M., Ryall, R., & Marshall, V. (1988). A discretized population balance for nucleation, growth and aggregation. *Alche journal*, *19*.

Hu, H., & Argyropoulos, A. (1996). Mathematical modelling of solidification and melting: A review. *Modelling Simulation Material Science Engineering*, *4*.

Hulburt, H., & Katz, S. (1964). Some problems in particle technology- statistical mechanical formulation. *Chemical engineering science*, *19*.

Ishii, M., & Zuber, N. (1979). Drag coefficient and relative velocity in bubbly, droplets or particulate flows. *Alche Journal*, *25*.

Ismail, K., Henriquez, J., & DaSilva, T. (2003). A parametric study on ice formation inside a spherical capsule. *International Journal of Thermal Sciences*, *42*.

Issa, R., & Oliveira, P. (1994). Numerical prediction of phase separation in two-phase flow through t-junctions. *Computer fluids*, *23*.

Jalali, A., & Najafi, A. (2010). Numerical modeling of the solidification phase change in a pipe and evaluation of the effect of boundary conditions. *Journal of thermal sciences*, *19*.

Jana, S., Ray, S., & Durst, F. (2007). A numerical method to compute solidification and melting processes. *Applied mathematics modelling*, *31*.

Jorgen, T. (1998). *Simulation and modeling of turbulent incompressible flows*. Ph.D. thesis, Lausanne EPFL.

Klaseboer, E., Chavailler, J., Mate, A., Masbernat, O., & Gourdon, C. (2001). Model on experiments of drop impinging on an immersed wall. *Physics fluids*, *13*.

Kohlrausch, F. (1968). Praktische physik. *Auflage*, *22*.

Kolev, N. (1993). Fragmentation and coalescence dynamics in multiphase flows. *Experimental thermal and fluid science*, *6*.

Kowaleski, T., & Rebow, M. (1999). Freezing of water in a differentially heated cubic cavity. *International Journal of computational fluid dynamics*, *11*.

Krieger, I., & Dougherty, T. (1959). A mechanism for non-newtonian flow in suspensions of rigid spheres. *Journal of Rheology*, *3*.

Kumar, A., & Hartland, S. (1985). Gravity settling in liquid-liquid dispersion. *Canadian Journal of chemical engineering*, *63*.

Lacroix, M. (1993). Numerical simulation of a shell-and-tube latent heat thermal energy storage unit. *Solar energy*, *50*.

Lahey, R., & Lopez, M. (1993). Phase distribution in complex geometry conduits. *Nuclear engineering and design*, *141*.

Lamb, H. (1945). *Hydrodynamics*. Dover Publications.

Lei, H., Geng, D., & He, J. (2009). A continuum model of solidification and inclusion collision-growth in the slab continuous casting caster. *ISIJ international*, *49*.

Liao, Y., & Lucas, D. (2009). A literature review of theoretical models for drop and bubble breakup in turbulent dispersions. *Chemical engineering science*, *64*.

Liao, Y., & Lucas, D. (2010). A literature review on mechanisms and models for the coalescence process of fluid particles. *Chemical engineering science*, *65*.

Litster, J., Smit, D., & Hounslow, M. (1995). Adjustable discretization population balance for growth and aggregation. *Alche journal*, *41*.

Liu, D. (2000). Particle packing and rheological property of highly-concentrated ceramic suspensions : ϕ_m determination and viscosity prediction. *Journal of material science*, *37*.

Lo, S., & Rao, P. (2007). Modelling of droplet break-up and coalescence in an oil-water pipeline. *International conference of multiphase flow*, *13*.

Lo, S., & Zhang, D. (2009). Modelling of break-up and coalescence in bubbly two-phase flows. *Journal of Computational Multiphase flows*, *1*.

Lucas, D., Shi, J., & Krepper, E. (2004). Modelling of non-drag forces for bubbly flows.

Luo, H., & Svendsen, H. (2004). Theoretical model for drop and bubble breakup in turbulent dispersions. *Alche journal*, *42*.

Magnaudet, J., & Legendre, D. (1997). Some aspects of the lift force on a spherical bubble. *Applied Scientific Research*, *58*.

Marchisio, D., & Fox, R. (2013). Computational models for polydispersed particulate and multiphase systems.

Marchisio, D., Fox, R., Pikturna, J., Vigil, R., & Barresi, A. (2003). Quadrature method of moments for population balance equations. *Alche Journal*, *49*.

Marechal, M. (2008). Phase-diagramme.

McGraw, R. (1997). Description of aerosol dynamics by the quadrature method of moments. *Aerosol science and technology*, *27*.

Mei, R., Klausner, J., & Lawrence, C. (1994). A note on the history force on a spherical bubble at finite reynolds number. *Physics of fluids*, *6*.

Metzner, A. (1985). Rheology of suspensions in polymeric liquids. *Journal of rheology*, *29*.

Michalek, T., & Kowaleski, A. (2002). Simulations of the water freezing process - numerical benchmarks. *International Journal of computational fluid dynamics*, *40*.

Mooney, M. (1951). The viscosity of concentrated suspension of spherical particles. *Journal of colloid science*, *6*.

Morsi, S., & Alexander, J. (1972). An investigation of particle trajectories in two-phase flow systems. *Journal of fluid mechanics*, *55*.

Murray, W., & Landis, F. (1959). Numerical and machine solutions of transient heat-conduction problems involving melting or freezing. *Journal of heat transfer*, *81*.

Myers, T., & Mitchell, S. (2011). Application of the combined integral method to stefan problems. *Applied mathematic modelling*, *62*.

Neumann, F. (1912). Die paruellen differentialgleichungen der mathematischen. *Physik*, *2*.

Oliveira, P., & Issa, R. (2001). An improved piso algorithm for the computation of buoyancy-driven flows. *Numerical heat transfer*, *40*.

Paterson, S. (1952). Propagation of a boundary of fusion. *Proc Glasgow Maths assoc*, *1*.

Perrot, P. (1998). *A to Z of thermodynamics*. Oxford university Press, U.S.A.

Petitti, M., Vanni, M., Marchisio, D., Buffo, A., & Podenzani, F. (2012). Application of the conditional quadrature method of moments for the simulation of coalescence, break-up and mass transfer in gas-liquid stirred tanks. *Conference on mixing Warsawa*, *14*.

Poirier, D. (1986). *On numerical methods used in mathematical modeling of phase change in liquid metals*. Master's thesis, University of Ottawa.

Poirier, D., & Salcudean, M. (1988). On numerical methods used in mathematical modeling of phase change in liquid metals. *Journal of heat transfer*, *110*.

Pradipta, K., Dibakar, P., & Ashutosh, P. (2008). Predicting viscosity of limestone-water slurry. *Journal of minerals and materials characterization and Engineering*, *8*.

Prince, M., & Blanch, H. (1990). Bubble coalescence and break-up in air-sparged. *Alche journal*, *36*.

Ramkrishna, D. (1985). The status of population balances. *Journal of chemical engineering*, *49*.

Ramkrishna, D. (2000). Population balances : Theory and applications to particulate systems in engineering. *Academic press*, *8*.

Ranz, W., & Marshall, W. (1958). Evaporation from drops. *Chemical engineering progress*, *48*.

Reizes, J., Leonardi, E., & Vahl Davis, G. (1985). Natural convection near the density extremum of water. *Proceedings of the fourth International conference on numerical methods in laminar and turbulent flow*, *15*.

Richardson, J., & Zaki, W. (1997). Sedimentation and fluidisation: Part 1. *Chemical engineering research and design*, *75*.

Rolph, W., & Bathe, K. (1982). An efficient algorithm for analysis of nonlinear heat transfer with phase changes. *Numerical methods in engineering*, *18*.

Rose, M. (1960). A method for calculating solutions of parabolic equations with a free boundary. *Mathematical Computer*, *14*.

Rosler, F., & Bruggermann, D. (2011). Shell-and-tube type latent heat thermal energy storage : numerical analysis and comparison with experiments. *Journal of heat and mass transfer*, *47*.

Rusche, H., Behzadi, A., & Issa, R. (2004). Modelling of dispersed bubble and droplet flow at high phase fractions. *Chemical Engineering Science*, *59*.

Rusche, H., & Issa, R. (2000). The effect of voidage on the drag force on particles in dispersed two-phase flow. *Japanese European two-phase flow meeting*, *2*.

Saffman, P. (1965). The lift on a small sphere in a slow shear flow. *Journal of fluid mechanics*, *1*.

Salcudean, M., & Abdullah, Z. (1988). On the numerical modelling of heat transfer during solidification process. *Numerical methods in engineering*, *25*.

Schiller, L., & Naumann, A. (1935). A drag coefficient correlation. *Z. Deutsch. Ing.*, *77*.

Shih, T., Liou, W., Shabbir, A., Zhang, Z., & Zhu, J. (1995). A new $k - \varepsilon$ eddy-viscosity model for high turbulent flows: model development and validations. *Computers fluids*, *24*.

Simmons, M., & Azzopardi, B. (2001). Drop size distributions in dispersed liquid-liquid pipe flow. *International Journal of multiphase flow*, *27*.

Snyder, M., Knio, O., Katz, J., & Maitre, O. (2007). Statistical analysis of small bubble dynamics in isotropic turbulence. *Physics fluids*, *19*.

StarCCM+ (2012). *User guide StarCCM+ V.7.06*. CD-Adapco.

Stefan, J. (1889a). Uber die theorie der eisbildung, inbesondere uber die eisbildung im polarmeer. *Annual Chemical and Physics*, *42*.

Stefan, J. (1889b). Wien akad. *Nature*, *98*.

Tacke, K. (1985). Discretization of the explicit enthalpy method for planar phase change. *International Journal of Numerical Methods in Engineering*, *21*.

Takagi, S., Osagawara, T., & Matsumoto, Y. (2008). The effect of surfactant on the multiscale structure of bubbly flows. *Philosophical transactions of the royal society*, *366*.

Tien, L., & Churchill, S. (1965). Freezing front motion and heat transfe routside an infinite isothermal cylinder. *Alche journal*, *11*.

Tomiyama, A., Tamai, H., Zun, I., & Hosokawa, S. (2002). Transverse migration of single bubbles in simple shear flows. *Chemical engineering*, *57*.

Trp, A. (2005). An experimental and numerical investigation of heat transfer during technical grade paraffin melting and solidification in a shell-and-tube latent heat thermal energy storage unit. *Solar energy*, *79*.

Vakhrushev, A., Ludwig, A., Wu, M., Tang, Y., Hackl, G., & Nitzl, G. (2013). Advanced multiphase modelling of solidification with openfoam.

Voller, V., & Prakash, C. (1987). A fixed grid numerical modelling methodology for convection-diffusion mushy region phase-change problems. *Journal of heat and mass transfer*, *30*.

Voller, V., & Swaminathan, C. (1991). General source based method for solidification phase change. *Numerical Heat Transfer*, *19*.

Voller, V., Swaminathan, C., & Thomas, B. (1990). Fixed grid techniques for phase change problems: a review. *Numerical methods in engineering*, *30*.

Wang, D. (1994). Modelling of bubbly flow in a sudden pipe expansion. Tech. rep., BRITE/EuRam project.

Wang, S., Lee, S., Jones, J., & Lacey, J. (1987). 3d turbulence structure and phase distribution measurements in bubbly two-phase flow. *International Journal of multiphase flow*, *13*.

Wei, J., & Pang, M. (2011). Analysis of drag and lift coefficient expressions of bubbly flow system for a low to medium reynolds number. *Nuclear engineering and design*, *241*.

Weigand, B., & Beer, H. (1993). Freezing in turbulent flow inside tubes and channels. *Warme- und stoffubertragung*, *28*.

Wintruff, I., & Gunther, C. (2001). An adaptative moving grid model for convective melting and solidification problems. *Interactive dynamics of convection and solidification*.

Yilmaz, F., & Gundogdu, M. (2009). Analysis of conventional drag and lift models for multiphase cfd modelling of blood flow. *Korea Australia Rheology Journal*, *21*.

Yuan, C., Laurent, F., & Fox, R. (2012). An extended method of moments for population balance equations. *Journal of aerosol science*, *51*.

Zhang, D., & VanderHeyden, W. (2002). The effects of mesoscale structures on the macroscopic momentum equations for two phase flows. *International Journal of multiphase flow*, *28*.

Zhao, H., Kruis, F., & Zheng, C. (2010). A differentially weighted monte carlo method for two-component coagulation. *Journal of computational physics*, *8*.

Zuber, N. (1964). On the dispersed two-phase flow in the laminar flow regime. *Chemical Engineering Science*, *19*.